

Constraining Dark Matter Through the Study of Merging Galaxy Clusters

By

WILLIAM ANTHONY DAWSON

B.S. Maritime Systems Engineering (Texas A& M University, Galveston) 2002

M.S. Physics (University of California, Davis) 2008

DISSERTATION

Submitted in partial satisfaction of the requirements for the degree of

DOCTOR OF PHILOSOPHY

in

Physics

in the

OFFICE OF GRADUATE STUDIES

of the

UNIVERSITY OF CALIFORNIA

DAVIS

Approved:

Professor David M. Wittman, Chair

Professor J. Anthony Tyson

Professor Maruša Bradač

Committee in Charge

2013

Copyright © 2013 by
William Anthony Dawson
All rights reserved.

*To my wife Kerri,
who has sacrificed more for this dissertation than anyone.*

CONTENTS

List of Figures	vii
List of Tables	x
Abstract	xi
Acknowledgments	xiv
1 Introduction	1
1.1 Composition of the Universe	1
1.2 Dark Matter	2
1.2.1 Historical Review	2
1.2.2 General Properties of Dark Matter	3
1.3 Motivation for Studying Self-interacting Dark Matter and Existing Constraints	4
1.3.1 Early Motivation	4
1.3.2 Early SIDM Constraints	5
1.3.3 Recent Motivation	6
1.4 Probes of SIDM	8
1.5 Merging Galaxy Clusters as Probes of Self-Interacting Dark Matter	8
1.5.1 Merging Galaxy Clusters	8
1.5.2 Constraining Self-Interacting Dark Matter with Merging Galaxy Clus- ters	10
2 Musket Ball Cluster: Observed Properties	17
2.1 Introduction	17
2.2 Photometric Studies	18
2.3 Spectroscopic Studies	18
2.4 Weak Lensing Analysis	21
2.5 Sunyaev–Zel’dovich Effect Studies	23
2.6 X-ray Studies	24
2.7 Radio Studies	27

2.8	Cluster Merger Scenario	29
2.9	Discussion	30
3	Dynamics of Merging Clusters	32
3.1	Introduction	33
3.2	Method	37
3.2.1	Model	37
3.2.2	Monte Carlo Analysis	40
3.2.3	Comparison with Hydrodynamic Simulations	42
3.3	Bullet Cluster Dynamics	45
3.3.1	Bullet Cluster Observed System Properties	45
3.3.2	Bullet Cluster System Dynamics Results	45
3.4	Musket Ball Cluster Dynamics	52
3.4.1	Musket Ball Observed System Properties	53
3.4.2	Musket Ball System Dynamics Results	53
3.5	Summary and Discussion	59
3.5.1	Suggested Uses of Method	60
3.5.2	Extensions to the Method	61
4	Musket Ball Cluster: Dark Matter Implications	64
4.1	Introduction	64
4.1.1	Location Estimation	65
4.2	Galaxy Location	65
4.2.1	Definition of Galaxy Location	66
4.2.2	Cluster Membership	68
4.2.3	Galaxy Location Poisson Noise	70
4.2.4	Estimating the Musket Ball Cluster's Galaxy Location	70
4.3	Gas Location	75
4.4	Weak Lensing Location	78
4.4.1	Generic Weak Lensing Errors	78
4.4.2	Dissociative Merger Systematic Errors	79

4.4.3	Weak Lensing Location Results	80
4.5	Gas–Weak Lensing Offset	81
4.6	Galaxy–Weak Lensing Offset	81
4.7	Summary	88
4.8	Discussion	90
5	Perspective: Summary & Discussion	93
5.1	Dissertation Summary	93
5.2	Discussion on the Path Forward	95
5.2.1	Uncertainty in the Location of Galaxies and DM/Lensing	95
5.2.2	Find and study more dissociative mergers	97
5.2.3	Going from Observations to Dark Matter Constraints	99
5.3	Concluding Remarks	101
A	Dynamics of Merging Clusters Appendix	102
A.1	Potential Energy of Two Truncated NFW Halos	102
A.1.1	Truncated NFW Gravitational Potential	102
A.1.2	Mass Elements of a Truncated NFW Halo	103
A.2	Musket Ball Cluster Redshift Catalog	104
A.3	Bullet Cluster Result Plots	106
A.4	Musket Ball Cluster Result Plots	114
B	Fully Probabilistic Galaxy Cluster Membership Determination	121
B.1	Method	121

LIST OF FIGURES

1.1 A basic time series leading to a dissociative galaxy cluster merger.	11
1.2 The four means of constraining σ_{SIDM} with merging clusters.	12
2.1 Merging cluster DLSCL J0916.2+2951 and its three matter components. . .	19
2.2 Color image of DLSCL J0916.2+2951 and its galaxy number density with a histogram of the spectroscopic redshifts in the area.	20
2.3 Musket Ball Cluster color-magnitude diagram based on HST photometry, along with galaxy location based on DLS photometric redshifts.	23
2.4 Comparison of the Musket Ball Cluster, HUDF and GOODS North & South source galaxy densities.	24
2.5 Comparison of the Subaru i' -band ground-based and HST space-based WL mass signal-to-noise maps of DLSCL J0916.2+2951 with the X-ray distribution and galaxy number density.	25
2.6 DLS optical image with SZE and galaxy number density maps.	26
2.7 X-ray map of the Musket Ball Cluster	28
2.8 Radio survey of the Musket Ball Cluster and surrounding area.	30
3.1 Parameters involved in a generic two-halo merger configuration.	35
3.2 Comparison of the analytic model results with hydrodynamic simulation results of the Bullet Cluster.	44
3.3 The posterior of the Bullet Cluster's time-since-collision and three-dimensional collision velocity parameters.	48
3.4 The posterior of the Bullet Cluster's TSC_0 and $v_{3D}(t_{\text{col}})$ parameters after application of an additional temporal prior based on X-ray observations of the Bullet Cluster.	51
3.5 Weak lensing mass PDF's of the Musket Ball subclusters [41].	54
3.6 Relative radial subcluster velocity PDF's inferred from spectroscopic redshifts the Musket Ball Cluster galaxies [41].	54

3.7	Projected separation PDF of the Musket Ball subcluster galaxy density centroids [41].	55
3.8	The posterior of the Musket Ball Cluster's TSC_0 and $v_{3D}(t_{\text{col}})$ parameters.	56
3.9	Comparison of the Musket Ball Cluster's and Bullet Cluster's time-since-collision.	57
4.1	Musket Ball Cluster spectroscopic and photometric magnitude distribution.	72
4.2	Spectroscopic versus photometric redshift for the Musket Ball Cluster.	73
4.3	Empirically based cluster membership weighting scheme; cumulative normalized weight distribution for galaxies being in the Musket Ball Cluster.	74
4.4	Musket Ball Cluster galaxy number density map including spectroscopic redshift information.	76
4.5	Musket Ball Cluster X-ray map with estimated centroid.	77
4.6	Musket Ball Cluster weak lensing signal-to-noise map with X-ray map overlay, including centroid locations.	82
4.7	Musket Ball Cluster weak lensing signal-to-noise map with galaxy number density map overlay, including centroid locations.	83
4.8	Musket Ball southern subcluster galaxy and weak lensing centroid spatial distribution.	84
4.9	Musket Ball southern subcluster galaxy and weak lensing centroid offset significance.	86
4.10	Musket Ball northern subcluster galaxy and weak lensing centroid spatial distribution.	87
4.11	Musket Ball joint northern and southern subcluster galaxy and weak lensing centroid offset significance.	89
5.1	Number of confirmed dissociative mergers as a function of time.	98
A.1	Dynamics results array configuration.	107
A.2	Bullet Cluster marginalized <i>Input vs. Input</i> parameters result plots.	108
A.3	Bullet Cluster marginalized <i>Input vs. Geometry</i> parameters result plots.	109

A.4	Bullet Cluster marginalized <i>Input vs. Velocity & Time</i> parameters result plots.	110
A.5	Bullet Cluster marginalized <i>Geometry vs. Geometry</i> parameters result plots.	111
A.6	Bullet Cluster marginalized <i>Geometry vs. Velocity & Time</i> parameters result plots.	112
A.7	Bullet Cluster marginalized <i>Velocity & Time vs. Velocity & Time</i> parameters result plots.	113
A.8	Musket Ball Cluster marginalized <i>Input vs. Input</i> parameters result plots. . .	115
A.9	Musket Ball Cluster marginalized <i>Input vs. Geometry</i> parameters result plots.	116
A.10	Musket Ball Cluster marginalized <i>Input vs. Velocity & Time</i> parameters result plots.	117
A.11	Musket Ball Cluster marginalized <i>Geometry vs. Geometry</i> parameters result plots.	118
A.12	Musket Ball Cluster marginalized <i>Geometry vs. Velocity & Time</i> parameters result plots.	119
A.13	Musket Ball Cluster marginalized <i>Velocity & Time vs. Velocity & Time</i> parameters result plots.	120
B.1	Probabilistic scheme; cumulative normalized weight distribution for galaxies being in the Musket Ball Cluster.	123
B.2	Comparison of parent galaxy redshift distribution with weighted random draw distribution.	124

LIST OF TABLES

2.1	Observed subcluster and X-ray concentration properties	21
3.1	Bullet Cluster parameter input	46
3.2	Bullet Cluster parameter estimates	50
3.3	Musket Ball Cluster parameter estimates	58
A.1	Musket Ball Cluster Redshift Catalog	105

ABSTRACT OF THE DISSERTATION

Constraining Dark Matter Through the Study of Merging Galaxy Clusters

Context: The majority ($\sim 85\%$) of the matter in the universe is composed of dark matter, a mysterious particle that does not interact via the electromagnetic force yet does interact with all other matter via the gravitational force. Many direct detection experiments have been devoted to finding interactions of dark matter with baryonic matter via the weak force. To date only tentative and controversial evidence for such interactions has been found. While such direct detection experiments have ruled out the possibility that dark matter interacts with baryonic matter via a strong scale force, it is still possible that dark matter interacts with itself via a strong scale force and has a self-scattering cross-section of $\sim 0.5 \text{ cm}^2 \text{ g}^{-1}$. In fact such a strong scale scattering force could resolve several outstanding astronomical mysteries: a discrepancy between the cuspy density profiles seen in ΛCDM simulations and the cored density profiles observed in low surface brightness galaxies, dwarf spheroidal galaxies, and galaxy clusters, as well as the discrepancy between the significant number of massive Milky Way dwarf spheroidal halos predicted by ΛCDM and the dearth of observed Milky Way dwarf spheroidal halos.

Need: While such observations are in conflict with ΛCDM and suggest that dark matter may self-scatter, each suffers from a *baryonic degeneracy*, where the observations might be explained by various baryonic processes (e.g., AGN or supernova feedback, stellar winds, etc.)¹ rather than self-interacting dark matter (SIDM). In fact, the important scales of these observations often coincide with baryonic scales (e.g., the core size in clusters is few factors smaller than the radius of the brightest cluster galaxy). What is needed is a probe of SIDM where the expected effect cannot be replicated by the same processes responsible for the baryonic degeneracy in the aforementioned probes. Merging galaxy clusters are such a probe. During the merging process the effectively collisionless galaxies ($\sim 2\%$ of the cluster mass) become dissociated from the collisional intracluster gas ($\sim 15\%$ of the cluster mass). A significant fraction of the gas self-interacts during the merger and slows down at the point

¹At the heart of this is a current lack of knowledge of the influence of baryons on structure formation.

of collision. If dark matter lags behind the effectively collisionless galaxies then this is clear evidence that dark matter self-interacts. The expected galaxy-dark matter offset is typically >25 kpc (for cross-sections that would explain the other aforementioned issues with Λ CDM), this is larger than the scales of that are plagued by the baryonic degeneracies.

Task: To test whether dark matter self-interacts we have carried out a comprehensive survey of the dissociative merging galaxy cluster DLSCL J0916.2+2951 (also known as the Musket Ball Cluster). This survey includes photometric and spectroscopic observations to quantify the position and velocity of the cluster galaxies, weak gravitational lensing observations to map and weigh the mass (i.e., dark matter which comprises $\sim 85\%$ of the mass) of the cluster, Sunyaev-Zel'dovich effect and X-ray observations to map and quantify the intracluster gas, and finally radio observations to search for associated radio relics, which had they been observed would have helped constrain the properties of the merger. Using this information in conjunction with a Monte Carlo analysis model I quantify the dynamic properties of the merger, necessary to properly interpret constraints on the SIDM cross-section. I compare the locations of the galaxies, dark matter and gas to constrain the SIDM cross-section. This dissertation presents this work.

Findings: We find that the Musket Ball is a merger with total mass of $4.8_{-1.5}^{+3.2} \times 10^{14} M_\odot$. However, the dynamic analysis shows that the Musket Ball is being observed $1.1_{-0.4}^{+1.3}$ Gyr after first pass through and is much further progressed in its merger process than previously identified dissociative mergers (for example it is $3.4_{-1.4}^{+3.8}$ times further progressed than the Bullet Cluster). By observing that the dark matter is significantly offset from the gas we are able to place an upper limit on the dark matter cross-section of $\sigma_{\text{SIDM}} m_{\text{DM}}^{-1} < 8 \text{ cm}^2 \text{ g}^{-1}$. However, we find an that the galaxies appear to be leading the weak lensing (WL) mass distribution by $20.5''$ (129 kpc at $z=0.53$) in southern subcluster, which might be expected to occur if dark matter self-interacts. Contrary to this finding though the WL mass centroid appears to be leading the galaxy centroid by $7.4''$ (47 kpc at $z=0.53$) in the northern subcluster.

Conclusion: The southern offset alone suggests that dark matter self-interacts with $\sim 83\%$ confidence. However, when we account for the observation that the galaxy centroid appears to trail the WL centroid in the north the confidence falls to $\sim 55\%$. While the SIDM scenario

is slightly preferred over the CDM scenario it is not significantly so.

Perspectives: The galaxy-dark matter offset measurement is dominated by random errors in each cluster. Thus measuring this offset in other dissociative mergers holds the promise of reducing our uncertainty and enabling us to: 1) state confidently whether dark matter self-interacts via a new dark sector force, or 2) constrain the dark matter cross-section to such a degree that SIDM cannot explain the aforementioned mysteries². To this end we have established the Merging Cluster Collaboration to observe and simulate an ensemble of dissociative merging clusters. We are currently in the process of analyzing six dissociative mergers with existing data, and carrying out multi-wavelength observations of a new sample of 15 radio relic identified dissociative mergers.

²In the case of a null detection of an offset between the galaxies and the DM, SIDM simulations will be necessary to place a quantitative constraint on the SIDM cross-section [see e.g., 127].

ACKNOWLEDGMENTS

I have had the good fortune of being positively influenced by many people during my life, thank you all. There are several people that deserve special note. First and foremost I am indebted to my wife Kerri. She has sacrificed more in the pursuit of this doctorate than any wife should be asked to sacrifice. I surely would not have succeeded without her support during every facet of this endeavor. I also thank my two boys, Evry and Lander, who have strengthened my resolve in studying a subject that is not likely to bear tangible fruit during my lifetime, but may bear fruit in their lifetime or their children's lifetime. I particularly want to thank my mother Marie for instilling in me a healthy sense of overconfidence and curiosity. Without which I would have never had the courage or desire to pursue a degree in physics. I thank my father Bill whose exemplary dedication and leadership in his pursuit to serve humanity provided a high mark that I will always strive towards. I also thank my other father Jim for providing unending support and introducing me to the many wonders of our natural world. I would like to thank my brother Thomas for sharing a curiosity of how things work and, through his own example, making exceptional career endeavors seem a little less exceptional. I also owe a great deal of thanks to my grandmother Imogene whose boundless love of the world and people around her gave me a hint to beauty of the universe and has inspired me to share that beauty with others.

I cannot take full credit for the work presented in this dissertation, it is the result of a concerted effort on the part of many researchers. In particular, I would like to acknowledge and thank my advisor Dr. David Wittman. He has always encouraged my research-freewill, while at the same time providing invaluable input and correcting guidance. It was Dave that first encouraged me to pursue my interest of merging galaxy clusters, despite there being more tangible research topics that we could have worked on. Furthermore for encouraging me to write a Chandra proposal as a second year graduate student, a proposal that was later accepted and provided the impetus for this whole dissertation. From these modest beginnings to the current state of a multi-national/institutional merging cluster collaboration Dave has been more than an advisor, he has been a partner.

I also owe a great deal of thanks to my other two dissertation committee members, Dr.

Tony Tyson and Dr. Maruša Bradač. They both provided valuable feedback and guidance during the writing of this dissertation, but far beyond that they have been major influences shaping the scientist that I have become. I can honestly say that I would not be the scientist I am today without Tony. He taught me single lesson that has influenced me the most: work in the low signal-to-noise regime because that is where the truly surprising science lies, but be ever vigilant of spurious results and pathological science. I am honored to be part of his great legacy. Maruša also deserves a great deal of credit for the scientist I am today. I have come to rely on her unbiased and unabashed feedback in almost every major decision I make. While I don't always agree with her, I often regard her opinion above all others.

My many collaborators (including Dave, Tony and Maruša) deserve much of the credit for this dissertation. I would particularly like to thank James Jee who performed almost all of the underlying lensing related data reduction, which played a critical role in this dissertation. I also thank Perry Gee who first discovered the Musket Ball Cluster and laid the spectroscopic ground work that was crucial in providing the first evidence of it being a dissociative merger. On a related note I thank Dan Marrone for providing the SZE measurements of the Musket Ball Cluster that was also part of the first evidence suggesting that the Musket Ball Cluster was a dissociative merger (in addition to coming up with the "Musket Ball" name). And I thank Jack Hughes for not only reducing the Chandra X-ray data, which proved that the Musket Ball Cluster was a dissociative merger, but for taking the time to teach me how to reduce the data myself. Crucial to the work of this dissertation was the previous work by all of the Deep Lens Survey collaboration, without which the Musket Ball Cluster may have never been discovered. Special thanks are due to the many people who worked on the photometry and photometric redshifts, in particular Sam Schmidt.

I would like to thank all of the members of the Merging Cluster Collaboration: Maruša Bradač, Marcus Bruggen, James Bullock, Oliver Elbert, James Jee, Manoj Kaplinghat, Alison Mansheim, Julian Merten, Karen Ng, Annika Peter, Miguel Rocha, Reinout van Weeren and David Wittman. Together we have taken raw ideas and turned them into a coherent directive. Many of the concepts presented in this dissertation are the result of our many discussions. In this regard a considerable amount of thanks are due to UC-HiPACC which has generously funded our collaboration through travel support.

I would also like to thank the UC Davis cosmology group, which has provided a fertile and supportive environment. In addition to the aforementioned faculty and researchers, I would like to thank Professor Chris Fassnacht who has always taken the lead to promote a social and healthy group, and Bob Becker for never having security remove me from the premises after the multiple times he has fired me. I would also like to thank my former officemates, Brian Lemaux, Dave Lagattuta, Greg Zeimann, Nicholas Hall, Marius Millea, Nick Rumbaugh, and Jackie Hodge. Not only did you provide the most enjoyable and entertaining work environment I have ever been a part of, but I learned a great deal from each of you (well everyone except Marius and Nick). In particular I have Brian to thank for everything I know about spectroscopy. He has always been an incredibly patient and thorough instructor. I would also like to thank Brian, Dave, and Chris Morrison for their invaluable help with formatting this dissertation, and in doing so saved me countless hours.

Finally I would like to thank the citizens of the United States of America. Without their financial support of scientific research none of this would be possible. Specifically, my research has been funded directly by the University of California at Davis through multiple block grants and through the support of my advisor. Support for this work was also provided by NASA through Chandra Award Number GO1-12171X issued by CXO Center, which is operated by the SAO for and on behalf of NASA under contract NAS8-03060, and support for program number GO-12377 was provided by NASA through a grant from STScI, which is operated by the Association of Universities for Research in Astronomy, Inc., under NASA contract NAS5-26555. Additional research funding was provided through the NSF under grant AST-1108893 and considerable travel funding has been provided by UC-HiPACC.

Chapter 1

An Introduction to Self-interacting Dark Matter and Merging Galaxy Clusters

1.1 Composition of the Universe

Over the past one-hundred years there has been a revolution in our understanding of the universe. From believing that the Milky Way was the extent of the Universe, that the age of Universe was infinite, and that the Universe was composed entirely of atomic matter and photons, to now having evidence that the Universe extends further than light can travel in the finite age of the universe [13.817 ± 0.048 Gyr; 122], and is dominated by mysterious dark energy and dark matter rather than atomic matter. Our studies of the universe have improved to such a degree that we are now able to quantify the composition of the universe to percent level accuracy. It has been found that atomic matter (which is dominated by baryonic particles, i.e. particles of the atomic nuclei) only accounts for $\sim 5\%$ of the universe's total matter-energy budget. The universe appears to largely be composed of dark matter (DM; $\sim 26\%$) and dark energy [$\sim 69\%$; see 122, for more accurate values]. Very little is known about each of these components. In very basic terms, dark energy appears to be a non-relativistic particle or field that acts to make the universe expand, while DM appears to be a particle that currently has only been observed to interact via the gravitational force (also known as cold dark matter; CDM). This has come to be known as the concordance cosmological model (Λ CDM). This dissertation will focus on our efforts to further our understanding of

DM, in particular to ascertain whether DM interacts with itself other than through the gravitational force.

1.2 Dark Matter

1.2.1 Historical Review

“Dunkle (kalte) Materie” (or “Dark (cold) Matter”) was first proposed by Zwicky [172]. Zwicky had measured the velocities of the galaxies in the Coma galaxy cluster (via their spectroscopic redshifts) and found that given their large velocity dispersion, the galaxies should not be gravitationally bound if galaxies and stars make up the entirety of the cluster mass. According to his calculations the total CDM mass was thought to be about 400 times that of the mass of the visible galaxies. As van den Bergh [151] notes in his review article, had Zwicky used the correct value for the Hubble constant (rather than the generally accepted value of his day, $H_0=558 \text{ km s}^{-1} \text{ Mpc}^{-1}$) he would have found that the CDM mass must be about 50 times that of the mass of the luminous matter, very close to the actual value of ~ 20 (disregarding the mass of the X-ray emitting intracluster gas that was unbeknownst to astronomers at the time). In 1939 Horace Babcock performed a similar study on the rotation velocities of stars in the Andromeda galaxy and also found that rotation velocities were incompatible with the amount of mass inferred from the stellar luminosity. Despite Zwicky’s pioneering and shocking findings and Babcock’s supporting evidence, the idea of DM did not garner much attention until the work of Vera Rubin [e.g., 131] on the rotation velocities of stars and gas in large sample of spiral galaxies.

Zwicky also introduced another, completely independent, method of measuring the mass of galaxy clusters: “gravitational lens effect” [173]. Zwicky argued that if his mass estimates of the Coma cluster were correct, then the cluster should be massive enough to distort space-time to such a degree that as light from distant background galaxies travels through the gravitational potential well of the cluster the light will be deflected and the galaxy images will be distorted in a coherent fashion. Thus by measuring the distortion of galaxies behind a galaxy cluster one could estimate the mass of the galaxy cluster [see Chapter 2 of 35, for an introduction to weak gravitational lensing]. While Lynds & Petrosian [88] were the first to observe a strong gravitational lens effect it wasn’t until the advent of CCD detectors [e.g.,

56] that Tyson et al. [150] were able to first successfully measure the weak gravitational lens effect of a galaxy cluster and estimate its mass. They too found that a mass of the luminous matter alone was insufficient to produce the observed effect.

While the aforementioned work, and subsequent work, found that the amount of luminous mass in galaxies and clusters was not enough to gravitationally bind the stars and galaxies in those structures, there was still a debate about the solution to this problem. Three general candidates for DM originally dominated the debate: it was simply massive compact objects made up of standard model particles, or it was some new particle, or general relativity needed to be modified [see 134, for a review]. The MACHO experiment [2] eventually ruled out the possibility that massive compact objects made up the bulk of DM, and observations of the merging galaxy cluster 1E 0657-558 (the Bullet Cluster) eventually ruled out modified gravity [29] thus providing strong evidence for DM being a new particle. The Bullet Cluster was the first discovered *dissociative merger* (see Figure 1.1 for a diagram of a dissociative merger). During the merging process the effectively collisionless galaxies become dissociated from the collisional intracluster gas, of which a large fraction self-interacts during the merger and becomes pancaked at the point of collision. In total the cluster gas is about seven times as massive as the galaxies. When Clowe et al. [30] measured the location of the total cluster mass using the gravitational lens effect they found that the majority of the mass was located with the galaxies rather than with the gas. Following more precise measurements via strong gravitational lensing Bradač et al. [20] then inferred that this was only possible if there was a DM particle that was nearly collisionless like the galaxies; modified gravity could not easily explain such an observation and simultaneously explain CDM dynamics on both galaxy and cluster scales with only one MOND parameter.

1.2.2 General Properties of Dark Matter

Peter [120] provides a review of our current understanding of DM; I summarize a few relevant points here. In addition to the abundance of DM (see §1.1) there are a few things we know about the properties of DM. Most notably DM is electromagnetically neutral. DM does not interact with photons, either through absorption or emission. Baryons cannot make up a large portion of DM. This is known from observations of the cosmic microwave background,

large-scale structure of the universe, and abundance of light elements created during big-bang nucleosynthesis. Nor can DM consist solely of light (sub-keV-mass) relativistic particles [e.g. neutrinos 146]. Light particles move too fast in the early universe to form the initial density concentrations necessary to seed the cosmic structures observed at later times. DM is completely outside the realm of our Standard Model of Particle Physics. Thus there is no reason to expect that it only interacts via the known forces. It is entirely possible that DM interacts with itself via some new dark gauge bosons in addition to a possible weak interaction with baryons. Such DM has been termed self-interacting dark matter (SIDM).

1.3 Motivation for Studying Self-interacting Dark Matter and Existing Constraints

1.3.1 Early Motivation

The earliest motivation for studying SIDM came from the *missing satellites problem* [see 21, for a thorough review]. Moore et al. [105] and Klypin et al. [82] were the first to note that the number of Milky Way satellites predicted by Λ CDM simulations significantly exceeded the number of observed satellites. In an attempt to resolve this problem Spergel & Steinhardt [142] revived a SIDM model with a large scattering cross-section but with negligible annihilation or dissipation¹. They found that if the SIDM scattering cross-section ($\sigma_{\text{SIDM}}/m_{\text{DM}}$) is between $0.45\text{--}450 \text{ cm}^2 \text{ g}^{-1}$ then the expected number of Milky Way satellites could be brought in line with the number of observed satellites. More recently the Sloan Digital Sky Survey (SDSS) and Sloan Extension for Galactic Understanding and Exploration (SEGUE) have enabled the discovery of a number of new dwarf satellites [see 165, for a review], effectively doubling the number of known satellites. This in combination with simulations that better quantified the selection function of these surveys has helped to reduce the tension between Λ CDM and the total number of observed satellites. While the missing satellites problem is not resolved, the gap is not nearly as large as originally believed. Recently though a number of other problems have cropped up, e.g., the “too big to fail”

¹Such a SIDM model was first proposed by Carlson et al. [24] and Machacek [90] to suppress small scale power of CDM dominated cosmologies. de Laix et al. [42] found that while SIDM suppressed the small scale power spectrum in a desirable way it resulted in inconsistencies with the observed properties of galaxies. The de Laix et al. [42] objections are no longer valid as they only applied to CDM dominated cosmologies, not Λ CDM cosmologies.

problem [18] and the “cusp/core” problem [e.g., 85], see the discussion in §1.3.3. On a final note, recent simulations [130] show that for $\sigma_{\text{SIDM}}/m_{\text{DM}} \sim 1 \text{ cm}^2 \text{ g}^{-1}$ the effects of DM halo evaporation are less than originally estimated by Spergel & Steinhardt [142]’s analytic estimates, especially in the outer radii of parent DM halos where the majority of satellites reside. This is in stark contrast to the expectations of warm DM (WDM; \sim keV-mass), which was also originally considered as a possible solution of the missing satellites problem. However, WDM cannot resolve the too big to fail or cusp/core problems [e.g. 89, 158].

1.3.2 Early SIDM Constraints

Following the revival of SIDM by Spergel & Steinhardt [142], a number of researchers began to constrain $\sigma_{\text{SIDM}} m_{\text{DM}}^{-1}$ through several independent observations, in what Peter et al. [121] has termed the “Y2K-era constraints”. The Y2K-era constraints fall into five categories:

- (i) Those that compare the central density of simulated SIDM halos with the observed central densities across a range of halo mass-scales from dwarf spheroids to galaxy clusters [33, 37, 38, 73, 83, 98, 169, 170]. Some found that SIDM created central density cores (i.e. flattened density profile) that were too large. While others found that SIDM with large cross-sections actually exacerbated the formation of cusps (i.e. sharply peaked density profile).
- (ii) Those that compare the shape (i.e. spherical or elliptical) of simulated SIDM halos with the shapes of observed DM halos [38, 104, 169]. They found that as the SIDM cross-section increases, DM halos become more spherically symmetric and at a certain point elliptical halos can no longer be formed. This is then in conflict with the observed ellipticity of some galaxy cluster.
- (iii) Those that compared the amount of substructure in simulated SIDM halos with the amount observed in galaxies and galaxy clusters [33, 64, 73, 169]. Finding that as the SIDM cross-section is increased the majority of the subhalos begin to evaporate in their parent DM halo, ultimately resulting in a conflict between the amount of observed substructure and that predicted by the simulations.
- (iv) Those that estimated the formation of super massive black holes (SMBH) as a function of varying SIDM cross-section [70]. As the SIDM cross-section is increased the

initial seeds of SMBH's can form earlier and more efficiently. At some point the expected number and mass of SMBH's exceeds the observed number and mass.

(v) Those that compared and contrasted the observed behavior of DM with collisionless galaxies and collisional gas during the merging process of two galaxy clusters [93]. This method will be the focus of this dissertation and is discussed in great detail in §1.5.2.

Of these early works four constrained the velocity independent $\sigma_{\text{SIDM}} m_{\text{DM}}^{-1}$ to such a degree that it became astrophysically uninteresting. Gnedin & Ostriker [64] obtained a constraint of $\sigma_{\text{SIDM}} m_{\text{DM}}^{-1} \lesssim 0.3 \text{ cm}^2 \text{ g}^{-1}$ with their study of subhalo evaporation in galaxy clusters. Yoshida et al. [170] and Meneghetti et al. [98] obtained a constraint of $\sigma_{\text{SIDM}} m_{\text{DM}}^{-1} \lesssim 0.1 \text{ cm}^2 \text{ g}^{-1}$ with their study of the central densities of galaxy clusters. Finally Miralda-Escudé [104] obtained the tightest constraint, $\sigma_{\text{SIDM}} m_{\text{DM}}^{-1} \lesssim 0.02 \text{ cm}^2 \text{ g}^{-1}$, with their study of galaxy cluster halo shapes. However recent SIDM simulations [121, 130] have cast serious doubts on each of these previous constraints. Rocha et al. [130] find that the previous subhalo evaporation and central density constraints are likely overestimated, and Peter et al. [121] points out several weaknesses of the Miralda-Escudé [104] work plus presents contradictory results. In summary Peter et al. [121] and Rocha et al. [130] find observations of central densities and halo shapes actually only result in a constraint of $\sigma_{\text{SIDM}} m_{\text{DM}}^{-1} \lesssim 1 \text{ cm}^2 \text{ g}^{-1}$. The primary reason being that the Miralda-Escudé [104] results failed to properly account for the fact that the observed surface mass density from lensing gains much of its signal from the projected cluster mass well outside the core (in regions where the cluster ellipticity can be maintained with $\sigma_{\text{SIDM}} m_{\text{DM}}^{-1} \lesssim 1 \text{ cm}^2 \text{ g}^{-1}$). As will be discussed in §1.3.3, $\sigma_{\text{SIDM}} m_{\text{DM}}^{-1}$ between $\sim 0.3 - 1 \text{ cm}^2 \text{ g}^{-1}$ has potentially interesting and desirable astrophysical implications, not to mention important consequences for fundamental physics.

1.3.3 Recent Motivation

After the burst of Y2K-era work, there was little work done in the field of SIDM, with only a few new constraints trickling in [19, 41, 91, 100, 127]. However, the field has recently entered a renaissance with extensive theoretical work [1, 5, 51, 125, 147, 148] and simulation work [121, 130, 159, 160, 171]. This renaissance can largely be attributed to three apparent conflicts between astrophysical observations and Λ CDM:

(i) Studies of the stellar kinematics in low surface brightness (LSBs) and dwarf spheroidal galaxies [dSphs; 85, 115, 140] have shown that the radial velocity profiles of the stars in many halos are better fit by a pseudoisothermal density profile (i.e. cored isothermal profile) rather than an Navarro-Frenk-White [NFW; 108] density profile predicted by Λ CDM. In other words Λ CDM produces DM halos that are too cuspy in the central density profile, while a pseudoisothermal density profile suggests that there is energy exchange occurring in the centers of these galaxies which produced cored (or flattened) central density halo. Using SIDM simulations, Rocha et al. [130] found that if $\sigma_{\text{SIDM}} m_{\text{DM}}^{-1} \sim 0.5 \text{ cm}^2 \text{ g}^{-1}$ then there is enough thermal exchange between the DM to produce cores of the size observed in the LSBs and dSphs.

(ii) All observed dSphs of the Milky Way have $12 \leq V_{\text{circ}}(r_{1/2}) \leq 20 \text{ km s}^{-1}$, where $V_{\text{circ}}(r_{1/2})$ is the circular velocity of particles at the half-light radius and is equal to $\sqrt{GM/r_{1/2}}$, where G is the gravitational constant and M is the mass within $r_{1/2}$. Recent Λ CDM simulations of Milky Way-like halos predict that at least 10 dSphs in the Galaxy's halo should have $V_{\text{circ}}(r_{1/2}) > 20 \text{ km s}^{-1}$ [18]. If the Λ CDM simulations are correct then this would suggest that Milky Way is missing a significant number of large dSphs, or these large dSphs DM halos are devoid of stars which is implausible. SIDM (with cross-sections that have not been ruled out by other means) results in a nearly identical power spectrum at these scales and above [130], thus these large dSphs will still exist in SIDM cosmologies. While this appears to be an entirely separate problem than the dSphs cusp/core problem previously mentioned, it may just be another perspective of exactly the same problem. Perhaps it is not that these massive dSphs are missing, but rather that their central densities are lower than predicted by Λ CDM (i.e. they are cored). If they are cored then some of the halo mass is diffused from the central $r_{1/2}$ outwards. Thus the halo's mass could remain the same but $V_{\text{circ}}(r_{1/2})$ would decrease. Again the work of Rocha et al. [130] suggests that if DM self-interacts with $\sigma_{\text{SIDM}} m_{\text{DM}}^{-1} \sim 0.5 \text{ cm}^2 \text{ g}^{-1}$ then the resulting central densities of the dSphs would be cored to such a degree to ameliorate this apparent discrepancy.

(iii) Finally on the much larger galaxy cluster scales, recent observations of their density profiles [109, 110] suggest that clusters have central cores at odds with Λ CDM. Comparison of the observed core size with simulations [121, 130] shows that $\sigma_{\text{SIDM}} m_{\text{DM}}^{-1} = 1.0 \text{ cm}^2 \text{ g}^{-1}$

will produce cores larger than what is observed. However, SIDM with $\sigma_{\text{SIDM}} m_{\text{DM}}^{-1} \sim 0.1\text{-}0.5 \text{ cm}^2 \text{ g}^{-1}$ is capable of producing the observed cores.

These observations all highlight inconsistencies with ΛCDM and simultaneously suggest SIDM with $\sigma_{\text{SIDM}} m_{\text{DM}}^{-1} \sim 0.1\text{-}0.5 \text{ cm}^2 \text{ g}^{-1}$. If $\sigma_{\text{SIDM}} m_{\text{DM}}^{-1} \lesssim 0.1 \text{ cm}^2 \text{ g}^{-1}$ then SIDM is not capable of resolving any of these observed inconsistencies. Given the existing constraints of $\sigma_{\text{SIDM}} m_{\text{DM}}^{-1} \lesssim 1.0 \text{ cm}^2 \text{ g}^{-1}$ this leaves a narrow window of parameter space to explore.

1.4 Probes of SIDM

While laboratory experiments have placed tight constraints on the baryon-dark matter interaction cross-section (~ 21 orders of magnitude tighter than the current σ_{SIDM} constraints), these experiments are insensitive to DM-DM interactions. The only way to investigate whether DM self-interacts is through astrophysical observations (§1.3.2 summarized the various astrophysical methods for constraining SIDM).

As discussed in the previous section the greatest tensions with ΛCDM come from studies of the central densities of DM halos. This is true over a range of halo scales from LSBs to galaxy clusters. While such probes suggest that DM may self-scatter, each suffers from a *baryonic degeneracy*, where the observations might be explained by various baryonic processes/assumptions (e.g. AGN or supernova feedback, or the assumed initial mass function)². In fact the important scales of these observations often coincide with baryonic scales [e.g. the core size in clusters is few factors smaller than the effective radius of the brightest cluster galaxy; 109, 110]. What is needed is a probe of self-interacting dark matter (SIDM) where the expected effect is independent of these baryonic degeneracies. Merging galaxy clusters are such a probe.

1.5 Merging Galaxy Clusters as Probes of Self-Interacting Dark Matter

1.5.1 Merging Galaxy Clusters

According to the generally accepted model of structure formation, small structures (e.g. galaxies) form first, then through gravitational attraction they begin to merge and form

²At the heart of this is a current lack of knowledge of the influence of baryons on structure formation.

larger structures (e.g. galaxy clusters). This process constantly repeats throughout the history of the universe and is known as the hierarchical structure formation model. When small structures merge with larger structures (e.g. dSphs merging with a galaxy or galaxies merging with a galaxy cluster) the smaller structures are often dramatically altered (often having some of their stars, gas and DM³ stripped from them), yet the larger structures remain mostly unaffected and there is little net change in the system. Occasionally structures of nearly the same size (e.g. two galaxies or two galaxy clusters) will merge. In these cases the system is often dramatically disturbed and will remain in such a disturbed state until dissipative processes (e.g. dynamic friction, and thermal radiation) cause the two structures to combine and the system to enter a relaxed state (of order Gyr). It is the disturbed phase of merging galaxy clusters that provides a means of testing whether DM self-interacts.

Merging galaxy clusters are the most energetic example of hierarchical structure formation. Figure 1.1 shows the schematic time-series of a merging galaxy cluster leading to a *dissociative merger*, a highly disturbed system where the intracluster gas has become dissociated from the galaxies and DM. In the case of a dissociative merger two subclusters⁴ begin with some physical separation, often significantly larger than the size of the individual subclusters. The mass of each subcluster is composed of ~2% galaxies, ~13% intracluster gas, and ~85% DM. Through gravitational attraction the two subclusters accelerate towards one another with the relative velocity of each approaching free-fall velocity⁵. Eventually the two subclusters may collide⁶. Because there is so much space between the galaxies, a significant interaction between any two galaxies is extremely unlikely and they can be treated as effectively collisionless particles. And since the galaxies of each subcluster have built up momentum they will pass through and begin to separate (see t_5 of Figure 1.1). The gas however is more evenly distributed, thus an interaction between the gas particles of each subcluster is more likely. These interactions will convert some of the infall kinetic energy into thermal energy (i.e. the gas of each subcluster will experience ram pressure), the net effect

³Less so if DM is collisionless.

⁴While they are both technically galaxy clusters they are termed subclusters to distinguish them from the galaxy cluster system they will eventually form when the merger is complete.

⁵It is possible that the two will collide with a velocity greater than the free-fall velocity since surrounding large scale structure can influence their motion.

⁶The time of collision is defined to be the time of the first pericentric passage (t_4 of Figure 1.1).

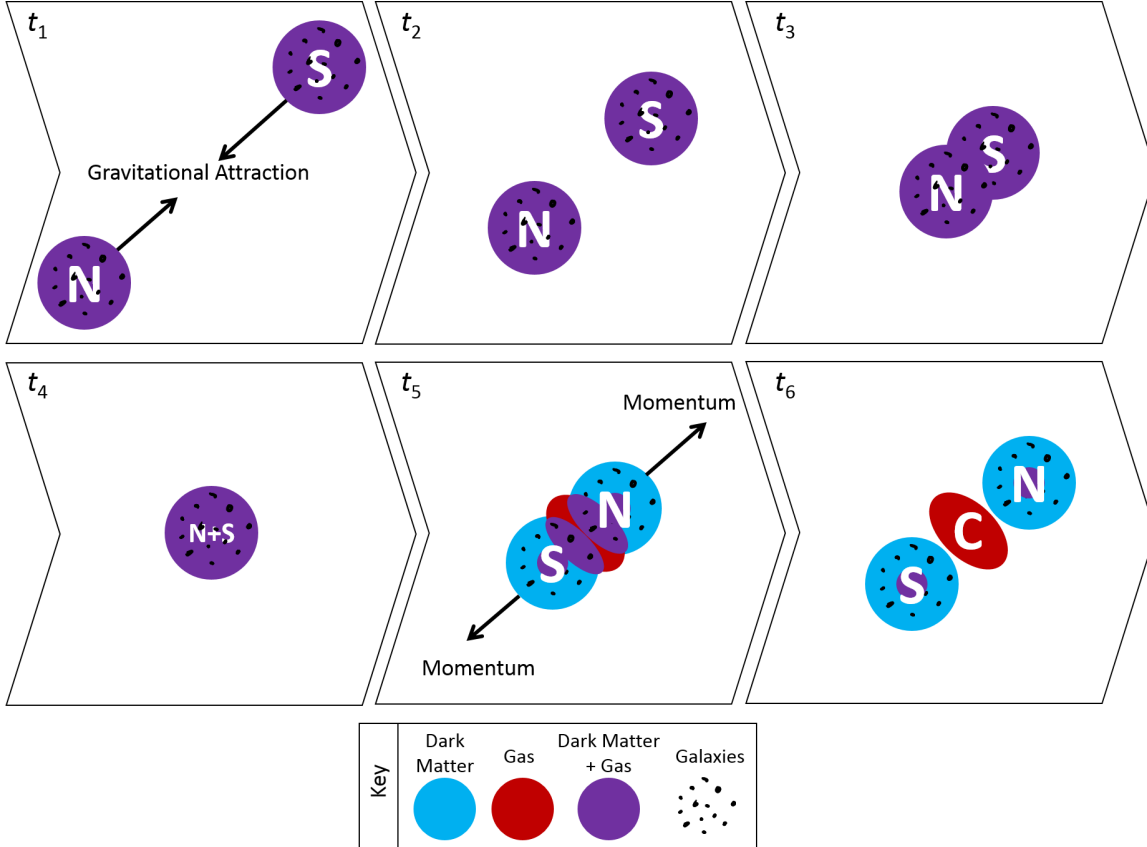


Figure 1.1: A basic time series leading to a dissociative galaxy cluster merger. Two galaxy clusters (N & S), each consisting of overlapping halos of DM and gas as well as sparsely populated galaxies, begin with an initial physical separation (t_1). Due to the mass of each galaxy cluster they experience a gravitational attraction and accelerate towards one another until eventually they collide (t_1-t_4). By convention time t_4 is defined as the “collision”. The momentum of the effectively collisionless galaxies will cause them to pass through the impact, t_5 , only slowed slightly by dynamic friction. The collisional gas will strongly self-interact, slowing significantly, and remain in the center (t_6 C). Much like the galaxies the DM behaves in a nearly collisionless manner and appears largely coincident with the galaxies. At t_6 the galaxy cluster merger is classed as *dissociative merger*. At later times dissipative processes (e.g. dynamic friction, and thermal radiation) will have caused the two structures to combine into a single relaxed galaxy cluster.

being that the gas halo of each subcluster is slowed with respect to the galaxies and much of it becomes dissociated and remains centered between the galaxies of the two subclusters ('C' in t_6 of Figure 1.1). Given that $\sigma_{\text{SIDM}} m_{\text{DM}}^{-1} \lesssim 1.0 \text{ cm}^2 \text{ g}^{-1}$, if the DM interacts it will be significantly less than the gas and behave more like the effectively collisionless galaxies. Thus the DM will predominately be located with the galaxies. It is during this disturbed phase of the merger (t_6 of Figure 1.1) that it is termed dissociative and can provide the best constraints on $\sigma_{\text{SIDM}} m_{\text{DM}}^{-1}$.

1.5.2 Constraining Self-Interacting Dark Matter with Merging Galaxy Clusters

Markevitch et al. [93] originally introduced (and applied to the Bullet Cluster) three methods for constraining σ_{SIDM} with observations of dissociative mergers. This was followed by Randall et al. [127] who introduced (and also applied to the Bullet Cluster) an additional method of constraint by combining observations and simulations of dissociative mergers. These four methods are shown in Figure 1.2 and are discussed below.

1.5.2.1 Dark Matter - Gas Offset

The first method that Markevitch et al. [93] introduced used the fact that in the case of the Bullet Cluster the DM was observed to be significantly offset from the gas. According to the generic merger picture discussed in §1.5.1 this is because the collisional gas has a significantly larger scattering depth⁷ than the DM and thus is likely to self-interact and become dissociated from the DM. Thus Markevitch et al. [93] set up the following inequality:

$$\tau_{\text{gas}} \gtrsim \tau_{\text{SIDM}},$$

relating the scattering depth of the gas, $\tau_{\text{gas}} \approx 1$, to the scattering depth of SIDM, $\tau_{\text{SIDM}} = \sigma_{\text{SIDM}} m_{\text{DM}}^{-1} \Sigma_{\text{DM}}$, where Σ_{DM} is the surface mass density of the DM particles⁸. Thus,

$$1 \gtrsim \frac{\sigma_{\text{SIDM}}}{m_{\text{DM}}} \Sigma_{\text{DM}} \quad (1.1)$$

$$\frac{\sigma_{\text{SIDM}}}{m_{\text{DM}}} \lesssim \Sigma_{\text{DM}}^{-1}.$$

This method has been applied to a number of dissociative mergers [41, 93, 100], with constraints ranging from $\sigma_{\text{SIDM}} m_{\text{DM}}^{-1} < 3-8 \text{ cm}^2 \text{ g}^{-1}$. This method has two notable disadvantages that are apparent from Equation 1.1: the constraint can only be improved by finding clusters with larger Σ_{DM} and the constraint is inversely proportional to the surface mass density. Two of the existing constraints [93, 100] come from extremely dense clusters. To better the

⁷Scattering depth is analogous to optical depth but is related to baryon-baryon or DM-DM scattering rather than Rayleigh scattering.

⁸Markevitch et al. [93] assumed that Σ_{DM} is approximately the weak lensing (WL) measured surface mass density, Σ , since the majority of a typical cluster's mass is DM.

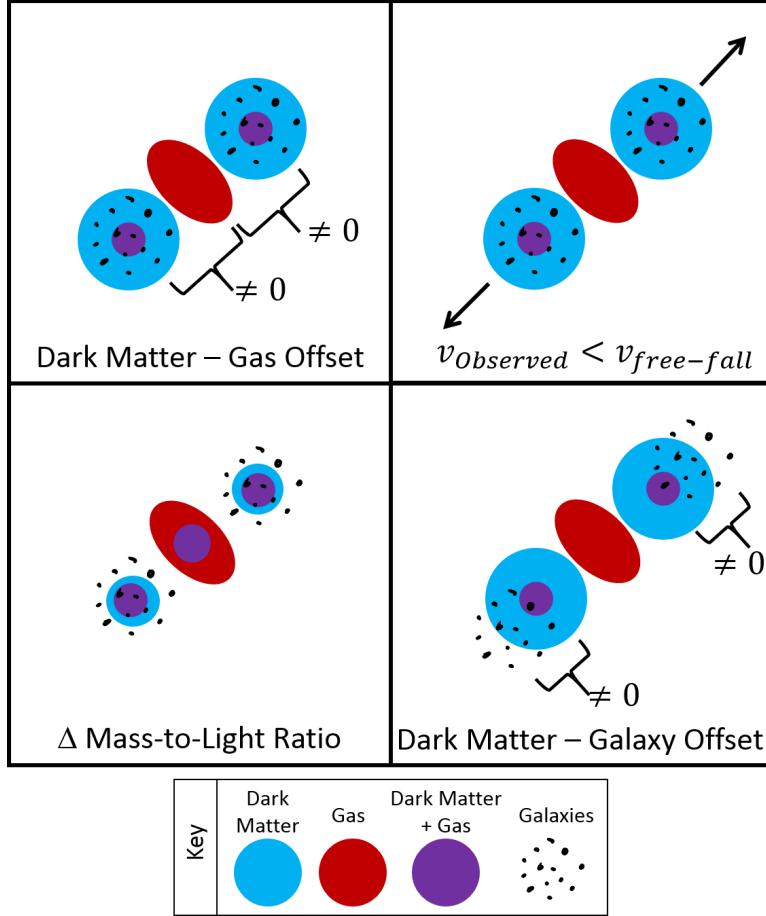


Figure 1.2: The three means of constraining σ_{SIDM} with merging clusters, originally outlined by Markevitch et al. [93] and fourth developed by Randall et al. [127]. *Upper Left:* If the DM is significantly offset from the gas then the scattering depth of the dark matter (τ_{DM}) must be less than the scattering depth of the gas (τ_{gas}) and an upper limit can be placed on σ_{SIDM} . *Upper Right:* If DM self-interacts during the merger, then the velocity of each subcluster will be slowed to some degree. Thus if the observed velocity (v_{obs}) is found to be consistent with the free-fall velocity ($v_{\text{free-fall}}$) an upper limit can be placed on σ_{SIDM} . If however v_{obs} is significantly less than $v_{\text{free-fall}}$, an upper limit could be potentially placed on σ_{SIDM} . *Lower Left:* If DM self-interacts during the merger, then some fraction of the DM particles will scatter and become unbound from each subcluster. Thus the mass-to-light ratio of each subcluster can be compared with the mass-to-light ratio of similar non-merging clusters, and depending on whether the mass-to-light ratio of the merger is the same or less than the non-merging clusters' mass-to-light ratio, then respectively an upper limit or lower limit can be placed on σ_{SIDM} . *Lower Right:* If the DM self-interacts during the merger, then the DM component of each subcluster will experience an additional drag force and will travel at a slower velocity than the respective subcluster galaxies. Thus depending on whether a significant offset between the galaxies and DM is or is not observed, then respectively a lower limit or upper limit can be placed on σ_{SIDM} .

existing $\sigma_{\text{SIDM}} m_{\text{DM}}^{-1}$ by the necessary order of magnitude would require clusters with surface mass densities an order of magnitude higher than both the Bullet Cluster and Abell 2744. Such clusters are highly unlikely to exist, thus this method has little value for future constraints of SIDM.

1.5.2.2 Velocities of the Subclusters

Markevitch et al. [93] noted that the Bullet Cluster merger velocity inferred from the X-ray gas shock feature “is in good agreement with the expected free-fall velocity”. They then argued that if DM self-interacts then each subcluster will decelerate, resulting in a velocity difference between the observed velocity, v_{obs} , and the free-fall velocity, $v_{\text{free-fall}}$:

$$v_{\text{obs}} - v_{\text{free-fall}} = \frac{\bar{p}}{m_{\text{DM}}} \frac{\sigma_{\text{SIDM}}}{m_{\text{DM}}} \Sigma_{\text{DM}},$$

where \bar{p} is the average momentum lost by the subcluster in each particle collision.

This method has only been applied to the Bullet Cluster [93], and resulted in a constraint of $\sigma_{\text{SIDM}} m_{\text{DM}}^{-1} \lesssim 7 \text{ cm}^2 \text{ g}^{-1}$. The predominant reason this method has not been applied to more mergers is that it is very difficult to constrain the three-dimensional velocity of the merger [40], which is necessary to estimate \bar{p} . Often times the only direct observation of the merger velocity comes from spectroscopic redshifts of the subcluster galaxies, and these only provide information about the line-of-sight velocity component of the merger. In the case of the Bullet Cluster however, the X-ray gas has been shocked due to the merger velocity being greater than the sound speed of the gas. From this shock Markevitch et al. [94] were able to estimate the Mach number of the merger, which in turn provided them with an estimate of the three-dimensional merger velocity. Most clusters do not have such a well defined shock feature.

While it was originally believed that the three-dimensional merger velocity could be inferred from the X-ray shock feature, Springel & Farrar [143] showed that the X-ray shock inferred velocity significantly overestimates the true three-dimensional merger velocity. This coupled with the fact that v_{obs} is expected to vary throughout the merger and always be less than $v_{\text{free-fall}}$ suggests that the existing constraints from this method should be questioned. Furthermore it seems unlikely that the constraints will ever improve upon existing SIDM constraints.

1.5.2.3 Mass-to-Light Ratio

Markevitch et al. [93] noted that if DM self-interacts during the merger, then some fraction of the DM particles will scatter and become unbound from each subcluster. Thus the mass-to-light ratio (M/L) of each subcluster can be compared with the M/L of similar non-merging clusters, and depending on whether the M/L of the merger is the same or less than the non-merging clusters' M/L , then respectively an upper limit or lower limit can be placed on σ_{SIDM} . Clowe et al. [30] claim that the M/L of the Bullet Cluster are in “good agreement with the universal cluster values from the lensing analyses [e.g., 36, 96].” This enabled Markevitch et al. [93] to place a constraint of $\sigma_{\text{SIDM}} m_{\text{DM}}^{-1} \lesssim 1 \text{ cm}^2 \text{ g}^{-1}$. Randall et al. [127] were able to improve upon this constraint by simulating the Bullet Cluster with collisionless “galaxy” particle and collisional SIDM particles and by varying σ_{SIDM} between collisions. They found that for $\sigma_{\text{SIDM}} m_{\text{DM}}^{-1} < 0.7 \text{ cm}^2 \text{ g}^{-1}$, otherwise the M/L decreased by more than $\sim 23\%$ in their simulation, which they claimed was not reasonable given the measured M/L of the subclusters.

While this method has provided the tightest $\sigma_{\text{SIDM}} m_{\text{DM}}^{-1}$ constraints there are a number of assumptions and possible systematic errors to consider more seriously. First and foremost the method assumes that all clusters have close to the same ($\lesssim 40\%$ difference) M/L . However as Dahle [36] shows there is significant variance in the M/L of galaxy clusters with $100 \lesssim h(M/L) \lesssim 1000$. Secondly, it is well established that galaxy clusters play an important role in the evolution of their member galaxies, but it is still unclear whether cluster mergers trigger star formation [e.g. 52, 74, 102, 118], quench it [123], or have no immediate effect [27]. Thus it is unclear what affects the cluster merger will have on the luminosities of the subclusters. Finally there are a number of systematic errors [112, 127, discuss several] that can affect the gravitational lensing estimated mass. Because of these issues caution should be used when applying this method to constrain SIDM.

1.5.2.4 Dark Matter - Galaxy Offset

The method introduced by Randall et al. [127] is based upon the fact that if DM self-interacts during the merger, then the DM component of each subcluster will experience an additional drag force and will decelerate with respect to the respective subcluster galaxies. Initially this velocity difference will result in a DM-galaxy offset that increases with time.

Thus depending on whether a significant offset between the galaxies and DM is or is not observed, then respectively a lower limit or upper limit can be placed on σ_{SIDM} .

Using the same galaxy-DM simulations referenced in §1.5.2.3 Randall et al. [127] found, as expected, that as they increased σ_{SIDM} the offset between their collisionless “galaxy” particles and there SIDM particles increased. Then given the observed galaxy and lensing centroids and the uncertainty on these centroids they claimed they could rule out any scenarios where SIDM resulted in an offset greater than ~ 50 kpc. This corresponded to a constraint of $\sigma_{\text{SIDM}} m_{\text{DM}}^{-1} < 1.25 \text{ cm}^2 \text{ g}^{-1}$. Interestingly Randall et al. [127] note that the observed galaxy centroid is leading the lensing mass centroid by $5.7'' \pm 6.6''$ (25 ± 29 kpc), yet rather than try to estimate the value of $\sigma_{\text{SIDM}} m_{\text{DM}}^{-1}$ based on this offset they only took the extreme and fit an upper limit. According to their simulations an offset of ~ 25 kpc is seen in their simulation with $\sigma_{\text{SIDM}} m_{\text{DM}}^{-1} \approx 0.7 \text{ cm}^2 \text{ g}^{-1}$. Granted that with offset uncertainties of order the measured offset there is little confidence in this estimate.

This method has the advantage that the scales of interest are typically $\gtrsim 25$ kpc. Thus this method is less subject to the baryonic degeneracies that weaken the constraining power of other SIDM constraining methods (e.g. central halo density). The method does have a number of sources of noise and systematic error that need to be considered, in addition to the Poisson noise of the centroid measurements. The important offset for this method is the three-dimensional offset between the galaxies and the DM. What can be measured is the projected offset between the galaxies and the lensing centroid. As will be discussed in Chapter 4 there is considerable uncertainty when converting between projected and three-dimensional distances of merging cluster systems. While this uncertainty is not important for determining if there is a significant offset between the galaxies and dark matter (that would suggest $\sigma_{\text{SIDM}} > 0$) it is important if we wish to quantify $\sigma_{\text{SIDM}} m_{\text{DM}}^{-1}$. The other key limitation is that we cannot directly measure the DM centroid, we are only able to measure the total projected mass with gravitational lensing. The lensing centroid can then diverge from the DM centroid for a number of reasons. The fact that these are dissociative mergers means that $\sim 10\%$ of the cluster mass is in between the two subclusters. This gas mass will act to pull the lensing centroid away from the DM centroid towards the center of the cluster. This systematic effect will exactly mimic the effect expected if DM self-interacts. Similarly

the mass of one subcluster will pull the lensing centroid of the other subcluster away from the DM centroid and towards the center. This effect may be countered to some degree since the galaxy centroid will experience a similar effect. Without simulations it is unclear if these two effects will completely null one another. Finally, lensing is sensitive to all mass along the line of sight. Thus foreground or background large scale structures could cause a random offset in the lensing centroid from the DM centroid of the subcluster. Dietrich et al. [44] found that projected large scale structure results in a $\sim 4''$ random offset of the lensing centroid from the true DM centroid. As will be discussed in Chapter 4 these sources of noise and systematic error can be mitigated. Thus it seems as though this method holds the most promise for constraining $\sigma_{\text{SIDM}} m_{\text{DM}}^{-1}$.

Chapter 2

Musket Ball Cluster: Observed Properties

This chapter is an expanded version of the article titled *Discovery of a Dissociative Galaxy Cluster Merger with Large Physical Separation* which was published in the March 2012 issue of the Astrophysical Journal Letters (Dawson et al., 2012, Volume 747, pp. L42).

We present DLSCL J0916.2+2951 ($z=0.53$), a major cluster merger in which the collisional cluster gas has become dissociated from the collisionless galaxies and dark matter. We identified the cluster using optical and weak lensing observations as part of the Deep Lens Survey. Our follow-up observations with *Keck*, *Subaru*, *Hubble Space Telescope*, and *Chandra* show that the cluster is a dissociative merger.

2.1 Introduction

We have identified a new dissociative merger, DLSCL J0916.2+2951, that probes an unexplored area of merger phase-space. We originally detected the cluster in the Deep Lens Survey [DLS; 166] via its weak lensing (WL) shear signal. It consists of two main subclusters spectroscopically confirmed to be at the same redshift (0.53). This cluster was also observed in the Sunyaev-Zel'dovich Array Survey [107] which provided evidence that the cluster gas is dissociated from the bulk of the mass and galaxies (Figure 2.6). Follow-up optical observations with *Subaru* and *HST* enable higher resolution mass maps and follow-up X-ray observations with *Chandra* ACIS-I confirm that the majority of the gas is offset between the

North and South subclusters, the signature of a dissociative merger (Figure 2.1).

In this chapter we introduce DLSCL J0916.2+2951 and summarize our survey of its three dominant components (galaxies, DM, and gas) and the cluster’s astrophysical implications. A more thorough exposition of the survey and analysis will be presented in Dawson et al. (in preparation). Throughout this dissertation we assume $\Omega_\Lambda = 0.7$, $\Omega_m = 0.3$, and $H = 70 \text{ km s}^{-1} \text{ Mpc}^{-1}$.

2.2 Photometric Studies

We obtained B , V , R , and z' photometric data (12, 12, 18, and 12 ksec, respectively) with Mosaic 1 on the KPNO 4-m *Mayall* telescope as part of the DLS. To improve the accuracy of our photometric redshifts we also observed the cluster in three medium-width optical bands (g , h , and i from the BATC filter set), bracketing the redshifted 4000 Å feature, using the upgraded Mosaic 1.1 imager on the KPNO *Mayall* with exposure times of 6 ks per filter (2011 April 22–24). We estimate colors using *ColorPro* [31] and redshifts using *BPZ* [11]. We replace the standard templates with a set “tweaked” in a method similar to that described in Ilbert et al. [75], using spectroscopic samples from SHELS [57] and the PRIMUS survey [32] which overlap the DLS. Figure 2.2 shows the density isopleths of galaxies with $0.43 < z_{\text{phot}} < 0.63$ (roughly the cluster redshift $\pm \sigma_{z_{\text{phot}}}$). This map agrees well with the distribution of spectroscopically confirmed cluster members.

2.3 Spectroscopic Studies

We obtained spectroscopic redshifts for 20 cluster members with *Keck* LRIS (2007 January 16) and 634 unique spectroscopic redshifts ($0 < z < 1.2$) in a $\sim 15' \times 15'$ area centered on the cluster with *Keck* DEIMOS (2011 March 2–3), including 132 members at the cluster redshift. We reduced the LRIS spectra using a scripted sequence of standard IRAF reduction tasks, and the DEIMOS spectra using a modified version of the DEEP2 *spec2d* package [39, 55, 87].

We use our full sample of 654 spectroscopic redshifts as well as photometric redshifts to identify potential line-of-sight structures which may confuse our results. We find no evidence for significant line-of-sight structure (Figure 2.2).

We estimate each subcluster’s redshift and velocity dispersion (Table 2.1) using the

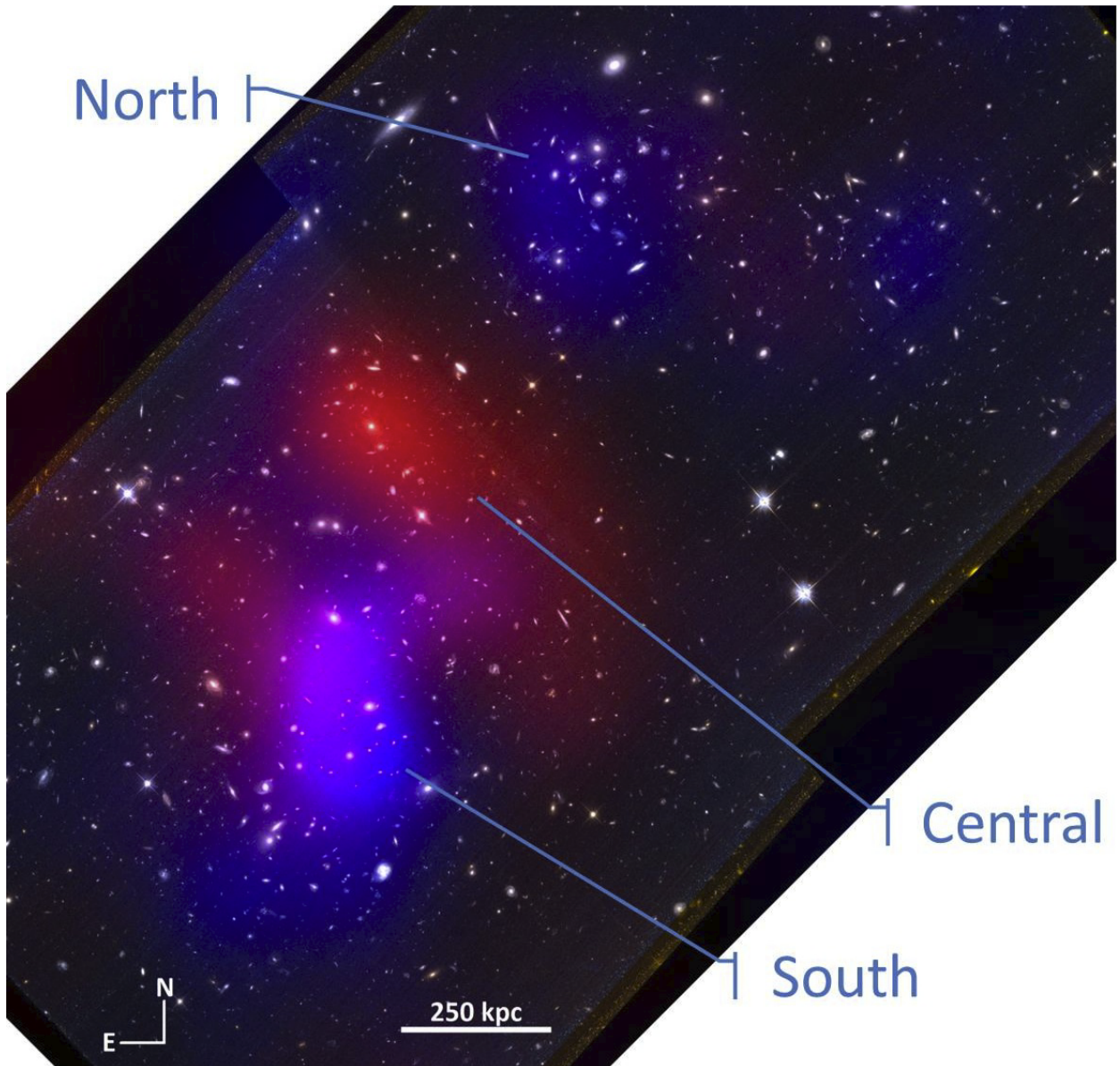


Figure 2.1: Merging cluster DLSCL J0916.2+2951 and its three matter components. Overlaid on the HST color image of the galaxies is the total mass distribution (blue) based on WL analysis of the HST images and the cluster gas distribution (red) based on Chandra X-ray observations. The bulk of the collisional gas is located between the two collisionless galaxy and mass concentrations, indicative of a dissociative merger. The image is $5' \times 5'$ ($\sim 1.9 \times 1.9 \text{ Mpc}^2$ at $z = 0.53$).

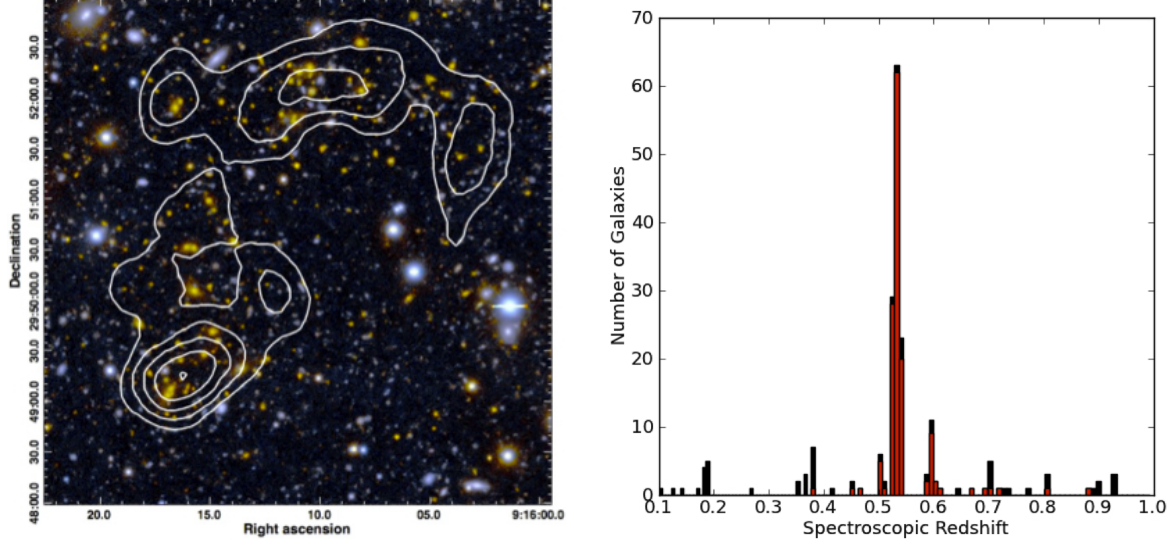


Figure 2.2: *Left:* DLS composite BVR color image of DLSCL J0916.2+2951 showing the galaxies of the two subclusters. The white contours represent the number density of galaxies with $z_{\text{phot}} = 0.53 \pm 0.1$, the cluster redshift $\pm \sigma_{z_{\text{phot}}}$. The contours begin at $200 \text{ galaxies Mpc}^{-2}$ with increments of $50 \text{ galaxies Mpc}^{-2}$. The image field-of-view is the same as Figure 2.1. *Right:* Histogram of the 200 observed spectroscopic redshifts within the field of view of the *left* figure. The red portion is the subsample that passes the $z_{\text{phot}} = 0.53 \pm 0.1$ criteria. The galaxies at $z \sim 0.6$ had equal probability of selection as the cluster members and show no sign of clustering.

biweight-statistic and bias-corrected 68% confidence limit [9] applied to 100,000 bootstrap samples of each subcluster’s spectroscopic redshifts. Our redshift estimates indicate a line-of-sight velocity difference of $v_{\text{los}} = 670^{+270}_{-330} \text{ km s}^{-1}$ between the North and South subclusters, using the galaxies within a 0.5 Mpc radius centered on the *HST* WL mass peaks and within a velocity range of $\pm 3000 \text{ km s}^{-1}$ of $z=0.53$ ($\sim 3 \times$ the expected velocity dispersion); corresponding to 38 and 35 galaxies for the North and South subusters, respectively. These results are robust against varying the velocity range $\pm 1000 \text{ km s}^{-1}$ and using the Subaru WL or galaxy number density peaks as the apertures’ centers, provided the aperture radius is $\lesssim 0.5 \text{ Mpc}$: larger radii lead to significant subcluster membership confusion. Additionally, we report the velocity dispersion mass estimates based on the scaling relation of Evrard et al. [48] in Table 2.1. We note that the velocity dispersions should be interpreted with caution since this is a disturbed system.

Table 2.1. Observed subcluster and X-ray concentration properties

Subcluster	Redshift	σ_v (km s ⁻¹)	σ_v M ₂₀₀ (10 ¹⁴ M _⊙)	WL M ₂₀₀ (10 ¹⁴ M _⊙)	L _{X,0.5–2keV} (10 ⁴³ erg s ⁻¹)	T _X (keV)	X-ray S/N	Joint WL S/N
North	0.53074 ^{+0.00068} _{-0.00064}	740 ⁺¹³⁰ ₋₁₉₀	3.7 ± 2.3	1.7 ^{+2.0} _{-0.72}	0.63	...	3.2	3.0
South	0.53414 ^{+0.00065} _{-0.00064}	770 ⁺¹¹⁰ ₋₉₂	4.1 ± 1.6	3.1 ^{+1.2} _{-0.79}	2.1	2.7 ^{+1.2} _{-0.7}	7.0	6.7
Central	2.8	2.2 ^{+1.4} _{-0.6}	9.1	-3.3 ^a

^aThe negative WL S/N indicates a projected surface mass local under-density.

2.4 Weak Lensing Analysis

To map the total mass distribution we use a version of the Fischer & Tyson [53] method modified to include a novel tomographic signal-matched filter. The cluster's WL shear signal, γ , depends not only on the projected surface mass over-density of the cluster, $\Delta\Sigma$, but on the relative distances of the observer, the mass, and the background galaxies:

$$\gamma = \frac{\Delta\Sigma}{\Sigma_{cr}} = \frac{\Delta\Sigma 4\pi G}{c^2} \frac{D_{ls}(z_l, z_s) D_l(z_l)}{D_s(z_s)} \mathcal{H}\left(\frac{z_s}{z_l} - 1\right), \quad (2.1)$$

where Σ_{cr} is the critical surface density, \mathcal{H} is the Heaviside step function, and D_l , D_s , & D_{ls} are the angular diameter distances to the lens, source, and between the lens and source, respectively. In addition to weights based on shape measurement errors, we also weight by each galaxy's photometric redshift probability distribution function, $p(z)$,

$$w_\gamma(z_l) = \Sigma_{cr}^{-1}(z_l) \approx \langle \Sigma_{cr}^{-1}(z_l) \rangle = \int \Sigma_{cr}^{-1}(z_l, z_s) p(z_s) \mathcal{H}\left(\frac{z_s}{z_l} - 1\right) dz_s.$$

This method increases the signal-to-noise of the measurement [see e.g. 71], and more accurately accounts for the errors inherent in the photometric redshift estimates, compared to single-point estimates. We estimate uncertainties using 100 bootstrap resamplings.

Encouraged by the DLS mass and galaxy maps we obtained higher-resolution ground and space based observations. *Subaru* Suprime-Cam i' -band coverage of the cluster was provided by engineering-time observations of DLS Field 2 (2008 January 8). We use the Suprime-Cam data reduction software *SDFRED* [117, 167] followed by *SCAMP* & *SWARP* [13, 14] to refine the astrometry and make the final mosaic. DLSCL J0916.2+2951 was also

observed with *HST* ACS/WFC using F606W and F814W filters (GO-12377, PI-W. Dawson) in a 2×1 pointing mosaic that covers the subclusters (Figure 2.1). The exposure times for F606W and F814W are 2520s and 4947s per pointing, respectively. We reduce this data following a method similar to that presented in Jee & Tyson [78]. We measure the PSF of both datasets using the PCA method presented in Jee et al. [76].

We perform our WL analysis independently on both the Subaru and HST F814W data. The Subaru data has $0.72''$ seeing and 49 WL-quality source galaxies (i.e. background galaxies with measured ellipticity error < 0.3) per arcmin 2 . For the mass map we use an apodizing kernel radius of $0.5'$, which can be interpreted as the effective resolution of the WL mass map. We are able to cross-match most of the detected objects with the DLS and use the $p(z)$'s discussed in the previous section.

Cross-matching is more problematic with the higher-resolution HST data, so we use a color-magnitude cut ($F606W - F814W < 0.8$ and $24 < F814W < 28.5$) to select source galaxies and exclude cluster red-sequence and bright foreground galaxies, see Figure 2.3. For the WL analysis of the HST F814W image, which has a $0.1''$ PSF and 136 WL-quality source galaxies per arcmin 2 , we use an apodizing kernel radius of $3.6''$. We find no significant spatial correlation between source density and subcluster position, suggesting that our source galaxy population is not significantly contaminated with cluster galaxies. Furthermore, we find a comparable number distribution of sources as a function of magnitude when we make similar cuts to the HUDF [31] and GOODS North & South [61] galaxy catalogs, indicating negligible cluster contamination, see Figure 2.4. We estimate the $p(z)$ of our HST source galaxy sample by assuming the photometric redshift distribution of the Coe et al. [31] HUDF catalog after applying our color-magnitude cut. Figure 2.5 shows excellent agreement between the Subaru and HST WL mass, and galaxy density maps.

We construct a joint catalog from the HST and Subaru data, using the HST data where available and Subaru for the surrounding area. Using a tomography-based MCMC analysis we simultaneously fit NFW halos centered on the North and South HST WL peaks, and use the Gelman & Rubin [58] convergence test applied to eight independent chains. In order to reduce the number of free parameters we use the Duffy et al. [46] empirical relation between M_{200} and concentration. We present the most likely masses for each halo along with the

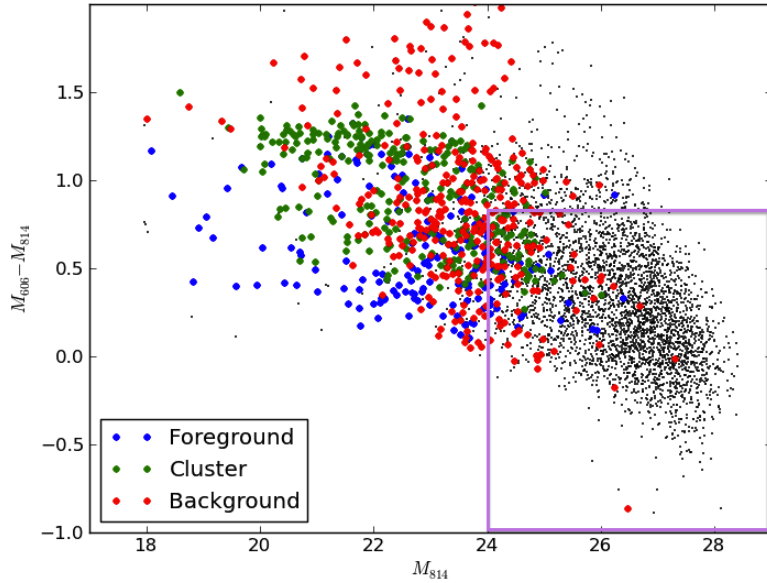


Figure 2.3: Musket Ball Cluster color-magnitude diagram based on HST photometry. The larger color points are cross-matched DLS objects which have been divided into *Foreground* (blue; $z_{\text{phot}} < 0.43$), *Cluster* (green; $z_{\text{phot}} = 0.53 \pm 0.1$), and *Background* (red; $z_{\text{phot}} > 0.63$) samples. Note that the photometric redshifts become relatively unreliable for $M_{814} > 24$. The purple box indicates the HST source galaxy sample.

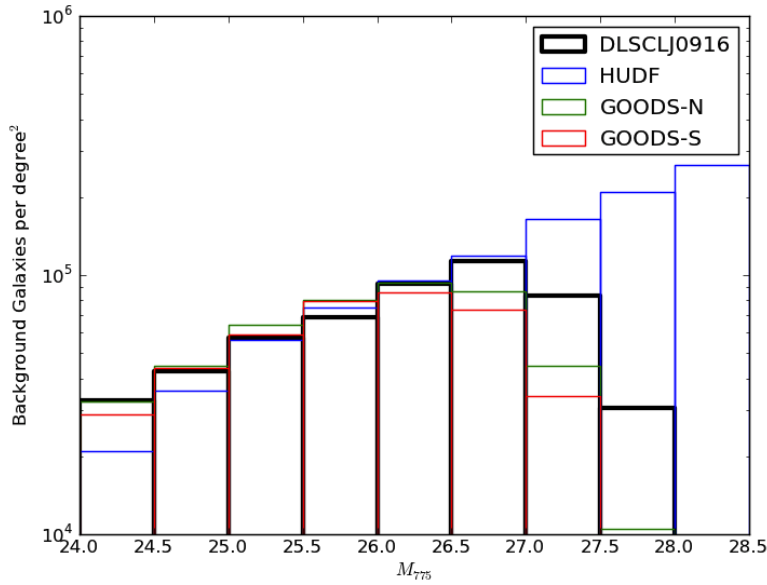


Figure 2.4: Comparison of the Musket Ball Cluster, HUDF [31] and GOODS North & South [61] source galaxy densities. The HUDF field has a depth of 288 F775W orbits, the GOODS survey has a depth of one F775W orbit, and the Musket Ball Cluster has a depth of 2 F814W orbits (the F814W filter is conservatively wider than the F775W filter). Up to the completeness of each survey we find a comparable number distribution of sources as a function of magnitude when we make similar cuts to each galaxy catalog, indicating negligible cluster contamination.

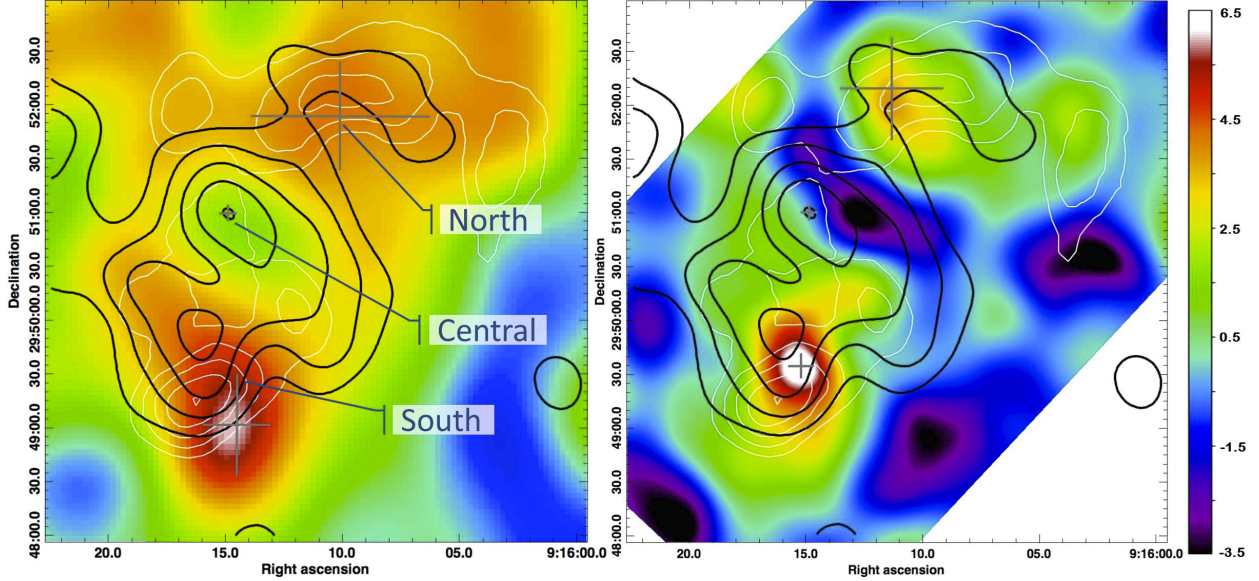


Figure 2.5: Comparison of the Subaru i' -band ground-based (left) and HST space-based (right) WL mass signal-to-noise maps (color) of DLSCL J0916.2+2951 with the X-ray distribution (bold black contours) and galaxy number density (white contours, same as Figure 2.2). The peak centers and corresponding one sigma errors are denoted by the gray cross-hairs. In both analyses there is general agreement between the location and relative magnitude of galaxies and WL yet the majority of the cluster gas is centered $\sim 1.4'$ between the North and South subclusters in a local mass underdensity, providing evidence that the North and South subclusters have undergone the first pass-through of a major merger. Note however that the Subaru southern WL peak is located further south than the HST WL peak; this is important to keep in mind during the Chapter 4 discussion. The scale of each map is equivalent and the image field-of-view is the same as Figures 2.1 & 2.2. The map created from the joint Subaru/HST catalog looks nearly identical to the HST map, with only slight variations in the scale (see Table 2.1).

bias-corrected 68% confidence limits in Table 2.1. We also compare the integrated projected surface mass density of the NFW halos with the measured WL aperture mass [49] of each subcluster and find agreement within a radius of 0.5 Mpc of each subcluster.

2.5 Sunyaev–Zel’dovich Effect Studies

This cluster was also observed in the Sunyaev-Zel’dovich Array Survey [107]. They found a 4σ SZE signal roughly consistent with that expected for clusters of this mass. The signal is offset $\sim 1'$ (~ 0.4 Mpc) from the southern subcluster and $\sim 3'$ (~ 1 Mpc) from the northern subcluster. The SZE traces the cluster ICM and can be used to identify an offset of the ICM relative to the galaxies and dark matter [as in the case of the Bullet Cluster 68]. This shift provided the first evidence that the cluster gas is dissociated from the bulk of the mass and

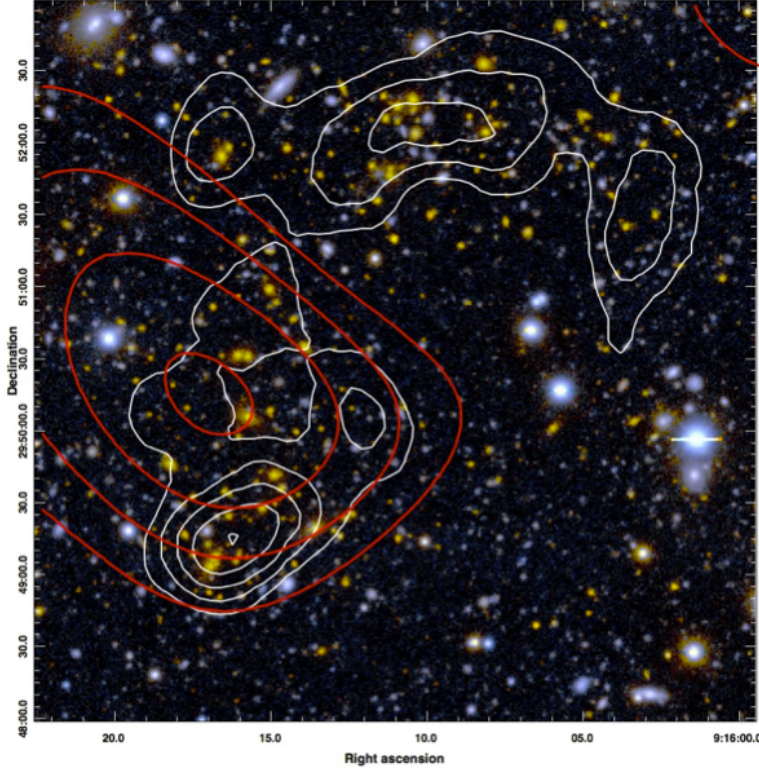


Figure 2.6: DLS composite BVR color image of DLSCL J0916.2+2951 showing evidence that the cluster gas, represented by the solid red SZE decrement significance contours (1, 2, 3, 4 σ), is offset $\sim 1'$ (~ 0.4 Mpc) and $\sim 3'$ (~ 1 Mpc) from the two subclusters, represented by the white galaxy number density contours for galaxies with $z_{\text{phot}} = 0.53 \pm 0.1$ (beginning at 200 galaxies Mpc^{-2} with increments of 50). The image field-of-view is the same as Figure 2.1. The beam of the SZ observation has a radius of $\sim 1'$.

galaxies (Figure 2.6).

2.6 X-ray Studies

We acquired X-ray spectral-imaging of the cluster with 40ks of *Chandra* ACIS-I time (GO-12800854, PI Dawson), and reduce it using *CIAO* version 4.2 and *CALDB* version 4.4.1. We manually identify X-ray point sources and mask them before adaptively smoothing the diffuse emission, we present the resulting map in Figure 2.7. We estimate source counts and their error using the *dmextract* function of *CIAO*. We use an $8'$ radius background region which encloses the subcluster regions and rests $\sim 90\%$ on ACIS-I3 (on which the subclusters are observed). In the estimate of the background counts each subcluster region, chip gap, and point source are excluded. The subcluster exclusion regions were defined such that they encompassed the source emission and were extended out to approximately the SNR =

1 level based on the smoothed map. In total we there were 1800 ± 40 background counts in 620,000 pixel² area within the energy range of 0.5-2 keV. For the South and Central X-ray concentrations (120 ± 17 and 170 ± 19 detected 0.5-2 keV photons, respectively) we use the *Xspec* X-ray spectral fitting tool [6] to fit a Mewe-Kaastra-Liedahl plus photoelectric absorption model [fixed to the Leiden/Argentine/Bonn value; 81] to the X-ray spectrum of each X-ray concentration. For the North concentration there are not enough detected X-ray photons (38 ± 12) to fit a meaningful spectrum. We report the results of this analysis in Table 2.1. We define the subcluster exclusion regions such that they encompass the source emission and extend out to approximately the 1σ level based on the smoothed map. In total there are 1800 ± 40 background counts in the 620,000 pixel² area and 0.5-2 keV energy range. For the North, South, and Central X-ray concentrations we find 38 ± 12 , 120 ± 17 and 170 ± 19 detected 0.5-2 keV photons, respectively.

To estimate the temperatures of the South and Central concentrations we use the *Xspec* X-ray spectral fitting tool [6] to fit a Mewe-Kaastra-Liedahl plus photoelectric absorption model [fixed to the Leiden/Argentine/Bonn value; 81] to the X-ray spectrum of each X-ray concentration. For the North concentration there are not enough detected X-ray photons to fit a meaningful spectrum. Due to the low count regime and our use of the χ^2 statistic we rebin the data so that each spectral channel used in the fit contains at least 20 counts. The binning is carried out on the spectra before background subtraction; these raw spectra contained 843 (1070) counts in the South (Central) subcluster. Since the background spectrum contains 7725 counts, each spectral bin in the background is far above the 20 count threshold. Binning data in this manner does reduce the spectral resolution, however for hot clusters like those in our study the number of final spectral bins we have (31 for the southern and 39 for the central subcluster, which include cuts on the highest energy channels) are sufficient to determine the temperature, since the spectrum is dominated by bremsstrahlung emission which has few sharp spectral features. We report the results of this analysis in Table 2.1.

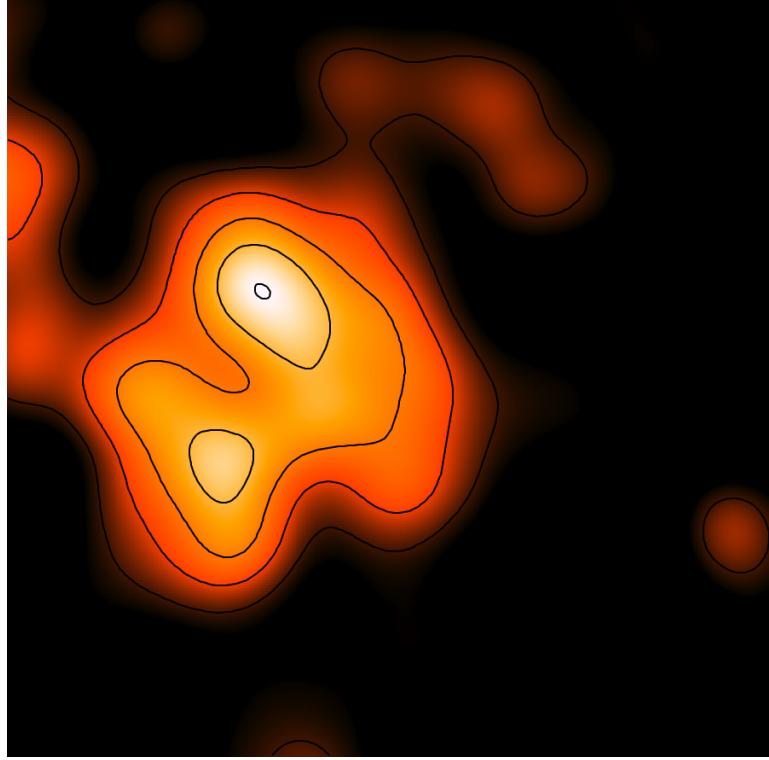


Figure 2.7: Chandra ACIS-I 40 ks adaptively smoothed X-ray image of DLSCL J0916.2+2951. The image field-of-view is the same as Figure 2.1. The contours are evenly spaced on an arbitrary linear scale and are used throughout this dissertation when comparing the gas map with other components.

2.7 Radio Studies

Since the Musket Ball cluster is a strong merger with an X-ray inferred¹ Mach number of > 3 whose axis is likely to be close to the plane of the sky [40, and presented in Chapter 3], it is a prime candidate for a double radio relic. Radio relics are irregularly shaped radio sources, located at the outskirts of galaxy clusters, characterized by a steep radio spectrum² with $\alpha \leq -1.2$. Radio relics are thought to be produced by relativistic particles that have been accelerated by shock waves in the ICM. Double relics show relics on opposite sides from the cluster center and form a subset of relics for which the merger geometry can be constrained particularly well [see e.g. 15].

Since the Musket Ball Cluster is at a later stage than all other dissociative mergers [41] and is thought to have shocks with $M > 3$, the detection of radio relics would provide

¹The estimated Mach number is based on the X-ray temperature of the gas (Table 2.1) and estimated collision velocity of the merger (Table 3.3).

²The spectrum is defined as $S(\nu) \propto \nu^\alpha$.

constraints on the merger geometry. This has direct implications for the measurement of the dark matter cross-section with the Musket Ball since observed projected offsets must be translated into meaningful physical offsets [see e.g. 40]. The degree of polarization provides important information on the angle of the shock surface and the line of sight and together with the location of the relics with respect to the X-ray position we can constrain the geometry of the merger axis to within 10 degrees [152]. Furthermore, the cluster makes an ideal target to study the evolution of radio relics, due to its superior temporal lever arm, with ramifications for the theory of particle acceleration.

The Musket Ball Cluster is located at $z = 0.53$ and at this redshift a typical moderate luminosity radio relic has a flux density of 0.3 mJy at $z = 0.53$ and 1.4 GHz [114, 152]. This is well below both the NRAO VLA Sky Survey (NVSS) and Westerbork Northern Sky Survey (WENNS) sensitivities, thus an existing non-detection in these surveys is not surprising.

We observed the Musket Ball Cluster with the Westerbork Synthesis Radio Telescope (WSRT) in 2013 January 23-28 for a total of 24 hours. We used the standard 21 cm L-band as it is the most sensitive system at the WSRT. The observations have a resolution of about 15x30 arcsec, corresponding to a physical size of 100x200kpc at $z = 0.53$, enough to resolve a 1 Mpc relic (relic sizes range between 0.5 and 2 Mpc). With two full synthesis runs we achieved a noise level of $20 \mu\text{Jy}/\text{beam}$ in the continuum, and about $10 \mu\text{Jy}/\text{beam}$ in Stokes Q and U. This should enable us to detect a 0.3 mJy relic, covering 5 beam areas, with an SNR of 10.

While there are a number of compact sources associated with the merging cluster (see the X 's in Figure 2.8), we find no evidence for diffuse radio emission associated with the merging cluster. In other words, no radio halos or relics are detected in the Musket Ball Cluster merger. All previously discovered radio relics have been in clusters with X-ray luminosities in the range of $10^{44}\text{-}10^{45} \text{ erg s}^{-1}$. The Musket Ball Cluster has an X-ray luminosity of $\sim 10^{43} \text{ erg s}^{-1}$ (see Table 2.1). This null detection is in line with current observations suggesting that radio relics are only found in very massive cluster mergers, although without better measurements of the cluster merger velocity and gas sound speed there remains the possibility that the merger Mach number $\gtrsim 3$ is an overestimate.

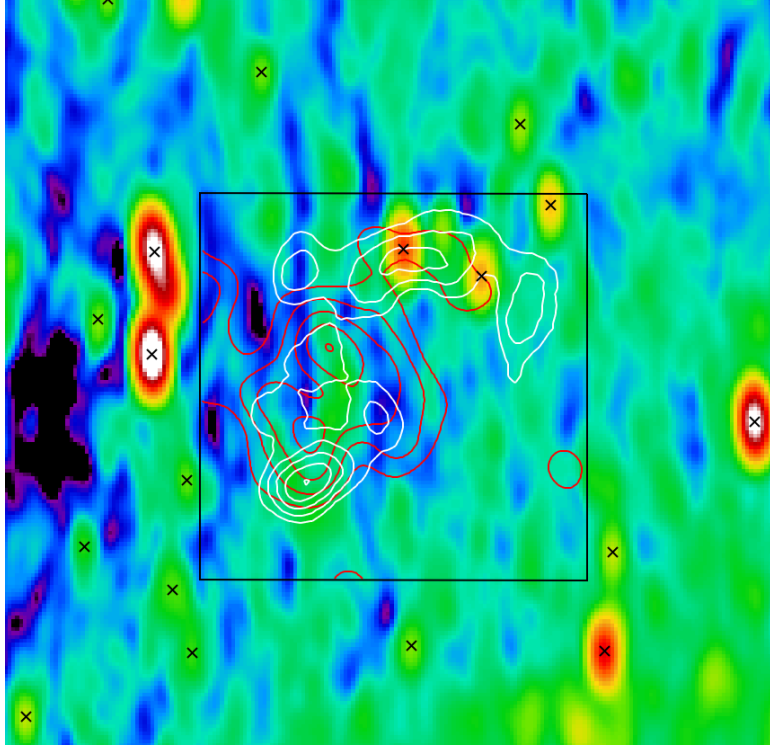


Figure 2.8: Westerbork Synthesis Radio Telescope 21cm L-band image of the Musket Ball Cluster and surrounding area. The color image has an arbitrary log-scale. Likely compact radio sources are denoted by the X points, and from these the north/south elongated PSF can be seen. The black box shows the area corresponding to Figures 2.1, 2.2, and 2.5. Similarly the white contours are the galaxy number density contours from Figure 2.2, and the red contours are the X-ray contours from Figure 2.5. We detect no significant diffuse radio emission associated with the Musket Ball Cluster (i.e. no radio halos or relics are detected).

2.8 Cluster Merger Scenario

The peak of the gas distribution ($09^{\text{h}}16^{\text{m}}15^{\text{s}} \pm 5.5^{\text{s}}, 29^{\circ}50'59'' \pm 5.0''$) derived from X-rays is offset $1.4' \pm 0.49$ from the North HST WL mass peak ($09^{\text{h}}16^{\text{m}}10^{\text{s}} \pm 30^{\text{s}}, 29^{\circ}52'10'' \pm 30''$), and $1.4' \pm 0.14$ from the South HST WL mass peak ($09^{\text{h}}16^{\text{m}}15^{\text{s}} \pm 8.0^{\text{s}}, 29^{\circ}49'34'' \pm 6.9''$), and is located near a local minimum in the mass, suggesting that the subclusters have a small impact parameter and have experienced at least their first pass-through along a north-northwest merger direction (see Figure 2.5). Additionally the central X-ray concentration has a temperature (Table 2.1) in line with an $M_{500} = 0.9_{-0.3}^{+1.1} \times 10^{14} M_{\odot}$ potential [156], but the WL data suggests that there is a local under-density of mass at this concentration incapable of supporting such a temperature. Further evidence for the merger scenario is provided by the morphology of the gas. Simulations [124, 136] predict that the gas morphology elongates

transverse to the merger direction after pass-through for mergers with small impact parameters. The Central gas concentration appears to be oblate and roughly perpendicular to the axis connecting the North and South mass peaks. This is consistent with the interpretation that these two subclusters have experienced their first pass-through and that the merger axis being roughly in the plane of the sky.

2.9 Discussion

While we use DLSCL J0916.2+2951 to provide further evidence for the canonical DM model and independently constrain $\sigma_{\text{DM}} m_{\text{DM}}^{-1}$, we believe that its greatest value is as a probe for a new and special phase of cluster formation. It provides a greatly improved temporal lever-arm with which to guide numerical simulations that explore the major merger phase. This is potentially important given that much of our knowledge of the cluster merger process comes from numerical hydrodynamic simulations [e.g. 124], which are used to place the tightest constraints on $\sigma_{\text{DM}} m_{\text{DM}}^{-1}$ [$< 0.7 \text{ cm}^2 \text{ g}^{-1}$; 127] and bring observed merger velocities (inferred from the observed shock velocity) more in line with the expectations of Λ CDM [86, 143]. Secondly, the large projected separation relative to the virial radii of the subclusters ($R_{200} \sim 1 \text{ Mpc}$) enables the deconvolution of the subclusters from the Central region and direct comparison of the physical properties of each. This will provide new insight into the behavior of the cluster constituents (gas, galaxies, & DM) during a major merger. For example, it is well established that galaxy clusters play an important role in the evolution of their member galaxies, but it is still unclear whether cluster mergers trigger star formation [e.g. 52, 74, 102, 118], quench it [123], or have no immediate effect [27].

Our identification of DLSCL J0916.2+2951 as a dissociative merging system using only optical, WL, and SZE observations shows that these systems can be found independent of X-ray observations. This has implications for finding more of these systems when the existing SZE surveys, e.g. ACT [72] and SPT [132], are coupled with upcoming and overlapping deep optical/WL surveys, e.g. DES [145] and LSST [149].

acknowledgements:

We thank Daniel P. Marrone, Stephen Muchovej, John E. Carlstrom, and Tony Mroczkowski of the SZA collaboration for sharing the results of the SZA Survey, which helped motivate the

detailed follow-up campaign of DLSCL J0916.2+2951. Support for this work was provided by NASA through Chandra Award Number GO1-12171X issued by CXO Center, which is operated by the SAO for and on behalf of NASA under contract NAS8-03060. Support for program number GO-12377 was provided by NASA through a grant from STScI, which is operated by the Association of Universities for Research in Astronomy, Inc., under NASA contract NAS5-26555.

This work made use of the following facilities: CXO (ACIS-I), HST (ACS), Keck:I (LRIS), Keck:2 (DEIMOS), Mayall (MOSAIC 1 & 1.1), Subaru (Suprime-Cam), SZA.

Chapter 3

The Dynamics of Merging Clusters: A Monte Carlo Solution Applied to the Bullet and Musket Ball

This chapter was originally published as an article with the same title in the August, 1, 2013 issue of the *Astrophysical Journal Letters* (Dawson, 2013, Volume 772, pp. 131-150).

Merging galaxy clusters have become one of the most important probes of dark matter, providing evidence for dark matter over modified gravity and even constraints on the dark matter self-interaction cross-section. To properly constrain the dark matter cross-section it is necessary to understand the dynamics of the merger, as the inferred cross-section is a function of both the velocity of the collision and the observed time since collision. While the best understanding of merging system dynamics comes from N-body simulations, these are computationally intensive and often explore only a limited volume of the merger phase space allowed by observed parameter uncertainty. Simple analytic models exist but the assumptions of these methods invalidate their results near the collision time, plus error propagation of the highly correlated merger parameters is unfeasible. To address these weaknesses I develop a Monte Carlo method to discern the properties of *dissociative mergers* and propagate the uncertainty of the measured cluster parameters in an accurate and Bayesian manner. I introduce this method, verify it against an existing hydrodynamic N-body simulation, and apply it to two known dissociative mergers: 1ES 0657-558 (Bullet Cluster) and DLSCL

J0916.2+2951 (Musket Ball Cluster). I find that this method surpasses existing analytic models — providing accurate (10% level) dynamic parameter and uncertainty estimates throughout the merger history. This coupled with minimal required *a priori* information (subcluster mass, redshift, and projected separation) and relatively fast computation (\sim 6 CPU hours) makes this method ideal for large samples of dissociative merging clusters.

3.1 Introduction

Merging galaxy clusters have become important astrophysical probes providing constraints on the dark matter (DM) self-interaction cross-section [σ_{DM} ; 19, 41, 91, 93, 100, 127], and the large-scale matter-antimatter ratio [144]. They are a suspected source of extremely energetic cosmic rays [154], and the merger event potentially affects the evolution of the cluster galaxies [e.g. 28, 74, 123]. All of the respective astrophysical conclusions drawn from merging clusters depend on the specific dynamic properties of a given merger.

For example, the subclass of dissociative mergers, in which the collisional cluster gas has become dissociated from the near collisionless galaxies and dark matter, provides four ways of constraining the dark matter self-interaction cross-section [93, 127]. The best constraints come from studying the mass-to-light ratios (M/L) of the subclusters¹, and the offset between the collisionless galaxies and dark matter (see Chapter 1 for a detailed discussion). Both constraints directly depend on the merger dynamics. First the relative collision velocity will affect the expected momentum transfer between each subcluster’s dark matter particles which will in turn affect the expected dark matter mass transfer from the smaller subcluster to the larger subcluster ultimately affecting the expected mass to light ratios of the clusters [93]. Second the expected galaxy–dark matter offset will depend on the observed time-since-collision² (TSC). Initially the offset between the galaxies and dark matter will increase with TSC (for $\sigma_{\text{DM}} > 0$) as the collisionless galaxies outrun the dark matter that experienced a drag force during the collision, then at later TSC the offset will decrease due to the gravitational attraction between the galaxies and dark matter halo. Additionally it is important to know the velocity so that dark matter candidates with velocity dependent

¹I define *subcluster* as either one of the two colliding clusters, irrespective of mass, and I define *cluster* as the whole two-subcluster system.

²I define the time of collision to be the time of the first pericentric passage.

cross-sections [e.g. 33, 160] can be constrained.

However there is no way to directly observe the dynamic merger parameters of principal interest: the three-dimensional relative velocity (v_{3D}) and separation (d_{3D}) of the subclusters as a function of time, their maximum separation (d_{\max}), the period between collisions (T), and the time-since-collision (TSC). Observations are generally limited to: the subcluster projected separation (d_{proj}), the line-of-sight (LOS) velocity of each subcluster (v_i) as inferred from their redshifts, and their mass (M_i) or projected surface mass density profile. In addition to the obvious inability to measure a change in the merger state, it is difficult to constrain the dynamic parameters of interest even in the observed state. This is due to the general inability to constrain the angle of the merger axis with respect to the plane of the sky (α), see Figure 3.1.

For the Bullet Cluster it was originally thought that estimates of the Mach number of the cluster merger through X-ray observations of the gas shock feature [e.g. 92] could be used to estimate v_{3D} , and in conjunction with measurements of the relative LOS velocities then estimate α . Similarly, the gas pressure differential across cold front features seen in some merging clusters have also been used to estimate the Mach number of the cluster merger [e.g. 157]. However, Springel & Farrar [143] showed that the Mach number only translates to an upper limit on v_{3D} , and in the case of the Bullet Cluster they showed that the Mach inferred velocity could be a factor of ~ 2 larger than the true v_{3D} . There is potential for constraining α using polarization measurements of radio relics [47], which are associated with some cluster mergers [e.g. 154] but not all [e.g. 133]. Even if for some mergers radio relics provide constraints on α , dynamic models are still needed in order to ascertain the dynamic properties of the merger throughout time.

The two most prevalent methods for ascertaining the dynamics of observed merging systems are *the timing argument* and N-body simulations. The timing argument is based on the solution to the equations of motion of two gravitating point masses, with the cosmological constraint that as $z \rightarrow \infty$ the separation of the two masses $d_{3D} \rightarrow 0$ [for an exposition of this method see 119]. The timing argument was first used by Kahn & Woltjer [80] to study the system of the Milky Way and M31, and first applied to binary cluster systems by Beers et al. [10]. It has recently been applied to several dissociative mergers, including the Bullet

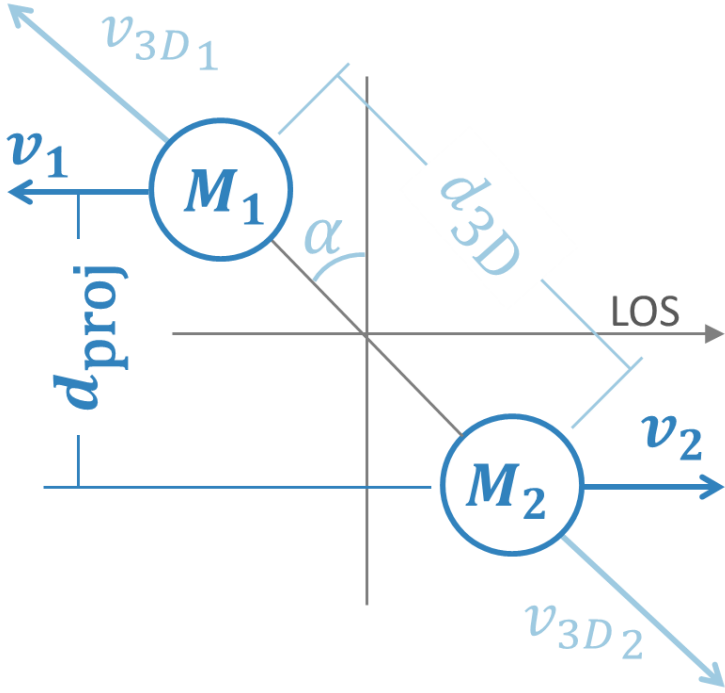


Figure 3.1: The generic two-halo merger configuration assumed in this work. Observable parameters are shown in dark blue, and include the mass of each halo (M_i), the projected separation (d_{proj}), and the line of sight (LOS) velocity components (v_i) as determined from the halo redshifts. The generally unknown parameters of the mergers are shown in light blue, and include the angle of the merger axis with respect to the plane of the sky (α), and the three-dimensional separation (d_{3D}) and velocity components (v_{3D_i}). Note that while just the outgoing scenario is shown in this figure, the method also considers the incoming scenario.

Cluster [7], Abell 520 [62], Abell 2163 [17], and Abell 1758N [16]. N-body simulations of observed dissociative mergers have been limited to the Bullet Cluster (1ES 0657-558) and have come in two variants: hydrodynamic [95, 103, 143], and self interacting dark matter (SIDM) plus collisionless galaxy particles [127].

While the timing argument method is easy to use, its inherent assumptions result in non-negligible error for dissociative systems. Most importantly the timing argument method assumes two point mass particles; this assumption begins to break down as the two subclusters overlap and results in divergent solutions as the subclusters near collision. Since most dissociative mergers are observed with the two-subcluster halos overlapping and dark matter constraints depend on the merger dynamics near collision, application of the traditional timing argument to dissociative mergers is limited and should be done with caution. Nusser [113] addressed this weakness of the traditional timing argument by substituting truncated

Navarro, Frenk, & White [108, hereafter NFW] halos and numerically solving the equations of motion. Another weakness of the timing argument is that its main constraint requires the assumption that the subcluster masses are constant since the beginning of the universe. While Angus & McGaugh [3] have noted this problem with the initial conditions of N-body simulations and proposed a solution based on estimating the mass accretion histories of the clusters [e.g. 164], their correction is incompatible with the timing argument method as this would add a second differential term to the equations of motion. Finally, the large covariance between the merger parameters plus the complexity of the equations of motion makes propagation of errors in the timing argument formalism untenable. This has resulted in a lack of certainty with timing argument results, leaving most users to run a few scenarios in an effort to roughly bound the range of possible solutions [e.g. 16].

N-body simulations provide the most accurate description of merger dynamics, however they are computationally expensive which results in their application being limited. Despite eleven currently confirmed dissociative mergers³ only the Bullet Cluster has been modeled with N-body simulations, whereas most of these have been analyzed with the timing argument method. Existing N-body simulation strategies to ascertain the dynamic properties of mergers are incapable of keeping up with the current faster than exponential rate of discovery. Even for the case of the Bullet Cluster the N-body analyses have been limited as far as mapping out the merger dynamic phase space allowed by the uncertainty of the observations, with at most 15 different scenarios being run [95]. Gómez et al. [66] have come the closest to addressing this issue in their investigation of potential dissociative mergers (A665 and AS1063) through the use of simplified scale-free numerical simulations of the mergers [see 65, for details]. However, they have still had to severely limit the phase space probed (fixing merger parameters such as the initial relative velocity and subcluster-subcluster mass ratio); thus admittedly this approach enables construction of plausible models, but not a thorough accounting of possible or likely models.

With these weaknesses in mind I present a new method⁴ for analyzing the dynamics of

³(1) Bullet Cluster [30]; (2) A520 [91]; (3) MACS J0025.4-1222 [19]; (4) A1240 [8]; (5) ZwCL 0008.8+5215 [153]; (6) A2744 [100]; (7) A2163 [116]; (8) A1758N [126]; (9) Musket Ball Cluster [41]; (10) ACT-CL J01024915 [97]; (11) MACS J0717.5+3745 [106]

⁴This method is similar to the one used by Dawson et al. [41], although with several improvements (see §3.4).

observed dissociative mergers. My primary objectives are to 1) obtain a solution valid near the collision state, 2) fully estimate the covariance matrix for the merger parameters, 3) be able to analyze a dissociative merger on the order of a day using a typical desktop computer, and 4) obtain approximately 10% accuracy; all assuming that only the most general merger observables and their uncertainty are known: mass of each subcluster, redshift of each subcluster, and projected separation of the subclusters.

In §3.2 I define a method for analyzing the dynamics of observed dissociative mergers. In §3.2.3 I verify this method with existing results from a hydrodynamic N-body simulation. In §3.3 I apply this method to the Bullet Cluster and in §3.4 I apply this method to the Musket Ball Cluster (DLSCL J0916.2+2951) and contrast its dynamics with those of the Bullet Cluster. Finally in §3.5 I summarize my findings, discuss their implications for the constraints on dark matter and suggest other science that will benefit from the introduced method. Throughout this chapter I assume $\Omega_\Lambda = 0.7$, $\Omega_m = 0.3$, and $H = 70 \text{ km s}^{-1} \text{ Mpc}^{-1}$.

3.2 Method

In order to obtain a valid solution of the system dynamics near the collision state I use a model of two spherically symmetric NFW halos, rather than point masses. I incorporate this model in a standard Monte Carlo implementation: draw randomly from the observables' probability density functions (PDF's) to generate a possible realization of the merger, use the model to calculate merger properties of interest, apply multiple priors, store these likelihood weighted results as a representative random draw of their PDF, and repeat. The final result is a multidimensional PDF for the dynamic parameters of the merger. This method agrees well with hydrodynamic simulations, §3.2.3, and satisfies the speed and accuracy objectives outlined in the Introduction.

3.2.1 Model

The general basis of the model is a collisionless two body system with the mass of each body mutually conserved throughout the merger. The model requires minimal input: the mass of each subcluster, the redshift of each subcluster, and the projected separation of the subclusters (along with associated uncertainties). It assumes conservation of energy and zero angular momentum. The model also assumes that the maximum relative velocity of the two

bodies is the free-fall velocity of the system assuming their observed mass. In the remainder of this subsection I will discuss in detail these general assumptions, their justification, and their implications.

I model the system using two spherically symmetric NFW halos truncated at r_{200} ⁵. By default the concentration of each halo is determined by the halo's mass via the mass-concentration scaling relation of Duffy et al. [46]. This is not a requirement of the model though, and measured concentrations can be used, as in the case of §3.3.1. The dynamic parameter results are relatively insensitive to the assumed concentration of the subclusters. Take for example the case of §3.2.3 with user specified concentrations of $c_1 = 1.94$ and $c_2 = 7.12$: if instead Duffy et al. [46] inferred concentrations $c_1 = 3.44$ and $c_2 = 2.75$ ($\sim 200\%$ difference for both) are used, the difference in the estimated $v_{3D}(t_{\text{col}})$ and TSC are both less than 6%.

The model assumes that the mass of each subcluster is constant and equal to the observed mass⁶. While this assumption is also used in the timing argument method, it is more reasonable for this method since the bulk of the results are calculated between the observed state and the collision state, typically lasting $\lesssim 1$ Gyr. This is about an order of magnitude shorter than the typical timescales of the timing argument method thus the new method is less susceptible to error due to neglecting growth of structure.

The model assumes that the energy of the two-halo system is conserved, and consists only of their mutual kinetic and potential energies. The kinetic energy of the system is $K(t) = 0.5\mu v_{3D}(t)^2$, where μ is the reduced mass of the system and $v_{3D}(t)$ is the relative physical velocity of the two subclusters at time t . The potential energy of the system is assumed to be purely gravitational and is derived in Appendix A.1. Since the model assumes zero impact parameter there is no rotational kinetic energy term. Mastropietro & Burkert [95] find that a moderate impact parameter of $\sim 0.1r_{200}$ has less than a 1% effect on the merger velocity, thus this assumption should have negligible effect for the case of dissociative mergers which must have had relatively small impact parameters in order to

⁵ r_{200} is defined as the radius of the spherical region within which the average density is 200 times the critical density at the respective redshift.

⁶For subcluster mass I refer to M_{200} , which is the mass of the individual subcluster enclosed within a radius of r_{200} .

dissociate the bulk of their gas.

For the relative velocity of the two subclusters I apply a flat prior from zero to the free-fall velocity of the subclusters, assuming their observed mass. This will result in an overestimate of the maximum possible relative velocity, due to the neglect of mass accretion. It is conceivable that this prior could be tightened using the maximum relative velocities observed in cosmological N-body simulations as a function of subcluster masses and redshift. Another possibility for tightening the prior would be to analytically estimate the free-fall velocity accounting for mass accretion [e.g. 3]. An advantage of the Monte Carlo approach taken with this method is that additional priors can be applied as more knowledge becomes available without the need to rerun the analysis, so I opt for a conservative default approach.

The model ignores the effects of surrounding large scale structure and simply treats the two-body system. As Nusser [113] shows, a global overdense region (10 times denser than the background) engulfing the system only affects the dynamics substantially for extreme collision velocities ($\sim 4500 \text{ km s}^{-1}$). While global overdensities may be disregarded it is not clear that the effects of nearby structures can be disregarded, e.g. as in the case three body systems. Thus this method should be applied with caution to complex cluster mergers.

The model also ignores dynamical friction. Farrar & Rosen [50] found that including dynamical friction accounted for an $\sim 10\%$ reduction in the inferred collision velocity of the Bullet Cluster in their analytic treatment. This is potentially concerning since dynamical friction is inversely proportional to the relative velocity of the merger, thus it may become even more important for mergers slower than the Bullet Cluster. However in §3.2.3 I compare the results of my method with those from a hydrodynamic N-body simulation and show that the net effect of all simplifications (including ignoring dynamical friction, tidal stripping of mass and gas mass lost during the collision) are negligible, suggesting that dynamic friction is less important than the analytic estimates of Farrar & Rosen [50] suggest.

3.2.2 Monte Carlo Analysis

In this section I discuss the details of the Monte Carlo analysis workflow. I chose to implement a Monte Carlo analysis because the high degree of correlation among the many merger dynamic parameters made traditional propagation of errors unfeasible. A Monte Carlo anal-

ysis has the added advantage of easily enabling application of different combinations of priors *ex post facto*, see e.g. §3.3.2.2.

The analysis begins by randomly drawing from the PDF's of the merger observables: mass of each subcluster (M_{200_i}), redshift of each subcluster (z_i), and projected separation of the subclusters (d_{proj}). The potential energy, V (see Appendix A.1), at the time of the collision is used to calculate the maximum relative velocity,

$$v_{3D_{\max}} = \sqrt{-\frac{2}{\mu}V(r=0)}.$$

The velocity of each subcluster relative to us is estimated from its redshift,

$$v_i = \left[\frac{(1+z_i)^2 - 1}{(1+z_i)^2 + 1} \right] c,$$

where c is the speed of light. The relative radial velocity of the subclusters is calculated from their redshifts,

$$v_{\text{rad}}(t_{\text{obs}}) = \frac{|v_2 - v_1|}{1 - \frac{v_1 v_2}{c^2}}.$$

Since the angle of the merger axis with respect to the plane of the sky, α , is unconstrained without prior knowledge of the three-dimensional relative velocity, I assume that all merger directions are equally probable. However, projection effects result in $PDF(\alpha) = \cos(\alpha)$. Due to symmetry it is only necessary to analyze the range $0 \leq \alpha \leq 90$ degrees. I draw randomly from this PDF for each realization. This enables the calculation of the three-dimensional relative velocity in the observed state,

$$v_{3D}(t_{\text{obs}}) = v_{\text{rad}}(t_{\text{obs}}) / \sin(\alpha), \quad (3.1)$$

as well as the observed three-dimensional separation of the subclusters,

$$d_{3D}(t_{\text{obs}}) = d_{\text{proj}} / \cos(\alpha). \quad (3.2)$$

If $v_{3D}(t_{\text{obs}}) > v_{3D_{\max}}$, then this realization of the merger is discarded; otherwise the relative collision velocity is calculated,

$$v_{3D}(t_{\text{col}}) = \sqrt{v_{3D}(t_{\text{obs}})^2 + \frac{2}{\mu} [V(t_{\text{obs}}) - V(t_{\text{col}})]}. \quad (3.3)$$

Similarly if $v_{3D}(t_{\text{col}}) > v_{3D_{\max}}$, then this realization is discarded.

The change in time, Δt , between two separations is given by

$$\Delta t = \int_{r_1}^{r_2} \frac{dr}{\sqrt{\frac{2}{\mu}(E - V(r))}}. \quad (3.4)$$

I define the time-since-collision (TSC) as the time it takes the subclusters to traverse from zero separation to their physical separation in the observed state, d_{3D} . Because there is a potential degeneracy in whether the subclusters are “outgoing” (approaching the apoapsis after collision) or “incoming” (on a return trajectory after colliding and reaching the apoapsis); I solve for both of these cases, TSC_0 and TSC_1 respectively. In determining TSC_1 it is useful to define the period, T , of the system. I define T to be the time between collisions,

$$T = 2 \int_0^{d_{\max}} \frac{dr}{\sqrt{\frac{2}{\mu}(E - V(r))}},$$

where d_{\max} is the distance from zero separation to the apoapsis, when $E = V$. Thus,

$$TSC_1 = T - TSC_0.$$

During the Monte Carlo analysis any realizations with TSC_0 greater than the age of the Universe at the cluster redshift are discarded. A similar flat prior is applied when calculating the statistics of TSC_1 . To this regard some insight into the likelihood of the system being in an “outgoing” or “incoming” state can be gained by calculating the fraction of realizations with TSC_1 less than the age of the Universe at the cluster redshift. Conceivably these temporal priors could be strengthened, requiring that the time to first collision (T) plus the respective TSC be less than the age of the Universe at the cluster redshift, in a fashion similar to the timing argument. However, as with the timing argument model, the model of §3.2.1 becomes less valid over time-scales approaching the age of the Universe. Thus I use the more conservative prior by default.

Since the majority of the merger time is spent at large separations, due to lower relative velocities, observations of the system are more likely near apoapsis than near the collision. Thus the probability of each realization is convolved with the prior

$$\text{PDF}(TSC_0) = 2 \frac{TSC_0}{T}. \quad (3.5)$$

There are likely selection effects which complicate this PDF, since it can be imagined that the X-ray luminosity is greatest near the time of the collision [see e.g. 128]. However this information is rarely if ever known, thus it is not included by default. In §3.3.2.2 I show how additional temporal priors, based on similar effects, may be effectively applied to the results of the analysis *ex post facto*.

The end result of this method is a 13 dimensional posterior PDF of an array of cluster merger parameters, see for example Appendix A.3. Finally to compact the results I use the biweight-statistic (generally more robust and less sensitive to abnormally tailed distributions than the median or mean) and bias-corrected percent confidence limits [9] applied to the marginalized parameter distributions of the valid realizations, see for example Table 3.2.

3.2.3 Comparison with Hydrodynamic Simulations

For the purposes of checking the physical assumptions of the model I reanalyze the Springel & Farrar [143] model of the Bullet Cluster, comparing my dynamic parameter estimates with their hydrodynamic N-body simulation based estimates. For this analysis I run just their single case through the model (i.e. I do not perform a Monte Carlo analysis). They represent the “main” and “bullet” subclusters as NFW halos with $M_{200_1} = 1.5 \times 10^{15} M_\odot$, $c_1 = 1.94$, $M_{200_2} = 1.5 \times 10^{14} M_\odot$, and $c_2 = 7.12$, respectively. They note that the gas properties of their simulation most closely match the observed Bullet Cluster gas properties for the time step corresponding to a subcluster separation of $d_{3D} = 625$ kpc and relative velocity of $v_{3D}(t_{\text{obs}}) = 2630 \text{ km s}^{-1}$. I define this as the “observed” state (dashed line in Figure 3.2) and use the model discussed in §3.2.1 to extrapolate values of the relative subcluster velocities (v_{3D}) and time-since-observed state (TSO) before and after the observed state (left and right of the dashed line in Figure 3.2, respectively). The Springel & Farrar [143] simulation results (black circles) for these parameters are read directly from their Figure 4.

I compare the model results (blue boxes) with the Springel & Farrar [143] simulation results, and assume their results as truth when calculating the percent error, see Figure 3.2. There is better than 4% agreement between v_{3D} and 14% agreement between the TSO. While the model results are biased, the bias appears stable and is roughly an order of magnitude smaller than the typical random error in the parameter estimates (see for example Table

3.2). Given the stability of the bias it is conceivable that it could be corrected in the model results. However, to have any confidence in this bias correction the model results should be compared with a range of merger scenarios, which is beyond the scope of this current work. Note that the better agreement between the velocity estimates than between the TSO estimates is to be expected since the velocity calculation (essentially Equation 3.3) comes from simply comparing the observed and another state of the merger whereas the TSO calculation (Equation 3.4) requires integration between these two states. The results of this comparative study essentially validate many of the simplifying assumptions of the model (conservation of energy, and ignoring the affects of dynamical friction, tidal stripping of dark matter and gas during the collision).

As an aside it should be noted that for this comparison I use the Springel & Farrar [143] NFW halo parameters that represent the state of the halos prior to collision. Ideally I should use the NFW parameters representative of the state of the halos at t_{obs} , however these properties were not reported in their paper. From Figure 5 of Springel & Farrar [143] some insight into the time variability of the halo parameters can be gained. Since the depth each halo’s gravitational potential at $\sim r_{200}$ does not change appreciably throughout the merger, it can be inferred that M_{200} of each halo does not change. However, the gravitational potential near the center of each halo deepens by $\sim 25\%$ during and after the collision. This can be interpreted as the concentration of each halo increasing. Thus for the comparison of my model with the Springel & Farrar [143] hydrodynamic simulation to be more appropriate I should have used halos with larger concentrations. Doing so actually brings my model results more in-line with the simulation results. If for example I increase the concentration of the “bullet” halo from 1.94 to 3 and the concentration of the “main” halo from 7.12 to 8, then the percent error for the relative velocity of the halos reduces to $\lesssim 1\%$ and the percent error for the TSO reduces to $\sim 10\%$. Thus the comparative results of Figure 3.2 should be considered conservative with respect to the variability of the halo properties throughout the merger.

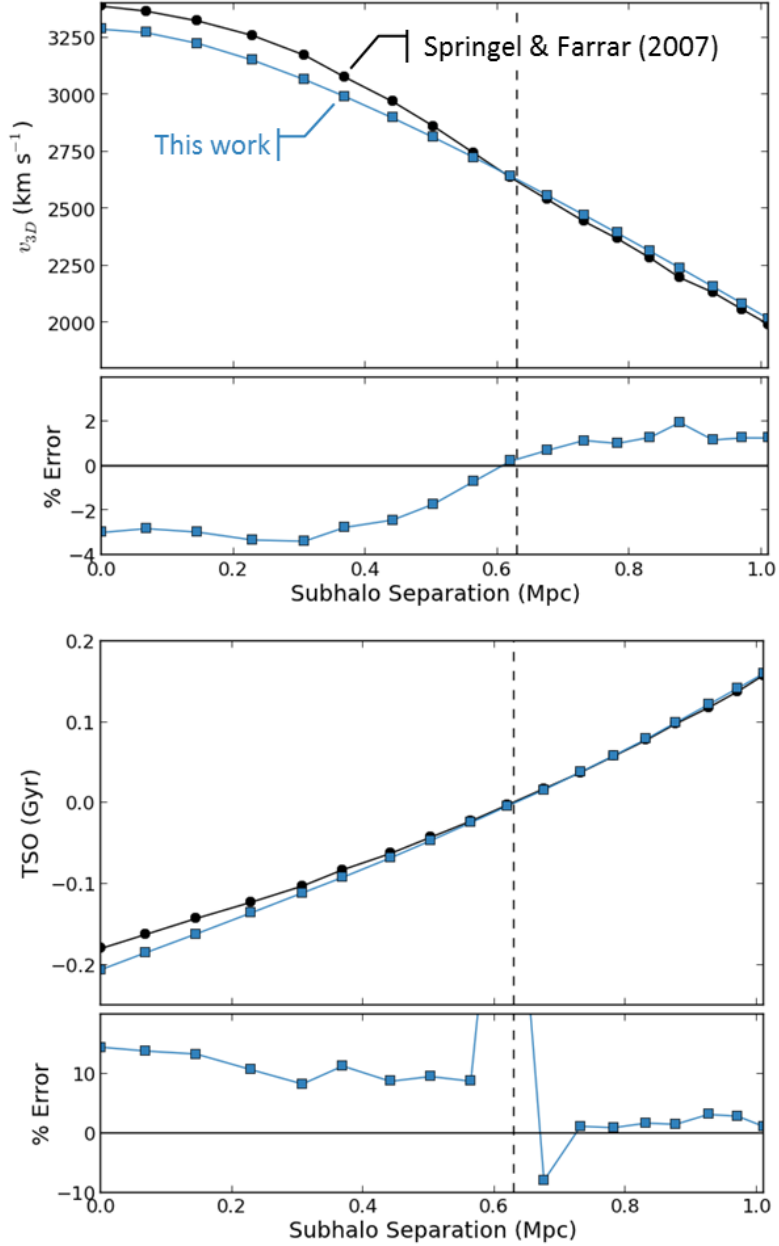


Figure 3.2: Comparison of the model results (blue boxes) with the hydrodynamic simulation results of Springel & Farrar [black circles; 143] for the Bullet Cluster. The top figure is a comparison of the velocity of the “bullet” relative to the “main” subcluster, with the subhalo separation (i.e. the three-dimensional separation of the “main” and “bullet” subclusters) as the independent variable. The bottom figure is a comparison of the time-since-observed state (TSO), where the “observed” state (dashed line) is defined by Springel & Farrar [143] as the time step in their simulation when the gas properties most closely match the observed Bullet Cluster gas properties. Times prior(post) to the observed state have negative(positive) values. The percent error in each case is calculated assuming the Springel & Farrar [143] results as truth. While the model results are biased, the bias appears stable and is roughly an order of magnitude smaller than the typical random error in the parameter estimates (see for example Table 3.2). Note that the TSO percent error calculation understandably diverges near the arbitrary choice of time equal zero. The Springel & Farrar [143] results are read directly from their Figure 4.

3.3 Bullet Cluster Dynamics

The Bullet Cluster is the prime candidate for first application of the method as it is one of the best studied dissociative mergers. It has a wealth of observational data necessary for input to the model, as discussed in §3.3.1, plus supplementary data which enables additional posterior priors, as discussed in §3.3.2.2.

3.3.1 Bullet Cluster Observed System Properties

I summarize the observed Bullet Cluster parameters used as input to my analysis in Table 3.1. The full PDF’s of these input parameters have not been published so I simply assume Gaussian distributions. I refer to the main subcluster as halo 1 and the “bullet” subcluster as halo 2. For the mass and concentration of each subcluster I use the most recently reported estimates from Springel & Farrar [143], based upon strong and weak lensing estimates [20]. However, they do not present errors for these quantities so for the mass I estimate the $1-\sigma$ errors to be 10% of the mass, since this is approximately the magnitude of the error reported by Bradač et al. [20] for $M(< 250 \text{ kpc})$. There is no published estimate for the uncertainty of the concentrations of the NFW model fits, c_i , so I simply assume the concentrations to be known quantities (as noted in §3.2.1 the results are relatively insensitive to the assumed concentrations). The redshifts of the main and “bullet” subclusters are estimated from 71 and 7 spectroscopic members, respectively [7]. The projected separation of the mass peaks is determined from strong and weak lensing measurements [20], and is essentially the same as the separation of the subclusters’ galaxy centroids. For each Monte Carlo realization individual values are drawn randomly from each of these assumed Gaussian distributions.

3.3.2 Bullet Cluster System Dynamics Results

I first analyze the Bullet Cluster with the Monte Carlo analysis method and default priors discussed in §3.2, highlighting the complexity of merger dynamics and the inappropriateness of analyzing a small sample of select merger scenarios. In §3.3.2.2 I incorporate additional constraints provided by the observed strong X-ray shock front plus boosted temperature and luminosity. I discuss this prior information and apply it ex post facto to the default prior results of §3.3.2.1.

I perform the analysis with 2,000,000 Monte Carlo realizations. Parameter estimates

Table 3.1. Bullet Cluster parameter input

Parameter	Units	μ	σ	Ref.
M_{200_1}	$10^{14} M_\odot$	15	1.5 ^a	1
c_1		7.2	... ^b	1
M_{200_2}	$10^{14} M_\odot$	1.5	0.15 ^a	1
c_2		2.0	... ^b	1
z_1		0.29560	0.00023	2
z_2		0.29826	0.00014	2
d_{proj}	kpc	720	25	3

Note. — A Gaussian distribution with mean, μ , and standard deviation, σ , is assumed for all parameters with quoted respective values. The mass, M_{200} , and concentration, c , are the defining properties of assumed spherically symmetric NFW halos.

^aEstimated to be 10%, based one the error magnitude of $M(< 250 \text{ kpc})$ reported in Bradač et al. [20].

^bNo errors were presented in the reference. A single concentration value was used for all Monte Carlo realizations.

References. — (1) Springel & Farrar 2007; (2) Barrena et al. 2002; (3) Bradač et al. 2006.

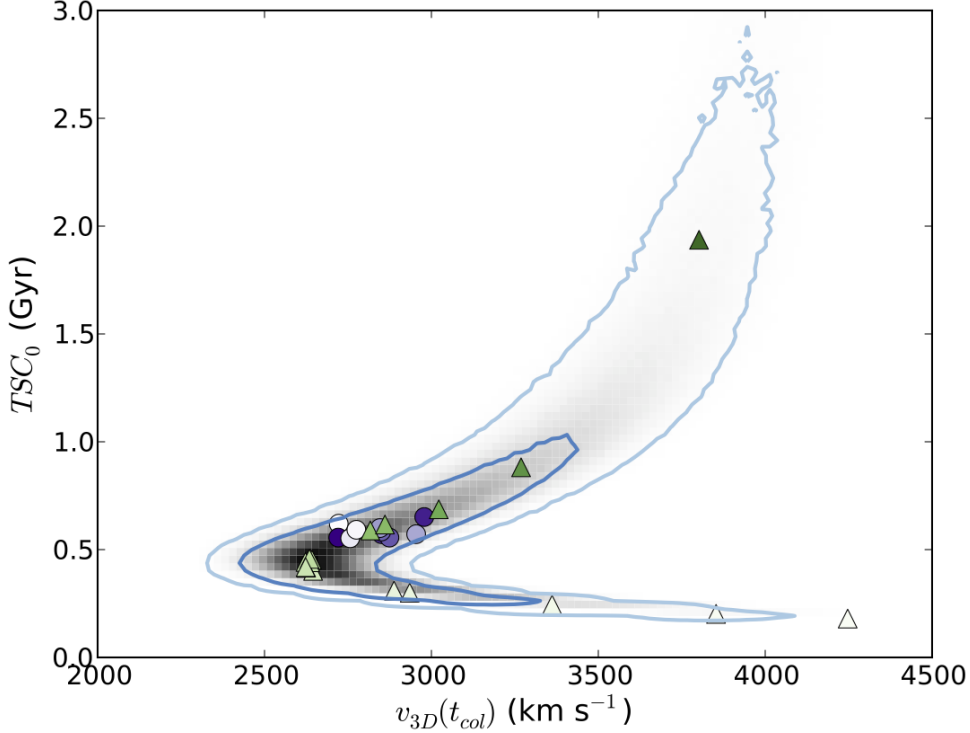


Figure 3.3: The posterior of the Bullet Cluster’s time-since-collision TSC_0 and $v_{3D}(t_{\text{col}})$ parameters is shown in grayscale with dark and light blue contours representing 68% and 95% confidence, respectively. The green-scale triangles are from a subsample of the Monte Carlo population, which jointly satisfies the requirement of being drawn from $\pm 0.01\sigma$ of the mean of each of the input parameters, i.e. the “most likely” values for the input parameters. Despite representing the most probable input parameter values there is considerable spread in the inferred output parameters, with the subsample clearly tracing the ridge of the distribution. The saturation of the triangles increases with increasing α , from 10–86 degrees. The purple-scale circles are from a subsample near the bi-weight location of $\alpha = 50 \pm 0.0002$ degrees, with the saturation of the circles increasing with increasing M_{200_1} . While the length of the distribution is predominantly caused by uncertainty in α the width is predominantly caused by uncertainty in the input parameters. Despite the Bullet Cluster being one of the best measured dissociative mergers there is still considerable and complex uncertainty in its merger parameters, predominantly due to uncertainty in α .

converge to better than a fraction of a percent with only 20,000 realizations (~ 6 CPU hours). I run a factor of a hundred more since it was computationally inexpensive and it provides a data sample to which I can apply any number of conceivable posterior PDF’s and still maintain sub-percent statistical accuracy.

3.3.2.1 Default Priors

The main results of this analysis are that: 1) there is a great degree of covariance between the geometry, velocity, and time parameters of the merger, and 2) models of the system which disregard the uncertainty of α will catastrophically fail to capture the true uncertainty in

the dynamic parameters.

The two-dimensional PDF of Figure 3.3 exemplifies the complexity of the covariance between the various merger parameters⁷. The shape of the PDF is most easily understood in terms of the parameters’ dependence on α . This dependence is illustrated by the green-scale triangles that represent a subsample of the Monte Carlo population, which jointly satisfies the requirement of being drawn from $\pm 0.13\sigma$ of the mean of each of the input parameters, i.e. the “most likely” values for the input parameters. The saturation of the triangles increases with increasing α , from 10–86 degrees, clearly showing a monotonically increasing relationship with TSC_0 (see also Figure A.6). For small α (light green triangles), Equation 3.1 states that $v_{3D}(t_{obs})$ must be large thus $v_{3D}(t_{col})$ must also be large, and since Equation 3.2 states that $d_{3D}(t_{obs})$ approaches the minimum possible observed separation, d_{proj} , the TSC_0 must approach a minimum. Conversely for large α (dark green triangles), $d_{3D}(t_{obs})$ becomes large increasing the time required to reach the observed state, and despite $v_{3D}(t_{obs})$ approaching the minimum $v_{rad}(t_{obs})$ the collision velocity must increase for the subclusters to have been able to reach the larger $d_{3D}(t_{obs})$.

The bulk of the uncertainty in the geometry, velocity and time parameters is due to the uncertainty of α . This is exemplified by the fact that the green-scale triangles in Figure 3.3 closely trace the extent of the ridge line of the two-dimensional distribution (i.e. span the bulk of the uncertainty). Conversely the “width” of the distribution is predominantly due to uncertainty in the input parameters. This is exemplified by the purple circles of Figure 3.3, which are for a near constant α yet randomly sample the M_{200} distribution. The saturation of the circles increase with increasing mass.

The inability to directly measure α , coupled with its strong degree of correlation with the other dynamic parameters, makes it the dominant source of uncertainty. While it was originally believed that the three-dimensional merger velocity as inferred from the X-ray shock feature could be coupled with the redshift determined radial velocity to measure α , Springel & Farrar [143] showed that the X-ray shock inferred velocity significantly overestimates the true three-dimensional merger velocity. So at best this information can weakly constrain

⁷Similar degrees of complex covariance exist for the other geometry, velocity and time parameters, see e.g. the results array in Appendix A.3.

α , and in the case of the Bullet Cluster the X-ray shock inferred velocity is significantly greater than the free-fall velocity, $v_{3D_{max}}$, thus it provides no additional constraining power. In §3.5.1 I discuss how the results of this method can be used in conjunction with N-body simulations to limit the computational impact of accounting for the uncertainty in α .

3.3.2.2 Added Temporal Prior

One of the advantages of this Monte Carlo method is that additional constraints are easily incorporated ex post facto. An example of such constraints in the case of the Bullet Cluster is the observed X-ray shock front and factor of 2.4 greater X-ray estimated mass to lensing estimated mass [92], due to merger related X-ray temperature and luminosity boost. Hydrodynamic simulations of merging clusters [e.g. 128, 129] suggest that such transient effects last of order the X-ray sound crossing time. Since simulations show negligible difference between the time scales of the two I chose to construct a prior based on the observed temperature boost. Randall et al. [128] find that the full-width-half-max (FWHM) duration of the temperature boost is $\sim 0.4t_{sc}$ with the entire boost duration being $\sim 1.4t_{sc}$, where t_{sc} is the sound crossing time of the more massive of the two subclusters. The peak of this boost roughly coincides with the time of the *collision*, as defined in §3.1. Given the $M_{200_1} = 15 \times 10^{14} M_\odot$ and temperature $T_X = 14 \text{ keV}$ of the “main” subcluster [92], the $t_{sc} = 1 \text{ Gyr}$. I construct a sigmoid function for the TSC prior PDF based on the observed temperature boost,

$$\text{PDF}(TSC) = \frac{1}{2} \left[1 - \tanh \left(\frac{TSC - 0.5a}{0.25b} \right) \right],$$

where a is the FWHM of the duration of the temperature boost and b is the entire boost duration. I chose a sigmoid function over a simple step function since the temperature boost predicted by Randall et al. [128] does not end abruptly. This prior is coupled with the previously discussed TSC prior (Equation 3.5).

Application of this prior significantly improves the uncertainty in TSC_0 (180% to 67%) and $v_{3D}(t_{col})$ (28% to 19%), compare Figure 3.3 with Figure 3.4. It essentially removes the possibility of a $TSC > 0.6 \text{ Gyr}$. As expected from the α dependence shown by the green triangles in Figure 3.3 this prior also reduces the likelihood of $\alpha \gtrsim 50$ degrees, which in turn affects both the location and uncertainty of d_{3D} and $v_{3D}(t_{obs})$, see Table 3.2. The remaining

Table 3.2. Bullet Cluster parameter estimates

Parameter	Units	Location ^a	Default Priors			Default + Added Temporal Priors		
			68% LCL–UCL ^b	95% LCL–UCL ^b	Location ^a	68% LCL–UCL ^b	95% LCL–UCL ^b	Location ^a
M_{200_1}	$10^{14} M_\odot$	15.0	13.5 – 16.6	12.1 – 18.1	15.2	13.6 – 16.6	12.2 – 18.1	
M_{200_2}	$10^{14} M_\odot$	1.5	1.4 – 1.6	1.2 – 1.8	1.5	1.4 – 1.7	1.2 – 1.8	
z_1		0.2956	0.2954 – 0.2958	0.2951 – 0.2961	0.2956	0.2954 – 0.2958	0.2951 – 0.2961	
z_2		0.2983	0.2981 – 0.2984	0.2980 – 0.2985	0.2983	0.2981 – 0.2984	0.2980 – 0.2985	
d_{proj}	Mpc	0.72	0.69 – 0.76	0.65 – 0.80	0.72	0.68 – 0.75	0.64 – 0.79	
α	degree	50	27 – 73	15 – 84	24	16 – 38	11 – 53	
d_{3D}	Mpc	1.1	0.8 – 2.6	0.7 – 7.1	0.8	0.7 – 0.9	0.7 – 1.2	
d_{\max}	Mpc	1.3	1.1 – 2.5	1.0 – 6.4	1.2	1.0 – 1.7	1.0 – 3.1	
$v_{3D}(t_{\text{obs}})$	km s^{-1}	820	640 – 1500	550 – 2500	1600	1100 – 2500	790 – 3200	
$v_{3D}(t_{\text{col}})$	km s^{-1}	3000	2700 – 3800	2500 – 4200	2800	2600 – 3300	2500 – 3800	
TSC_0	Gyr	0.6	0.3 – 1.1	0.2 – 3.9	0.4	0.3 – 0.5	0.2 – 0.6	
TSC_1^c	Gyr	1.2	1.0 – 2.4	0.9 – 8.2	1.3	1.0 – 2.0	0.9 – 4.6	
T	Gyr	1.8	1.5 – 3.2	1.4 – 8.1	1.6	1.4 – 2.3	1.3 – 4.8	

^aBiweight-statistic location [see e.g. 9].

^bBias-corrected lower and upper confidence limits, LCL and UCL respectively [see e.g. 9].

^cFor the case of the Default + Added Temporal Prior, none of the realizations have a valid TSC_1 , meaning that the Bullet Cluster is being observed in the “outgoing” state, as discussed in §3.3.2.2.

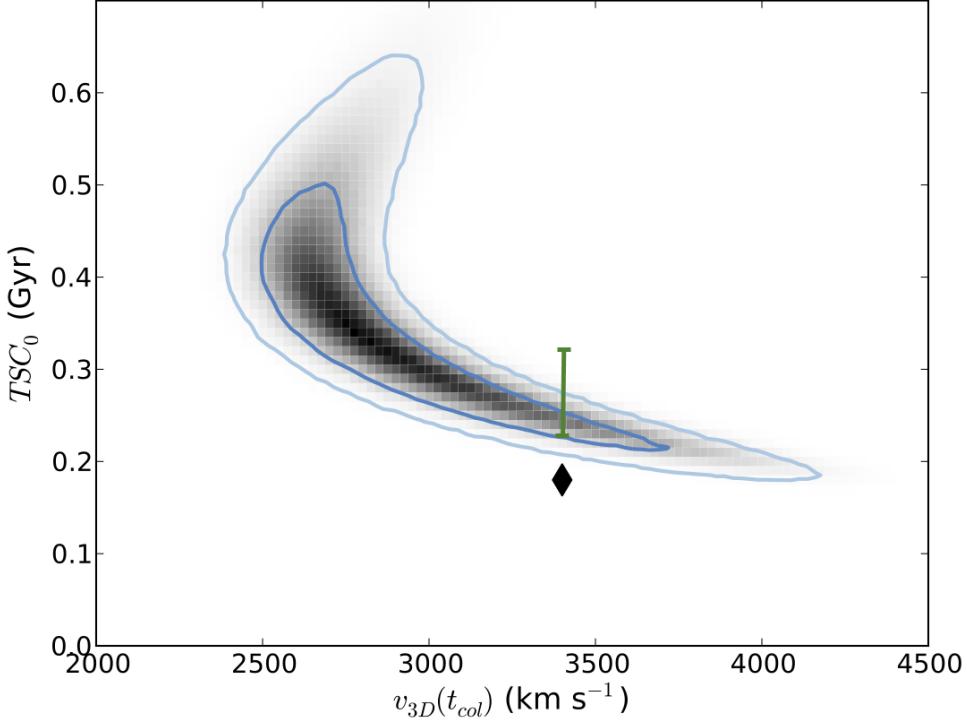


Figure 3.4: The posterior of the Bullet Cluster’s TSC_0 and $v_{3D}(t_{\text{col}})$ parameters after application of an additional temporal prior based on X-ray observations of the Bullet Cluster (grayscale). Dark and light blue contours representing 68% and 95% confidence, respectively. The added temporal prior significantly improves the constraint on the merger parameters (compare with Figure 3.3). The black diamond represents the Springel & Farrar (2007) hydrodynamic simulation result for their defined “observed state”, whose X-ray properties best match the observed X-ray properties; $d_{3D}=625$ kpc for this state. The green bar shows their result for d_{3D} between 700 to 900 kpc, which is more in line with the observed $d_{\text{proj}} = 720 \pm 25$ kpc (assuming $0 < \alpha < 35$ degrees).

parameter estimates are predominantly unaffected by the prior, with only a few having their confidence limits affected as the result of their high end low probability tails being down weighted. Additionally there is now essentially zero probability that the bullet subcluster has reached the apoapsis and is on a return trajectory, since the 95% lower confidence limit of TSC_1 is 0.9 Gyr (see Table 3.2) and the prior essentially removes the possibility of a $TSC > 0.6$ Gyr. I present the full results array, which includes the default analysis prior combined with this temperature boost prior, in Appendix A.3 and the compact parameter estimates in Table 3.2.

According to this analysis the Springel & Farrar [143] results stated in §3.2.3 seem unlikely (see the black diamond of Figure 3.4), however this is simply due to their definition of the “observed state”. They define the observed state to be when their simulated X-ray

properties most closely match the observed X-ray properties, yet the separation of the halos in this state is only $d_{3D} = 625$ kpc; this is less than the observed $d_{\text{proj}} = 720 \pm 25$ kpc [20]. If we instead consider their estimate of TSC_0 for d_{3D} between 700 to 900 kpc (corresponding to $d_{\text{proj}} = 700$ and $0 < \alpha < 35$ degrees), then $0.24 < TSC_0 < 0.33$ Gyr (see green bar of Figure 3.4). This brings their result in line with the results of this method, as expected by the agreement presented in §3.2.3. Note that the general conclusion of Springel & Farrar [143], that the shock speed greatly overestimates the actual relative speed of the subclusters, remains valid regardless of which “observed state” is used.

3.4 Musket Ball Cluster Dynamics

I also apply the method to the Musket Ball Cluster, with the objective of updating an existing analysis and comparing this system with the Bullet Cluster. A preliminary analysis of the system dynamics using a similar method [41] suggested that the Musket Ball Cluster merger is $\sim 3\text{--}5$ times further progressed than other confirmed dissociative mergers. However, that analysis treated the two merging subclusters as uniform density spheres and also failed to account for the temporal phase-space PDF (Equation 3.5). Additionally the claim that the Musket Ball Cluster is both slower and further progressed than the Bullet Cluster was based on comparing the Musket Ball’s $TSC_0 - v_{3D}(t_{\text{col}})$ PDF with that of the single point Springel & Farrar [143] estimate. As noted in §3.3.2.1 there is a large area of parameter space that the Springel & Farrar [143] result fails to represent.

Similar to my analysis of the Bullet Cluster I perform the analysis with 2,000,000 Monte Carlo realizations. Parameter estimates converge to better than a fraction of a percent with only 20,000 realizations.

3.4.1 Musket Ball Observed System Properties

I show the observed Musket Ball Cluster parameter PDF’s in Figures 3.5–3.7, each the result of analyses presented by Dawson et al. [41]. I refer to their “south” subcluster as halo 1 and “north” subcluster as halo 2. The mass PDF’s, Figure 3.5, are the result of an MCMC analysis where NFW halos were simultaneously fit to the weak lensing signal. The relative velocity distributions, Figure 3.6, are the result of a bootstrap error analysis [9] of the 38 and 35 spectroscopic members of the north and south subclusters, respectively. These redshifts

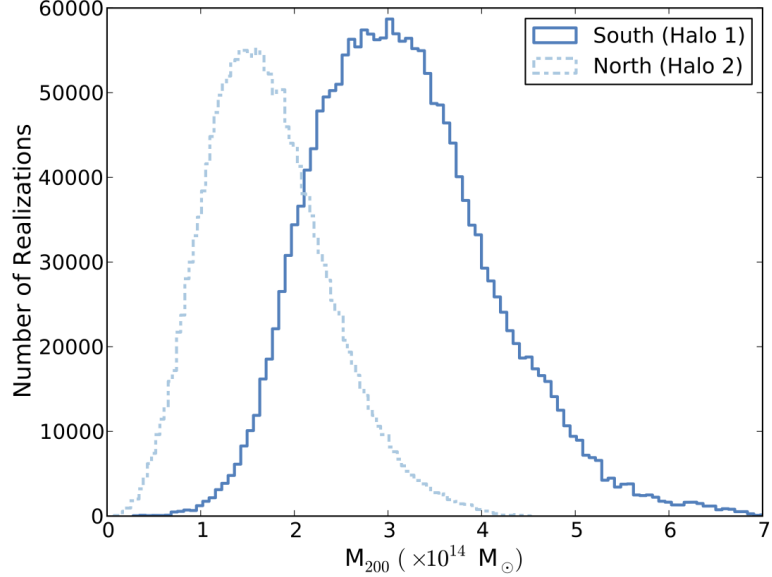


Figure 3.5: Weak lensing mass PDF’s of the Musket Ball subclusters [41].

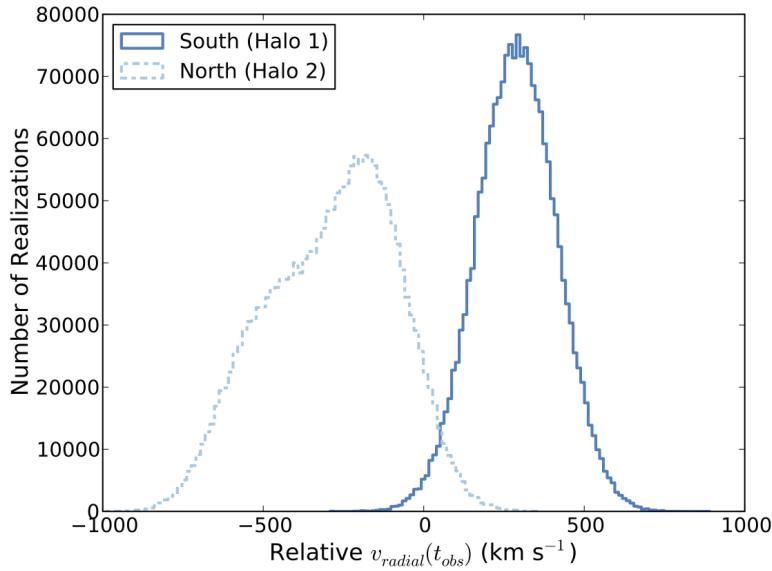


Figure 3.6: Relative radial subcluster velocity PDF’s inferred from spectroscopic redshifts the Musket Ball Cluster galaxies [41].

as well as the full Musket Ball Cluster spectroscopic catalog are presented in Table A.1 of Appendix A.2. The projected subcluster separation distribution, Figure 3.7, is the result of a bootstrap error analysis of the recursively estimated subclusters’ galaxy number density centroids [see e.g. 127, for a description of this method]. For each Monte Carlo realization individual values are drawn randomly from each of these distributions.

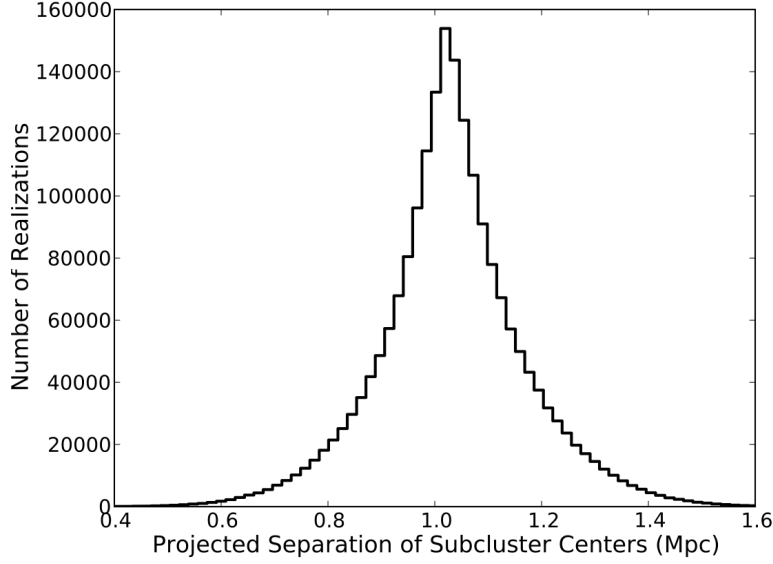


Figure 3.7: Projected separation PDF of the Musket Ball subcluster galaxy density centroids [41].

3.4.2 Musket Ball System Dynamics Results

This more complete analysis confirms that the Musket Ball Cluster merger is both significantly slower and further progressed compared to the Bullet Cluster, see Figure 3.8. To estimate a lower limit on how much further progressed I perform an additional Monte Carlo analysis for $TSC_{0\text{Musket}} - TSC_{0\text{Bullet}}$ assuming the marginalized TSC_0 distributions (see Appendices A.3 and A.4). This is a lower limit since the Musket Ball observations, unlike the Bullet Cluster observations, cannot rule out the case that its subclusters have reached the apoapsis and are on a return trajectory (61% of the realizations have TSC_1 less than the age of the Universe at $z = 0.53$). I find that the Musket Ball is at least $0.8^{+1.2}_{-0.4}$ Gyr ($3.4^{+3.8}_{-1.4}$ times) further progressed than the Bullet Cluster, see Figure 3.9. This is in line with the more approximate 3–5 times estimate of Dawson et al. [41]. The Musket Ball’s relatively large TSC_0 means that it has potential for providing tighter constraints on σ_{DM} , since the expected offset between the galaxies and dark matter will initially increase with increasing TSC_0 . However as noted in §3.1, given enough time the expected offset will decrease due the gravitational attraction between the galaxies and dark matter. Also important in determining which cluster can provide the tightest σ_{DM} constraints is the fact the expected offset increases as a function of the cluster surface mass density and collision velocity, both

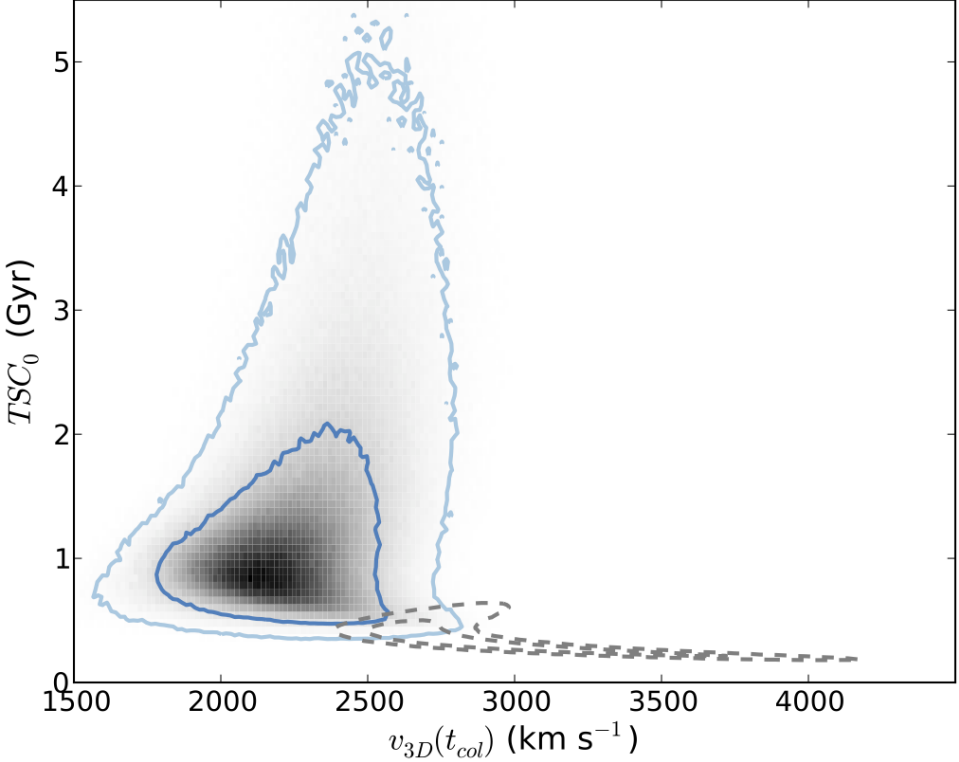


Figure 3.8: The posterior of the Musket Ball Cluster’s TSC_0 and $v_{3D}(t_{col})$ parameters is shown in grayscale with dark and light blue contours representing 68% and 95% confidence, respectively. For comparison the gray dashed contours are the Bullet Cluster’s 68% and 95% confidence intervals copied from Figure 3.4. The Musket Ball Cluster occupies a much different region of merger phase than the Bullet Cluster, having both a slower relative collision velocity and being observed in a much later stage of merger.

of which are larger in the the case of the Bullet Cluster (compare Tables 3.2 & 3.3). Without running SIDM simulations it is difficult to know at what TSC_0 the offset reaches its maximum, or which merger parameters are most important for maximizing the offset. The complete Musket Ball Cluster parameter estimates are summarized in Table 3.3 and plotted in Appendix A.4.

Note that just as a temporal prior was justified for the Bullet Cluster based on the observed shock front and increased temperature/mass estimate, I could apply a similar yet opposite prior to the Musket Ball since the temperature/mass estimate is consistent with the weak lensing inferred mass (additionally no shock front is observed). According to Randall et al. [128] if the cluster mass and inferred X-ray temperature or luminosity cluster mass are approximately the same then $TSC_0 \gtrsim 2t_{sc}$, which in the case of the Musket Ball means $TSC_0 \gtrsim 1.75$ Gyr. While this is consistent with my TSC_0 estimate for the Musket Ball,

Table 3.3. Musket Ball Cluster parameter estimates

Parameter	Units	Location ^a	68% LCL–UCL ^b	95% LCL–UCL ^b
M_{200_1}	$10^{14} M_\odot$	3.2	2.3 – 4.3	1.6 – 5.5
M_{200_2}	$10^{14} M_\odot$	1.7	1.1 – 2.4	0.6 – 3.3
z_1		0.5339	0.5333 – 0.5345	0.5326 – 0.5352
z_2		0.5316	0.5305 – 0.5324	0.5294 – 0.5331
d_{proj}	Mpc	1.0	0.9 – 1.1	0.7 – 1.3
α	degree	48	28 – 67	13 – 78
d_{3D}	Mpc	1.6	1.2 – 2.9	0.9 – 5.5
d_{max}	Mpc	2.1	1.5 – 3.8	1.1 – 7.3
$v_{\text{3D}}(t_{\text{obs}})$	km s^{-1}	670	390 – 1100	140 – 1500
$v_{\text{3D}}(t_{\text{col}})$	km s^{-1}	2300	2000 – 2500	1800 – 2800
TSC_0	Gyr	1.1	0.7 – 2.4	0.5 – 5.8
TSC_1^{c}	Gyr	3.5	2.0 – 7.2	1.4 – 12.0
T	Gyr	4.8	2.9 – 10.4	2.2 – 22.7

^aBiweight-statistic location [see e.g. 9].

^bBias-corrected lower and upper confidence limits, LCL and UCL respectively [see e.g. 9].

^c61% of the realizations with a valid TSC_0 (i.e. less than the age of the Universe at the cluster redshift) have a valid TSC_1 , meaning that it is possible that the Musket Ball Cluster is being observed in the “incoming” state.

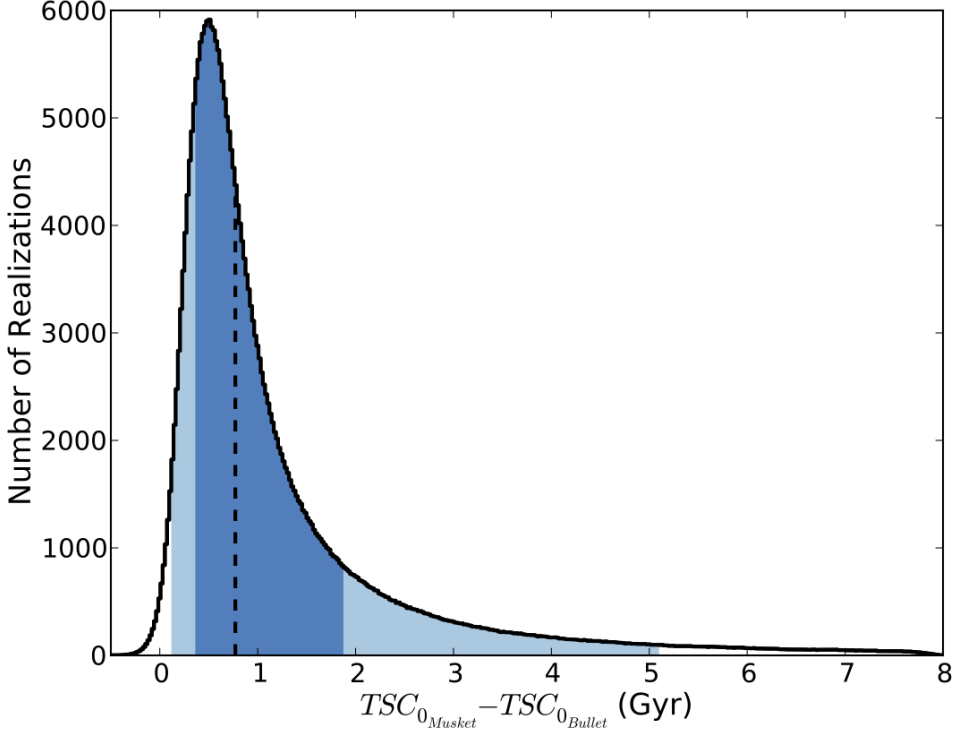


Figure 3.9: The histogram presents the $TSC_{0_{Musket}} - TSC_{0_{Bullet}}$ distribution from random draws of the respective marginalized TSC_0 distributions; showing that the Musket Ball Cluster merger is at least $0.8^{+1.2}_{-0.4}$ Gyr ($3.4^{+3.8}_{-1.4}$ times) further progressed than the Bullet Cluster merger. The black dashed line is the biweight-statistic location [10], the dark and light blue regions denote the bias-corrected 68% and 95% lower and upper confidence limits, respectively.

it is not entirely appropriate to apply this prior since the X-ray observations are relatively shallow and cannot confidently rule out a temperature and luminosity boost [41]. However it is conceivable that this line of reasoning would be applicable with deeper X-ray observations, either for the Musket Ball or similar dissociative mergers.

3.5 Summary and Discussion

I have introduced a new method for determining the dynamic properties and associated uncertainty of dissociative cluster mergers given only the most general merger observables: mass of each subcluster, redshift of each subcluster, and projected separation the subclusters. I find that this method addresses the primary weaknesses of existing methods, namely enabling accurate parameter estimation and propagation of uncertainty near the collision state with a convergent solution achieved in ~ 6 CPU hours. I have confirmed that the two NFW halo model is capable of achieving the required 10% level accuracy by direct comparison

with an N-body hydrodynamic simulation.

In applying this method to the Bullet Cluster I not only determined its merger dynamic parameters but found that the bulk of uncertainty in these parameters is due to uncertainty in α , the angle of the merger with respect to the plane of the sky. Analyses that fail to account for the uncertainty in α (all existing N-body simulations of the Bullet Cluster) will significantly underestimate the uncertainty in their results. This highlights the need to carefully select and model many possible realizations of the merger when trying to infer results from N-body simulations of a real merger (I discuss this further in §3.5.1). I have also shown how ex post facto priors can easily be applied to the results of the default priors to further constrain the inferred dynamic properties. In particular accurate measurement of the cluster gas properties can enable approximately a factor of two better constraint on the dynamic properties of the merger, principally through added constraint on the time scale of the merger.

I have also applied this method to the Musket Ball Cluster, validating the approximate results of Dawson et al. [41]. Comparing the dynamic properties of the Musket Ball with those of the Bullet I have shown that the Musket Ball represents a significantly different volume of merger phase space. The Musket Ball Cluster, being $3.4^{+3.8}_{-1.4}$ times further progressed than the Bullet Cluster, could potentially provide tighter constraints on σ_{DM} since the offset between galaxies and dark matter should initially increase with time post-merger for $\sigma_{\text{DM}} > 0$. And the larger the expected offset, the better the dark matter constraint when applying a method similar to Randall et al. [127].

3.5.1 Suggested Uses of Method

While a general method for determining the dynamics properties of merging clusters has numerous applications, several are worth noting. As noted N-body simulations of specific merging clusters are computationally expensive; in particular one SIDM simulation of a single dissociative merger requires \sim 1–10 million CPU hours (private communication, James Bullock). Thus it is currently unfeasible to simulate all confirmed dissociative mergers. This method can be used to quickly determine which mergers provide the best σ_{DM} constraining power, enabling an efficient use of limited computational resources.

Additionally it is inappropriate to simply simulate one realization of a dissociative merger due to the broad range of merger phase space allowed by uncertainty in observed parameters, as discussed in detail in §3.3.2.1. Thus multiple simulations of each merger are required to properly represent the allowed phase space. One could conceivably reduce the number of required simulations by using the results of this method to select representative merger realizations that uniformly sample the merger phase space of interest (e.g. cluster mass, $v_{3D}(t_{col})$, and TSC_0); then weight the results of each simulated realization by the integral of the corresponding local phase space PDF, as determined by this method. For example, one could estimate the uncertainty distribution of the σ_{DM} constraint inferred from SIDM simulations of the Bullet Cluster by weighting the constraint from each realization, where a realization with $v_{3D}(t_{col})=2800 \text{ km s}^{-1}$ and $TSC_0=0.4 \text{ Gyr}$ would receive greater weight than one with $v_{3D}(t_{col})=4000 \text{ km s}^{-1}$ and $TSC_0=0.2 \text{ Gyr}$, see Figure 3.4. Thus the results of this method will not only inform efficient selection of realizations to model but will reduce the number of simulations required to properly sample the posterior PDF's. Nevertheless SIDM simulations of mock clusters need to be performed to determine how much acceptable values of σ_{DM} affect the inferred merger dynamics properties.

General merger dynamic properties are also important for understanding how cluster mergers relate to other physical phenomena, such as galaxy evolution and radio relics. It is well established that galaxy clusters play an important role in the evolution of their member galaxies, but it is still unclear whether cluster mergers trigger star formation [e.g. 52, 74, 102, 118], quench it [123], or have no immediate effect [27]. Studying mergers at different TSC may resolve these seemingly conflicting results by discriminating between slow-working processes (e.g. galaxy harassment or strangulation) and fast-acting process (e.g. ram pressure stripping). Similarly, studying global merger dynamic properties may resolve the mystery of why many mergers have associated radio relics [e.g. 8, 153] yet others don't [e.g. 133].

3.5.2 Extensions to the Method

While this method has advantages over existing methods there is room for considerable improvement. For example the method could be improved through the elimination of some

of the simplifying assumptions of the model (see §3.2.1). One could attempt to incorporate subcluster mass accretion physics in a manner similar to the work of Angus & McGaugh [3] or attempt to account for the possibility of a non-zero impact parameter. To incorporate the latter one must: 1) add angular momentum terms to the equations of motion, which is entirely feasible, and 2) prescribe a reasonable impact parameter prior. Randall et al. [128] nicely outline how to determine an impact parameter PDF for halo mergers of variable mass by utilizing the PDF of the dimensionless *spin parameter*, determined from linear theory of the growth of structure [119] and simulations [22]. However, this prior should be adjusted to account for the amount of gas dissociated during the observed merger, since this amount will decrease as the impact parameter increases. Without a systematic study of various mergers in hydrodynamic simulations it is unclear exactly what adjustment an observed large dissociation of gas should infer.

Another significant extension to the model could be the inclusion of SIDM physics. As mentioned in the previous section, one of the promising uses of this method is to suggest which mergers might provide the best σ_{DM} constraining power. However one could take this a step further by including an analytic treatment of SIDM physics [e.g. 93], thereby enabling analytic estimates of σ_{DM} relevant effects for a given merger. Then this method could be used in conjunction with observed dissociative mergers to place direct constraints on σ_{DM} . Due to the increased complexity of the physics involved it would be necessary to verify this extension with SIDM N-body simulations.

Note: W. Dawson has made Python code implementing the discussed Monte Carlo method openly available at [git://github.com/MCTwo/MCMAC.git](https://github.com/MCTwo/MCMAC.git). He has also made all supporting work to this paper openly available at [git://github.com/wadawson/merging-cluster-dynamics-paper.git](https://github.com/wadawson/merging-cluster-dynamics-paper.git).

I thank my adviser David Wittman who has always encouraged my research-freewill, while at the same time providing invaluable input and correcting guidance. Our many fruitful discussions have touched every aspect of this work. I also thank the Deep Lens Survey — in particular Perry Gee — for access to the 2007 Keck LRIS spectra, as well as Perry Gee and Brian Lemaux for assistance in reduction of the 2011 Keck DEIMOS spectra. I am grateful to Jack P. Hughes for discussions on constraining the Bullet Cluster’s TSC by the observed

X-ray shock feature and boosted temperature/luminosity, and Reinout J. van Weeren for discussions on the possibilities of constraining the dynamics and geometry of mergers using radio relics. Finally I would like to thank Maruša Bradač, Ami Choi, James Jee, Phil Marshall, Annika Peter, Michael Schneider, Reinout van Weeren, and David Wittman for their substantial reviews of earlier drafts.

Support for this work was provided by NASA through Chandra Award Number GO1-12171X issued by CXO Center, which is operated by the SAO for and on behalf of NASA under contract NAS8-03060. Support for program number GO-12377 was provided by NASA through a grant from STScI, which is operated by the Association of Universities for Research in Astronomy, Inc., under NASA contract NAS5-26555. Support for this work was also provided by Graduate Research Fellowships through the University of California, Davis. I would also like to acknowledge the sultry universe who hides her secrets well.

This work made use of the following facilities: CXO (ACIS-I), HST (ACS), Keck:I (LRIS), Keck:2 (DEIMOS), Mayall (MOSAIC 1 & 1.1), Subaru (Suprime-Cam), SZA.

Chapter 4

Musket Ball Cluster: Dark Matter Implications

Portions of this chapter were originally published in the article titled *Discovery of a Dissociative Galaxy Cluster Merger with Large Physical Separation* which was published in the March 2012 issue of the Astrophysical Journal Letters (Dawson et al., 2012, Volume 747, pp. L42).

4.1 Introduction

As introduced in §1.5.2 there are four methods of constraining σ_{SIDM} with observations of dissociative mergers. In this chapter we apply two of those methods to observations of the Musket Ball Cluster. First we will consider the gas-DM offset, and second we will consider the galaxy-DM offset. As discussed in §1.5.2 these two methods are believed to be the most robust. In both cases we will depend on the WL measurements to ascertain the location of the DM. The galaxy location will be determined from optical spectroscopic and photometric observations of the galaxies, and the gas location will be determined from X-ray observations of the cluster.

We note that the exercise of comparing the galaxy-WL offset will be incomplete in this analysis, since simulations of mergers with varying σ_{SIDM} are necessary to turn any observed offset (or lack of offset) into a quantitative constraint on σ_{SIDM} (see §1.5.2.4). However we chose to present the observation portion of this analysis for two reasons. Firstly, it is

a necessary first step towards applying this constraint. Secondly, if a significant offset is observed then one could still conclude that $\sigma_{\text{SIDM}} > 0$, which would be a significant finding since this would imply that DM is self-interacting via a new force.

For both the gas-DM offset and galaxy-DM offset methods the primary measurements necessary are the location of the galaxies (§4.2), gas (§4.3), and DM (§4.4). Much of this chapter will focus on how their measurements are made with the later sections (§4.5 and §4.6) discussing the offset measurement and their implications for σ_{SIDM} .

4.1.1 Location Estimation

For the original work of Dawson et al. [41] (see Chapter 2) we estimated the weak lensing subcluster positions and errors on their positions by using the location of the peak signal in a region surrounding just the area of interest (e.g. one subcluster) and estimated the variance on the peak by measuring the peak location of each bootstrap iteration within the selected region. For this chapter, rather than using the location of the peak and variance of the peak, we have adopted an iterative centroid estimation scheme, similar to Randall et al. [127] (and often used in N-body simulations). We begin by calculating the centroid of a large aperture that encompasses one subcluster, but excludes the other. We then decrease the aperture, recenter on the previously calculated centroid, and estimate the centroid of the new aperture. This process is repeated until the aperture is decreased to a radius of ~ 200 kpc. To estimate the uncertainty on the location we perform this process on each iteration of a random bootstrap sample map, resulting in an array of centroid values. The uncertainty on the location is then inferred from the variance of this array of centroid values.

4.2 Galaxy Location

Galaxies are expected to populate dark matter subhalos [e.g. 168] and from dark matter simulations these subhalos are found to be the building blocks of clusters. Thus stars and galaxies are believed to be tracers of the underlying dark matter distribution. Evidence for this is found across all cosmological mass scales from dwarf spheroidals [e.g., 162], to galaxies [e.g., 25, 26], groups [e.g., 59], clusters [e.g., 36, 161], and large scale structures [e.g., 45]. So the location of galaxies is expected to coincide with the location of the DM in Λ CDM, to within some amount of intrinsic scatter. It is precisely this phenomenon that

we wish to challenge with observations of merging galaxy clusters, since for some non-zero σ_{SIDM} the location of the galaxy population is not expected to coincide precisely with the underlying DM distribution. As far as the location of the galaxy population (i.e. its center) is concerned there are three main challenges. First, there are many ambiguous definitions of the galaxy population location and these definitions often result in different estimates, sometimes even outside the uncertainty of each measurement [59]. Second, due to inherent observational limitations in determining galaxy positions and velocities it can be difficult to determine which galaxies are members of a given DM halo (and expected tracers of that DM halo). Third, even if galaxies are a fair sample of the underlying DM halo there are often only a few hundred members to trace the distribution of a given DM halo. Thus a certain amount of intrinsic scatter between the location of the galaxy population and the underlying DM distribution is to be expected simply due to Poisson noise. This is in addition to the intrinsic scatter that is due to galaxies being dynamic tracers of an ever evolving DM halo.

4.2.1 Definition of Galaxy Location

There are many different definitions of the location of the galaxy population. One that is commonly used is simply defining the location to be at the position of the brightest cluster galaxy [BCG; e.g. 63, 69, 84]. This method is often straightforward and for relaxed systems seems to agree well with other cluster location measures such as the X-ray location [59, 84, 135, 139]. In relaxed cool-core clusters the location of the BCG is found to agree with the location of the gas to within ≤ 15 kpc, however in non-cool core and potentially disturbed clusters the locations can be offset by ~ 100 kpc [135]. It is unclear in the case of the Sanderson et al. [135] non-cool core clusters which if either location is a better tracer of the DM location. The disadvantage of the BCG location method is that not all clusters have a dominant BCG ($\sim 1\text{--}2$ magnitudes brighter than the next brightest cluster galaxy). This is the case with the Musket Ball Cluster. In such cases the BCG is found to provide an unreliable location [see e.g. 59]

An obvious alternative to choosing a single galaxy to represent the central location of the population is to use the whole or a subsample of the galaxy population to estimate a central location. This is often done by estimating the weighted galaxy centroid [e.g. 12, 23, 59, 77],

$$\vec{x}_{\text{centroid}} = \frac{\sum_{i=1}^N w_i \vec{x}_i}{\sum_{i=1}^N w_i}, \quad (4.1)$$

where $\vec{x}_{\text{centroid}}$ is the calculated centroid coordinates (right ascension and declination in the case of observations) for a population of N galaxies with \vec{x}_i being the coordinate of galaxy i and w_i the weight assigned to that galaxy. In the case of a simple galaxy number density centroid $w_i=1$. It is common to weight galaxies by their luminosity or stellar mass. George et al. [59] find that for groups of galaxies, centroid based location estimates typically have larger uncertainties (~ 50 kpc) and appear to be offset more from the underlying DM distribution than the BCG (or in their case brightest group galaxy, BGG) location estimates. However, it is important to note that this work was performed on groups of galaxies (typically ~ 1 order of magnitude less massive and with ~ 1 order of magnitude fewer galaxies than galaxy clusters). Since the the centroid measurement error will scale with the number of member galaxies like $N^{-1/2}$, this will result in a noisier estimate in the case of galaxy groups. In support of this reasoning, Jee et al. [77] found that clusters in their sample with high lensing signal (i.e. more massive) had galaxy centroids that “agree well with the mass peaks”. However in the same study, they find that in clusters where the lensing signal is weak offsets can be $>20''$ between the mass and galaxies. The George et al. [59] and Jee et al. [77] results suggest that the systematic offset of the galaxy centroid estimate can be a strong function of the mass of the group or cluster. Finally smoothing based methods are an alternative population based location estimate. Typically in these methods the projected distribution of galaxy members are smoothed by a signal matched smoothing kernel and then the peak of this smoothed distribution is used as the location [see e.g. 67, 99, 127].

Because the Musket Ball Cluster does not have a dominant BCG in either subcluster we will adopt the centroid location estimate method. This will also allow for a consistent location estimate scheme across the multiple components of the merger, since it is easy to apply to the gas and WL measurements.

4.2.2 Cluster Membership

Another major challenge in determining the galaxy population location is separating the sample of galaxies that are gravitationally bound to a DM halo from foreground and background galaxy samples. Both the contamination of the cluster sample by fore/background galaxies, and the dilution of the cluster sample by improperly assigning cluster members to the fore/background galaxy sample will act to decrease the signal-to-noise of the galaxy centroid measurements. In the case of isolated clusters these effects should not induce a directional bias in the centroid measurement, however in the case of merging clusters it is possible to induce such a bias. In a dissociative merger the two subclusters are often in close proximity to one another, both in projected space (often within each others' virial radii) and in redshift space (often within each others' velocity dispersion). Thus the galaxy centroid estimate of one subcluster will be biased away from its true galaxy centroid towards the other subcluster. This may cancel to some degree with a similar directional bias in the WL estimate of the DM location (see §4.4) although studies of these relative biases have not been performed.

The challenge in determining cluster galaxy membership lies with the inherently limited observational information that one can obtain of galaxies. While it is relatively easy to constrain the projected position of individual galaxies to sub-arcsecond precision, it is much more difficult to constrain the position of the galaxies along the line-of-sight. The best measurements in this regard are spectroscopic redshifts of the galaxies, which can often constrain the line-of-sight velocities to a few km s^{-1} [in the case of a 1200 line mm^{-1} grating with resulting resolution of $\sim 1 \text{\AA}$; see e.g. 40]. However, spectroscopic surveys are observationally intensive often requiring a large amount of time (of order nights) on large telescopes ($\gtrsim 5 \text{ m}$)¹. Thus, many astronomers have developed and used membership identification methods that only require photometric galaxy surveys since these are capable of surveying many more galaxies in a much shorter amount of time even on smaller telescopes [e.g. the DLS, 166].

Even in the idealized case of having spectroscopic redshift information for all galaxies, two

¹Take for example the completeness of the spectroscopic survey carried out on the Musket Ball Cluster (see Figure 4.1) over 1.5 nights using the DEIMOS multi-object spectrograph on the Keck 10 m telescope.

major problems remain when estimating galaxy cluster membership in dissociative mergers. The first challenge is the “finger of god effect”. The typical velocity dispersion of cluster galaxies is $\sim 1000 \text{ km s}^{-1}$, and since a velocity difference (Δv) is related to a redshift difference (Δz) by,

$$\Delta z = \frac{\Delta v(1 + \bar{z})}{c},$$

where \bar{z} is the average of the two redshifts and c is the speed of light, the member galaxies of a cluster will often have $\Delta z \sim 0.015$ (for a cluster at $z=0.5$). This corresponds to a Hubble flow separation of $\sim 30 \text{ Mpc}$, which is roughly an order of magnitude larger than the cluster size. Thus it is nearly impossible to distinguish between cluster galaxies and projected fore/background galaxies within $\sim \pm 30 \text{ Mpc}$ of the cluster redshift. Fortunately clusters are $\sim 20\text{-}70$ times more dense than other cosmic structures [e.g. filaments, walls and voids; 4], thus this should not be a dominant source of noise. However, it becomes more important as the radius from the cluster center increases. Potentially more problematic is the second challenge to determining cluster membership which is specific to dissociative mergers. This challenge is that the typical relative merger velocity of the two subclusters in a dissociative merger is of order the velocity dispersion of each subcluster. Thus it is difficult to disengage the members of each subcluster. While similar to the “finger of god effect” this effect is potentially more serious since the central densities of each subcluster are of the same order of magnitude; for mergers just after first pass through this will be more of an issue than further progressed mergers with larger projected separations between the two subclusters. As previously mentioned this effect can potentially lead to a directional bias in the galaxy centroid estimate.

In the less ideal scenario where limited spectroscopic information is available we must attempt to determine cluster membership with only photometric data. In cases where multi-band ($\gtrsim 4$) observations have been carried out, photometric redshift estimates can be made for most of the galaxies detected with moderate signal-to-noise (~ 20). However, photometric redshift uncertainties ($\sigma_{z-\text{phot}} \sim 0.07(1+z_{\text{phot}})$) are typically many orders of magnitude larger than spectroscopic redshift uncertainties and a few orders of magnitude larger than the typical redshift velocity dispersion of a cluster. Thus, even if a galaxy has the exact same photometric redshift as the cluster there is still considerable uncertainty in whether that

galaxy is a member of the cluster. In cases of extreme photometric coverage (e.g. the COSMOS survey with 30-bands from ultraviolet to infrared) it is possible to identify 92% of cluster members (down to the limiting magnitude) with 84% purity [60]. More common is the case that there is not enough photometric coverage of a system to obtain reliable photometric redshifts and astronomers have used prior information about the properties of galaxies (e.g. luminosity, color, and stellar mass) in cluster environments to improve membership identification [see 59, for a review].

4.2.3 Galaxy Location Poisson Noise

The third challenge in estimating the galaxy population location is that there are often only a few hundred galaxies that trace a given DM halo's potential. Thus a certain amount of intrinsic scatter between the location of the galaxy population and the underlying DM distribution is to be expected simply due to Poisson noise. This source of galaxy location noise is often at direct odds with the noise from galaxy cluster membership. As one attempts to increase the number of cluster members (i.e. completeness) used in the centroid calculation to reduce the Poisson noise, they often must sacrifice purity (fraction of true cluster members to the assumed number of cluster members) which increases the noise due to cluster membership error. For example, the systematic error due to contamination can be decreased by placing strict membership requirements, e.g. only using galaxies that have spectroscopic redshifts within some small factor (e.g. 3) of the cluster velocity dispersion. However this will reduce the number of galaxies that are used to estimate the centroid and the Poisson noise will increase. At the outset there is not a clear what the optimal choice of membership selection criteria should be to minimize the joint membership noise and Poisson noise, however it is conceivable that this could be empirically optimized for a given dataset since the joint uncertainty can be determined ex post facto.

4.2.4 Estimating the Musket Ball Cluster's Galaxy Location

In this subsection we present the data used to estimate the Musket Ball Cluster's galaxy location. To determine the galaxy membership of the Musket Ball Cluster we consider two methods: a fully probabilistic method (Appendix B) and an empirically based method (§4.2.4.2). While there is potential for the fully probabilistic method by incorporating in-

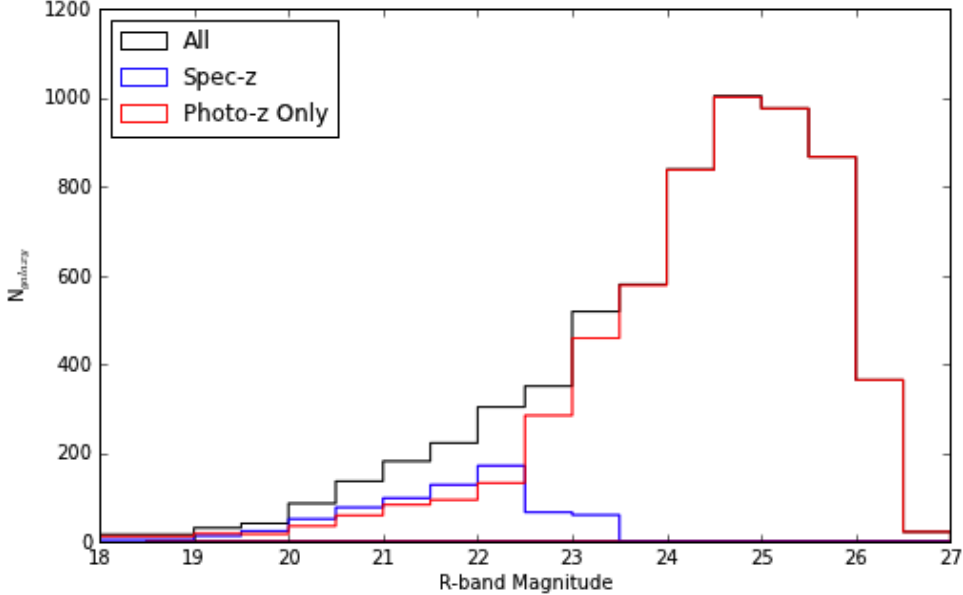


Figure 4.1: The Musket Ball Cluster spectroscopic (blue) and photometric (red) redshift galaxy magnitude distribution in the $\sim 15' \times 15'$ spectroscopic survey area. While the DLS photometric survey is complete to $R \sim 26$ photometric redshifts are not well verified fainter than $R \sim 24$.

formation about the field galaxy distribution we find that in its current state it does not provide as reliable results as the empirical method. Using the empirically based method to determine cluster membership we estimate the galaxy centroid of each subcluster.

4.2.4.1 Musket Ball Cluster Galaxy Location Data

Most of the available data to constrain the galaxy locations of the Musket Ball Cluster is presented in detail in Chapters 2 and 3, however we review some of the important information here. Because the Musket Ball Cluster is within the DLS [166] it has 4-broad-band photometry ($BVRz$) to limiting magnitudes of ~ 26 (see e.g. Figure 4.1). Additionally we observed the cluster in three medium-width optical bands (g, h , and i from the BATC filter set), bracketing the redshifted 4000 Å feature. This coverage has enabled photometric redshifts to be estimated for most of the galaxies in the cluster field with $R \lesssim 26$, however photometric errors increase for fainter galaxies and this in turn increases the photometric redshift uncertainty. For the DLS $\sigma_{z-\text{phot}} \approx 0.07(1+z_{\text{phot}})$ for galaxies with $R \leq 24$; photometric redshifts become not well verified fainter than $R \sim 24$ [137]. Thus in all our analyses of the Musket Ball Cluster's galaxy locations we only use galaxies with $R \leq 24$.

In addition to the deep photometric data we have carried out an extensive spectroscopic

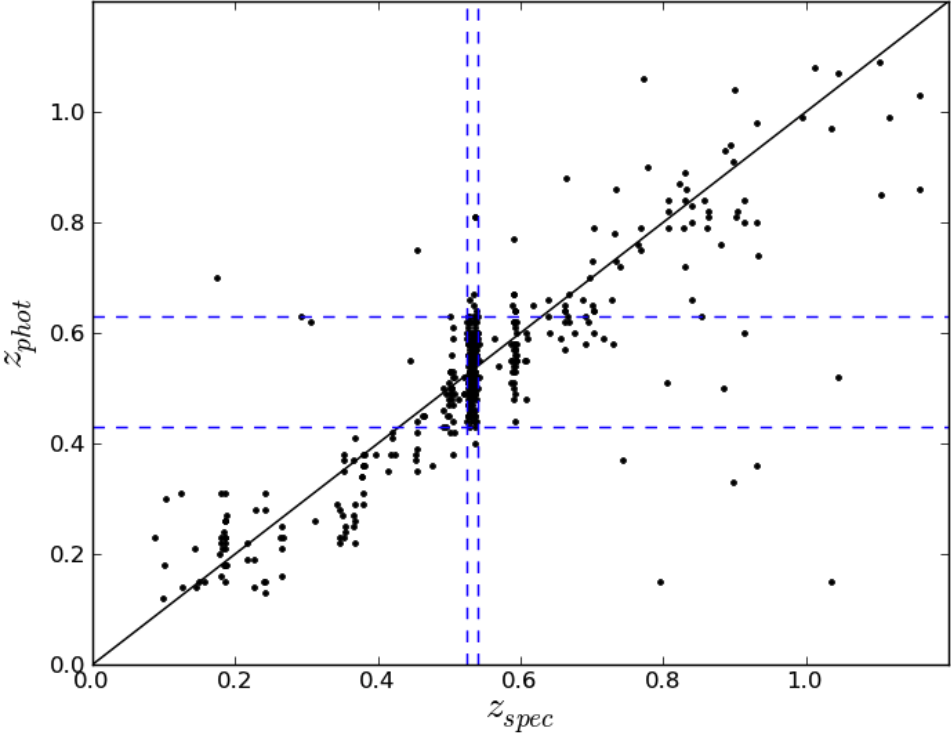


Figure 4.2: Spectroscopic redshifts versus photometric redshift estimates for the galaxies observed in the Musket Ball Cluster $R < 23.5$ magnitude limited survey (discussed in Chapter 2 and §A.2). The horizontal dashed blue lines highlight the $0.43 \leq z_{\text{phot}} \leq 0.63$ range; 63% of the surveyed galaxies within this range are cluster members. The vertical dashed blue lines highlight the $0.525 \leq z_{\text{spec}} \leq 0.54$, approximately plus or minus three times the cluster velocity dispersion at a redshift of 0.53.

survey of the Musket Ball Cluster (see §2.3 and §A.2). We have obtained a sample of 738 spectroscopically confirmed galaxy redshifts within an $\sim 18' \times 18'$ area centered on the Musket Ball Cluster (139.05 deg, +29.85 deg). This survey covers a significant fraction of the galaxies in the area brighter than $R = 23$, see Figure 4.1. This spectroscopic sample has also provided important information on the accuracy of the photometric redshifts, see Figure 4.2, in particular their accuracy of determining cluster galaxy membership.

4.2.4.2 Empirically Based Membership Determination

This method of membership determination is empirically based and leverages the galaxies that have overlapping spectroscopic and photometric coverage to inform the selection of cluster members that only have photometric redshifts. If a galaxy has a spectroscopic redshift within the $3\sigma_{\text{vdisp}}$ range of the cluster redshift ($0.525 < z_{\text{spec}} < 0.54$ for the Musket

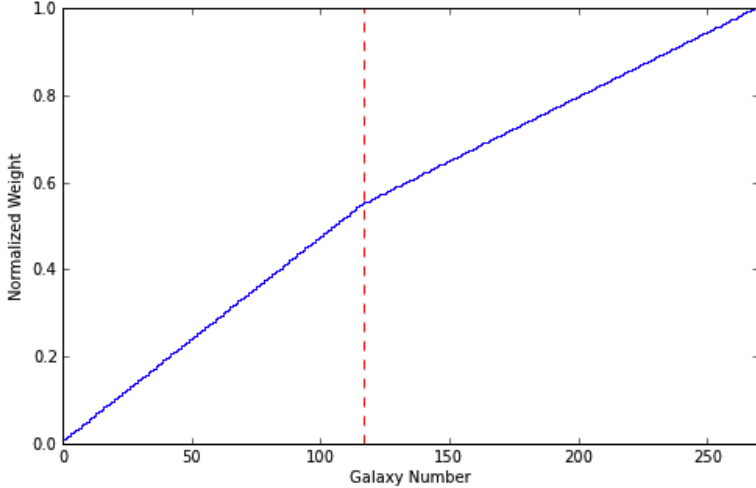


Figure 4.3: Empirically based cluster membership weighting scheme cumulative normalized weight distribution (blue step curve) for galaxies being in the Musket Ball Cluster. Galaxies that are spectroscopically confirmed cluster members ($0.525 \leq z_{\text{spec}} \leq 0.54$) are given a weight of 1 and are left of the dashed red line in this sorted sample. Galaxies that are from the photometric redshift only sample and are within the range $0.43 \leq z_{\text{phot}} \leq 0.63$ are given a weight of 0.63 and fall to the right of the red dashed line. Similar, but an alternative, to Figure B.1 this distribution is used to perform a weighted random draw of cluster galaxies for the galaxy centroid bootstrap analysis.

Ball Cluster) it is given a weight of 1². If galaxies only have a photometric redshift and that happens to be within the range $0.43 \leq z_{\text{phot}} \leq 0.63$ (approximately the Musket Ball Cluster redshift $\pm \sigma_{z-\text{phot}}$) they are given a weight of 0.63. All remaining galaxies are given a weight of 0. The cumulative normalized weight distribution function for this weighting scheme is shown in Figure 4.3.

The motivation behind the photometric redshift weight of 0.63 comes from our magnitude limited redshift survey³ of the Musket Ball Cluster. We obtained 355 high quality spectra of galaxies with $0.43 \leq z_{\text{phot}} \leq 0.63$ and 210 of these have spectroscopic redshifts between $0.525 < z_{\text{spec}} < 0.54$, see for example Figure 4.2. This translates to a purity of 63%. Note that this photometric redshift range should result in a cluster membership completeness of 95%.

² Note that this ignores the “finger of god effect”, although it is reasonable to assume that the number of cluster galaxies should dominate the number of fore/background galaxies within ± 30 Mpc of the cluster redshift this effect should not dominate the centroid uncertainty.

³The survey was magnitude limited in regards to the fact that we targeted any galaxy with $R < 23.5$, if galaxies had a $0.43 \leq z_{\text{phot}} \leq 0.63$ their likelihood of being targeted was twice that of other galaxies. This should not bias the conclusions of this section since we are limiting ourselves to considering just the range $0.43 \leq z_{\text{phot}} \leq 0.63$.

4.2.4.3 Galaxy Location Results

We use the empirical weighting scheme of §4.2.4.2 to create an updated version of the purely photometric redshift based galaxy number density map of Figure 2.2. The new galaxy number density map (Figure 4.4) gives a weight of 1 to all (117) galaxies with spectroscopic redshift within three times the velocity dispersion of each subcluster, and a weight of 0.63 to all (270) galaxies without a spectroscopic redshift but with $z_{\text{phot}} = 0.53 \pm 0.1$. While very similar to Figure 2.2, the peak in the northern subcluster is now slightly more prominent.

To estimate the location of the galaxy centroids in the north and south subclusters we use the iterative centroid procedure outlined in §4.1.1, the centroid formula of Equation 4.1 and the weights discussed in §4.2.4.2. To estimate the confidence limits on each subcluster's centroid we generate 10,000 bootstrap realizations of the galaxy sample using the cumulative weight distribution of Figure 4.3 when randomly drawing galaxies with replacement⁴. For each of these bootstrap realizations we apply the same iterative centroid procedure of §4.1.1, which generates a 10,000 sample distribution of the centroid right ascension and declination. From these bootstrap centroid distributions we calculate bias-corrected percent confidence limits [9] of the marginalized parameter distributions. We find that the south subcluster has a galaxy centroid of $09^{\text{h}}16^{\text{m}}16.0^{\text{s}} \pm 3.9^{\text{s}}$, $29^{\circ}49'14.7'' \pm 3.3''$ and the north subcluster has a galaxy centroid of $09^{\text{h}}16^{\text{m}}11.3^{\text{s}} \pm 15.9^{\text{s}}$, $29^{\circ}51'59.1'' \pm 5.3''$. These centroids and confidence limits are overplotted as dashed green ellipses on the galaxy number density map (Figure 4.4).

Finally it is worth noting that we have disregarded the centroid error associated with subcluster to subcluster galaxy membership contamination (see §4.2.2). This is a potentially important source of error and could cause a bias in the centroid estimates of each subcluster towards the direction of the other subcluster. To the best of our knowledge no-one has performed studies investigating this particular bias. As such, accounting for and correcting such a bias in the Musket Ball Cluster (and other dissociative mergers) will require a significant amount of investigation and is beyond the scope of this current dissertation. One could consider something like the multicomponent joint fitting method of Walker & Peñarrubia

⁴Note that because we weight the random draw we do not use the galaxy weights when calculating the centroid.

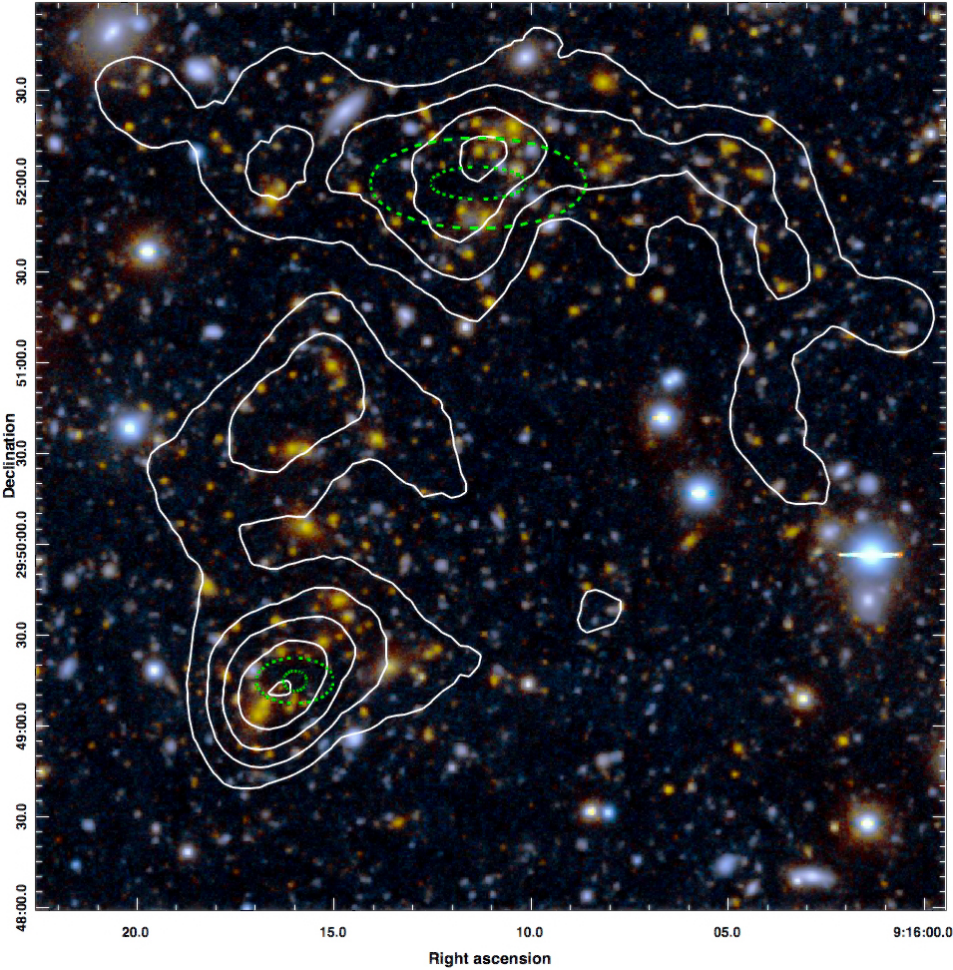


Figure 4.4: DLS composite *BVR* color image of the Musket Ball Cluster showing the galaxies of the two subclusters (predominately orange). This figure is similar to Figure 2.2, however the white contours representing the number density of galaxies now include both spectroscopic and photometric redshift information. All (117) galaxies with spectroscopic redshift and within three times the velocity dispersion of each subcluster were given a weight of 1. All (270) galaxies without a spectroscopic redshift but with $z_{\text{phot}} = 0.53 \pm 0.1$ (the cluster redshift $\pm \sigma_{z_{\text{phot}}}$) were given a weight of 0.63. The photometric redshift sample weight is based on the empirically determined cluster membership purity of this sample, as determined from our magnitude limited spectroscopic survey of the cluster. The contours begin at ~ 200 galaxies Mpc^{-2} with increments of ~ 50 galaxies Mpc^{-2} . The dashed green ellipses show the approximate galaxy centroid 68% and 95% confidence limits for each subcluster.

[163].

4.3 Gas Location

When estimating the central gas concentration’s centroid (black circles of Figure 4.5), all detected point sources (small green circles with red dashes of Figure 4.5) are excluded. Additionally the diffuse southern gas concentration is excluded (large green rectangular box of Figure 4.5). The remaining X-ray photons in the green semicircle are then used to estimate the gas centroid of the central concentration, using the *dmstat* function of the Chandra Interactive Analysis of Observations (CIAO) software package. We note that adaptive smoothing can introduce some artifacts to the image, however we find excellent agreement between the centroid of the smoothed image (black ‘x’ in Figure 4.5) and the centroid of the unsmoothed image (black circles of Figure 4.5) suggesting that the smoothed map provides a reasonable representation of the gas.

We find that the central gas concentration centroid ($09^{\text{h}}16^{\text{m}}13^{\text{s}} \pm 8^{\text{s}}$, $29^{\circ}50'55'' \pm 9''$) is offset $5.0''$ from the peak of the gas distribution ($09^{\text{h}}16^{\text{m}}15^{\text{s}} \pm 5.5^{\text{s}}$, $29^{\circ}50'59'' \pm 5.0''$). However both are significantly offset between the northern and southern galaxy and WL concentrations.

4.4 Weak Lensing Location

As discussed in Chapter 1 the best means of determining the location of the DM is with gravitational lensing since it is capable of mapping the total projected mass, which is predominately DM. Generically the major sources of error when mapping the location of DM with WL are galaxy shape measurement error, intrinsic ellipticity of galaxies, projected line-of-sight massive structures, and discrimination of foreground and cluster galaxies from the lensed source population of galaxies. These sources of error are discussed at great length elsewhere [see e.g. 44, 101] and for the specific case of the Musket Ball Cluster in Chapter 2. However there are a number of sources of error unique to dissociative mergers worth note here. First the DM mass of the one subcluster will cause a directional bias in the WL estimate of the DM location of the other subcluster away from the true DM location towards the first subcluster. Similarly the dissociated gas will cause a directional bias of the WL estimated DM location of one subcluster towards the center of the merger where the bulk

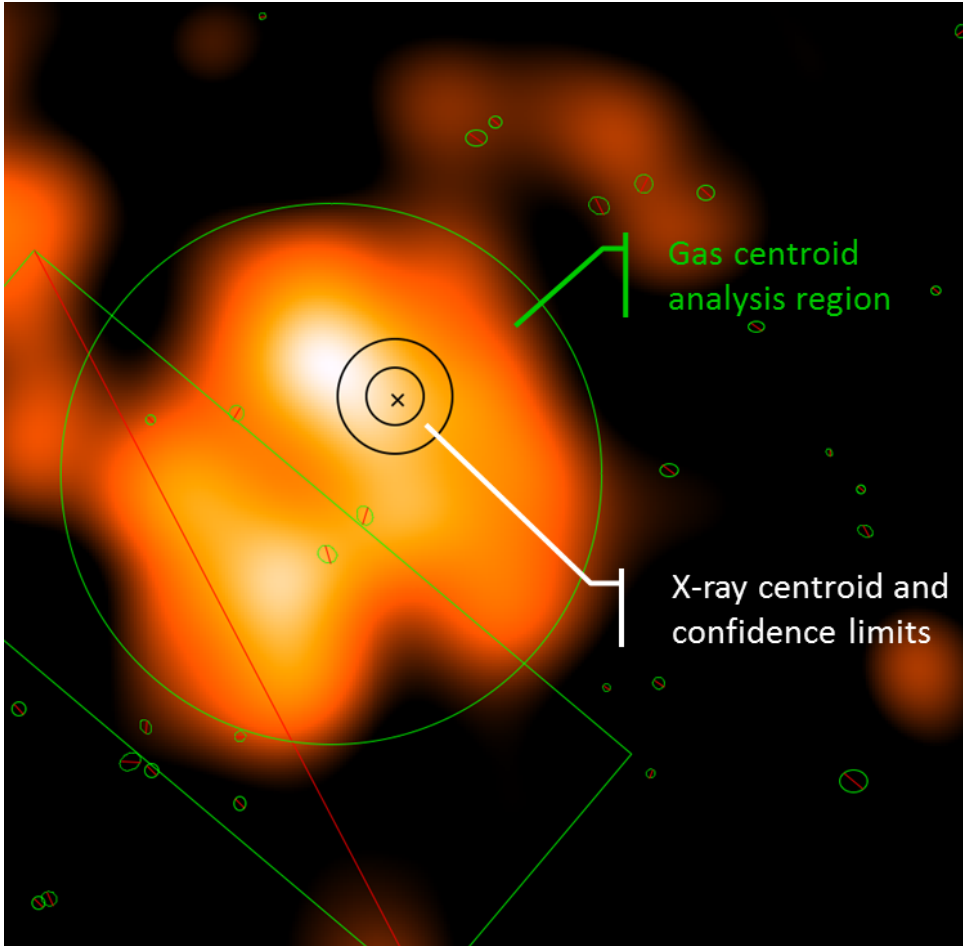


Figure 4.5: Chandra ACIS-I 40 ks adaptively smoothed X-ray image of DLSCL J0916.2+2951 (the same as Figure 2.7). The green circles and boxes are the SAOImageDS9 inclusion and exclusion regions used in conjunction with the Chandra Interactive Analysis of Observations (CIAO) software package. The unsmoothed central gas centroid 68% and 95% confidence intervals are represented by the black circles. The gas centroid is shifted towards the southwest away from the peak by the extended gas distribution in that direction. The smoothed central gas centroid is represented by the black ‘x’. The image field-of-view is the same as Figure 2.1.

of the gas resides. Both of these directional biases will mimic the expected effect of SIDM. In this section we will review how we account for the generic WL errors and go into detail on how we estimate the directional biases to the DM centroid location.

4.4.1 Generic Weak Lensing Errors

Details of the galaxy shape measurement for the Musket Ball Cluster are discussed in Chapter 2. We account for the effects of shape measurement and intrinsic ellipticity errors on the WL location in much the same way as we estimate the signal-to-noise of our WL mass maps as a whole (see §2.4). This is done by generating 10,000 bootstrap realizations of the HST WL mass map, where each realization is created with a random sample of the lensed source galaxy population. Then just as we do for the galaxy centroid location (see §4.2) we iteratively determine the centroid of each subcluster in each bootstrap realization of the mass map. The distribution of centroids in these bootstrap realizations is then used to calculate bias-corrected percent confidence limits [9] of the marginalized right ascension and declination distributions.

As for the effects of projected line of sight structures, Dietrich et al. [44] find in their simulations that line-of-sight structures contribute slightly ($\sim 2''$) to the lensing centroid uncertainty. Furthermore we find no evidence of significant line of sight structures using our full sample of 654 spectroscopic redshifts (with uniform selection over $0 < z < 1.0$) as well as photometric redshifts (see further discussion in Chapter 2). Based on our findings we confidently rule out any line of sight structures with $M_{200} \gtrsim 1 \times 10^{12} M_\odot$. Any undetected structure will have negligible impact on the offset.

Just as redshift uncertainties affect the galaxy centroid estimate (see §4.2.2) they too affect the WL centroid estimate. However unlike with the galaxy centroid estimate, spectroscopic redshifts help very little to improve the WL centroid estimate. This is because most of the lensing information comes from the large number of faint ($R \gtrsim 23$) galaxies that predominately make up the lensed source population. There is negligible spectroscopic information available for this population. So we rely almost entirely on photometric magnitude, color, and redshift information. Fortunately WL is not quite as sensitive to these errors as the galaxy membership determination due to the relatively broad lensing redshift kernel (see

Equation 2.4)⁵. However it is still important to properly account for the inherently large errors associated with photometric redshifts. The full $p(z)$ tomographic lensing method introduced in §2.4 is designed to do just that. The method’s effectiveness has recently been shown in the case of Abell 781 (Wittman, Dawson, & Benson, 2013) where it increased the signal-to-noise of the Abell 781-D subcluster by $\sim 40\%$, thereby resolving the missing WL mass mystery [34].

4.4.2 Dissociative Merger Systematic Errors

To estimate the systematic error associated with using the WL centroid to estimate the DM centroid in dissociative mergers we have developed simple simulations. In these simulations we model the projected surface mass density of each subcluster assuming NFW halo properties measured from the WL analysis (§2.4) and locate the NFW halos at the projected locations of the galaxy centroid of each subcluster. We also model the projected surface mass density of the gas by placing NFW halos at the location of the south and central location. It is highly unlikely that the gas concentrations of the Musket Ball cluster take the form of NFW halos, however it is also unlikely that the specific distribution of the gas mass matters as much as the location and magnitude of the gas mass⁶. We then apply the same iterative centroid estimate procedure to the simulated projected surface density map at the locations of the north and south subclusters. We then compare the estimated centroid of the total surface density map with the known location of the subcluster’s simulated DM halo. In all cases we find that each subcluster’s estimated centroid is biased from the true centroid towards the center of the merger. In the case of the southern subcluster we find that the centroid offset is $7.6''$ for the best fit mass estimates of the subclusters and south and central gas concentrations. For perspective, if we double the gas mass the total offset increases to $10''$, or if we account for the uncertainty in our distribution of the gas mass the modeled centroid offset ranges from $3.4''$ to $9.4''$. In the case of the northern subcluster the bias is actually less, ranging from $(0.7'' \text{ to } 1.5'')$. Unlike the southern subcluster that has a

⁵However as previously noted, the breadth of this WL kernel is also a hindrance when determining the WL centroid, since line-of-sight massive structures can induce additional noise in WL centroid estimate of the DM halo centroid.

⁶A more thorough analysis should attempt to use the observed X-ray luminosity map to model a projected gas density distribution.

significant gas concentration just offset from the galaxies and DM of the subcluster (see e.g. Figure 4.6) in addition to the dissociated central gas concentration, the closest significant gas concentration to the northern subcluster is the central gas concentration. Since the magnitude of the WL-DM centroid bias decreases rapidly with mass separation, the northern subcluster is much less affected.

4.4.3 Weak Lensing Location Results

We find that the location of the HST WL north subcluster is $(09^{\text{h}}16^{\text{m}}11^{\text{s}} \pm 7^{\text{s}}, 29^{\circ}52'05'' \pm 13'')$ and the south subcluster is $(09^{\text{h}}16^{\text{m}}15^{\text{s}} \pm 5^{\text{s}}, 29^{\circ}49'34'' \pm 11'')$. These uncertainties are plotted as dashed ellipses in Figures 4.6 and 4.7. The centroid uncertainty in the northern cluster is slightly larger as a result of the northern subcluster being approximately half as massive as the southern subcluster (see Chapter 2). Note that these uncertainties do not include the effects of line-of-sight structures or the systematic effects discussed in §4.4.2.

As an aside, the above WL centroids are based on the iterative centroid location estimation process (see §4.1.1), while the WL location estimates reported in Dawson et al. [41] were based on the peak of the lensing distribution. The WL locations based on those peaks were $09^{\text{h}}16^{\text{m}}10^{\text{s}} \pm 30^{\text{s}}, 29^{\circ}52'10'' \pm 30''$ for the north subcluster, and $09^{\text{h}}16^{\text{m}}15^{\text{s}} \pm 8.0^{\text{s}}, 29^{\circ}49'34'' \pm 6.9''$ for the south subcluster. The results for the southern subcluster are in excellent agreement, while the increased uncertainty the northern subcluster can be attributed to originally including the small northwestern mass peak in the region used to search for the peak.

4.5 Gas–Weak Lensing Offset

The peak of the gas distribution $(09^{\text{h}}16^{\text{m}}15^{\text{s}} \pm 5.5^{\text{s}}, 29^{\circ}50'59'' \pm 5.0'')$ derived from X-rays is offset $1.4' \pm 0.49$ from the North HST WL mass peak $(09^{\text{h}}16^{\text{m}}11^{\text{s}} \pm 7^{\text{s}}, 29^{\circ}52'05'' \pm 13'')$, and $1.4' \pm 0.14$ from the South HST WL mass peak $(09^{\text{h}}16^{\text{m}}15^{\text{s}} \pm 5^{\text{s}}, 29^{\circ}49'34'' \pm 11'')$, and is located near a local minimum in the mass (see Figure 2.5). Given the significant offset between the WL and gas locations we are able to use the first method of Markevitch et al. [93] and place a rough limit on the DM self-interaction cross-section, σ_{DM} . This method compares the scattering depth of the dark matter, $\tau_{\text{DM}} = \sigma_{\text{DM}} m_{\text{DM}}^{-1} \Sigma_{\text{DM}}$, with that of the ICM gas, $\tau_{\text{ICM}} \approx 1$, where m_{DM} is the DM particle mass and Σ_{DM} is the surface mass density of the DM particles. Σ_{DM} is approximately the WL measured surface mass density, Σ , since

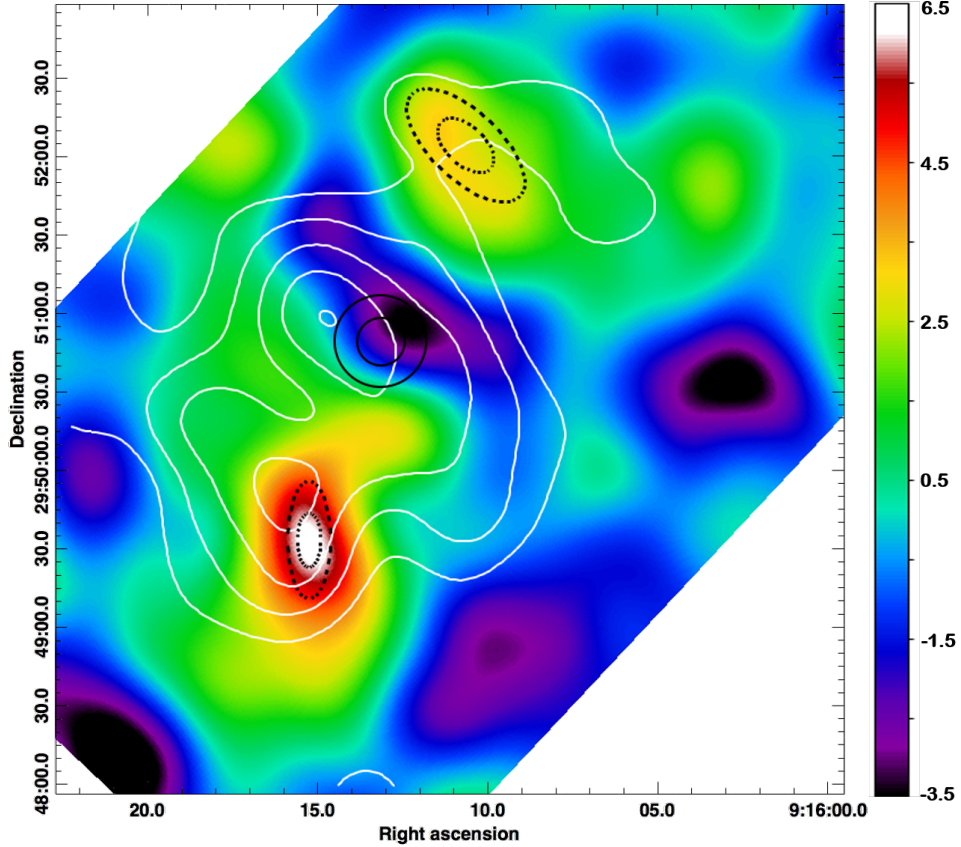


Figure 4.6: HST space-based WL mass signal-to-noise map of the Musket Ball Cluster with the X-ray distribution overlay (white contours). The 68% and 95% centroid confidence intervals are shown for the north and south subcluster WL centroids (dashed black ellipses) as well as the central gas distribution (solid black ellipses). The majority of the cluster gas is centered $\sim 1.4'$ between the North and South subclusters.

$\sim 80\%$ of a typical cluster's mass is DM [43]. For ease of comparison with the results of Markevitch et al. [93] and Merten et al. [100] we examine the surface density averaged over the face of the subcluster within $r=125$ kpc, which is $\Sigma \approx 0.15 \text{ g cm}^{-2}$; thus we find $\sigma_{\text{DM}} m_{\text{DM}}^{-1} \lesssim 7 \text{ cm}^2 \text{ g}^{-1}$.

4.6 Galaxy–Weak Lensing Offset

As discussed previously it is interesting to study the galaxy-WL offset since the WL is expected to largely map the DM distribution (after accounting for the biases discussed in §4.4) and if the nearly collisionless galaxies are found to lead the DM in the merger then this could provide evidence of SIDM. Here we consider the measured galaxy-WL offset in both the north and south subclusters of the Musket Ball Cluster. We plot the WL (dashed

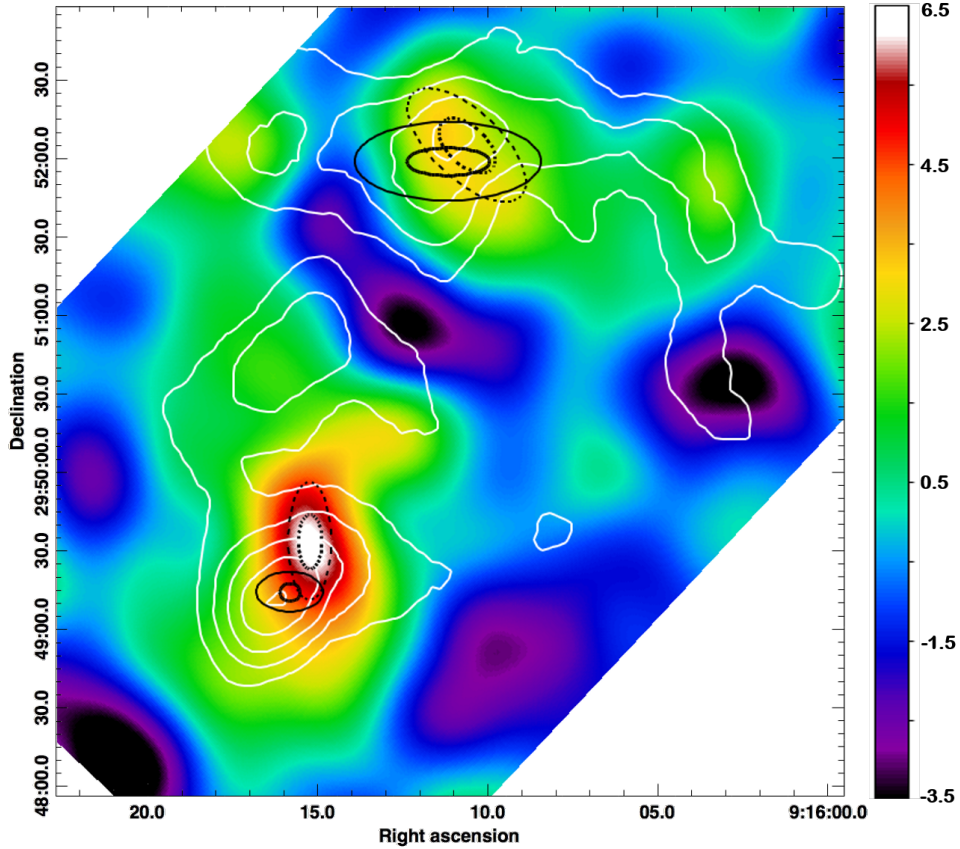


Figure 4.7: HST space-based WL mass signal-to-noise map of the Musket Ball Cluster with the spectroscopic and photometric redshift based galaxy number density overlay (white contours). The 68% and 95% centroid confidence intervals are shown for the north and south subcluster WL centroids (dashed black ellipses) as well as north and south galaxy number density centroids (solid black ellipses). Note the $20.5''$ offset between the galaxies and the WL mass in the South subcluster. However also note the $7.4''$ offset between the two in the North subcluster, but in the opposite direction (in the sense that the galaxies are trailing the WL).

black) and galaxy (solid black) centroid confidence intervals on the HST WL signal-to-noise mass map in Figure 4.7. Interestingly there is an offset of $20.5''$ (129 kpc at $z = 0.53$) in the southern subcluster where the galaxies appear to be leading the WL determined DM mass. There also exists an offset ($7.4''$; 47 kpc at $z = 0.53$) in the northern subcluster but in the opposite direction (in the sense that the WL determined mass appears to be leading the galaxies). As noted previously the larger centroid uncertainties in the northern cluster are primarily due to it being less massive and having fewer galaxies than the southern subcluster.

In Figure 4.8 we highlight the the bootstrap distributions of the galaxy centroid and WL centroid in the southern subcluster looking at a region $1.5'$ by $1.5'$. For perspective we

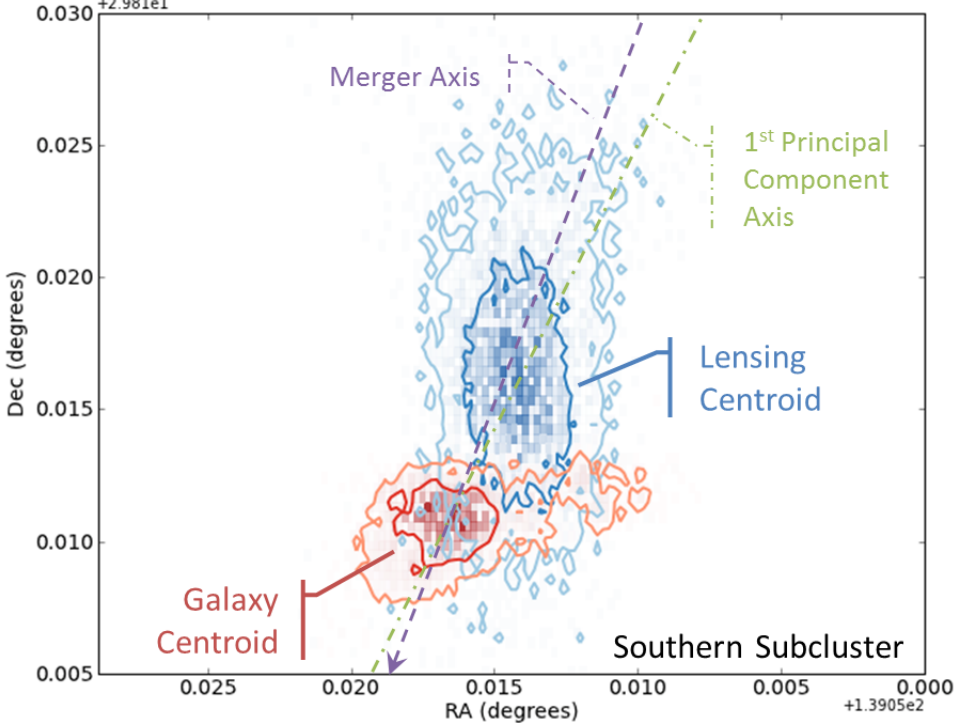


Figure 4.8: Musket Ball southern subcluster WL (blue) and galaxy number density (red) centroid probability density distribution functions constructed from 10,000 respective bootstrap realizations. The 68% (dark contours) and 95% (light contours) confidence intervals are shown for each. The region shown is 1.5' by 1.5', 567 kpc \times 567 kpc at $z=0.53$. The first principal component axis of the separation between the two distributions (dot-dashed green line) has a position angle of 159 degrees, this is close to the 153 degree position angle of the merger axis of the cluster (dashed purple line; as inferred from a line intersecting the two galaxy centroids). The outgoing merger direction is denoted by the purple arrow.

have shown the merger axis (purple dashed line), which is defined by drawing a straight line between the galaxy centroids of the north and south subclusters⁷. The outgoing merger axis direction is towards the south. Under this definition the merger axis has a position angle (PA; positive from north towards east) of 153 degrees. Interestingly the first principal component axis of the joint galaxy/WL distributions has a PA=159 degrees (green dot-dashed line). This offset seems to very closely match the expectations of SIDM.

While the southern centroids are offset by more than their respective 68% confidence intervals there remains the question of how significant this offset is, especially in light of the directional biases (§4.4.2) expected with such a measurement. To estimate this significance we pose the question: if the estimated WL and galaxy two-dimensional PDF's coincide how

⁷It is entirely possible that the actual merger trajectory is curved or that the actual axis does not pass directly through the centers of the galaxy locations.

often would one expect the observed offset ($20.5''$) of the galaxies leading the WL along the merger axis⁸? Assuming the two centroids are expected to coincide in the CDM scenario, and that the bootstrap analysis accounts for all systematic errors or random noise, then the complement of the previous probability is the confidence that $\sigma_{\text{DM}} > 0$. For the case of zero expected offset between the two centroids, the observed offset suggests that $\sigma_{\text{DM}} > 0$ with $\sim 97\%$ confidence (see where the blue curve of Figure 4.9). However as we pointed out in §4.4.2 the directional biases due to the mass of the northern subcluster and the mass of the gas can cause the WL centroid to be offset away from the true DM centroid towards the center of the merger by $\sim 3.4''$ to $9.4''$ (red region) with an expectation of $\sim 7.6''$ (dashed red line). Once these biases are taken into account the confidence that $\sigma_{\text{DM}} > 0$ falls to $\sim 83\%$.

However there remains the observation that the galaxies appear to be trailing the DM slightly in the northern subcluster (see Figure 4.7). Figure 4.10 for the northern subcluster is analogous to Figure 4.8 for the southern subcluster. It also shows a region $1.5'$ by $1.5'$, note however in this case that the outgoing merger axis direction is towards the north. Neither distribution is as well defined as the distributions in the south and the first principal component axis of the joint galaxy and WL centroid distributions has a PA = 116 degrees (v.s. the merger axis PA = 153 degrees). Despite this, it appears as though the galaxy centroid distribution is trailing the WL centroid distribution. Other than noise there is no physical explanation for such an offset⁹, and it is clearly at odds with the SIDM expectations.

Given that the northern galaxy-WL offset appears at odds with galaxy-WL offset in the south (in regards to the observed offset in the south being evidence for SIDM), it seems reasonable to jointly analyze the observed offsets when attempting to infer the confidence that $\sigma_{\text{DM}} > 0$. Beyond fully simulating the system it is not entirely clear on the best way to do this, since the two measurements are not necessarily independent (due to their mutual dependence on the gas mass and the possibility that there is a global astrometry shift between the optical and lensing maps). However, a reasonable option is to simply add the galaxy-WL offsets of the north and south subcluster ($\Delta x'_{\text{North}} + \Delta x'_{\text{South}}$) in each bootstrap realization, then compare this distribution, where the galaxy-WL offset in each cluster is defined to

⁸This is a one-tailed test.

⁹Care has been taken to make sure that the multi-wavelength astrometry is accurate. Thus there should *not* be a translational shift from one map to another, which could cause an offset similar to what is observed.

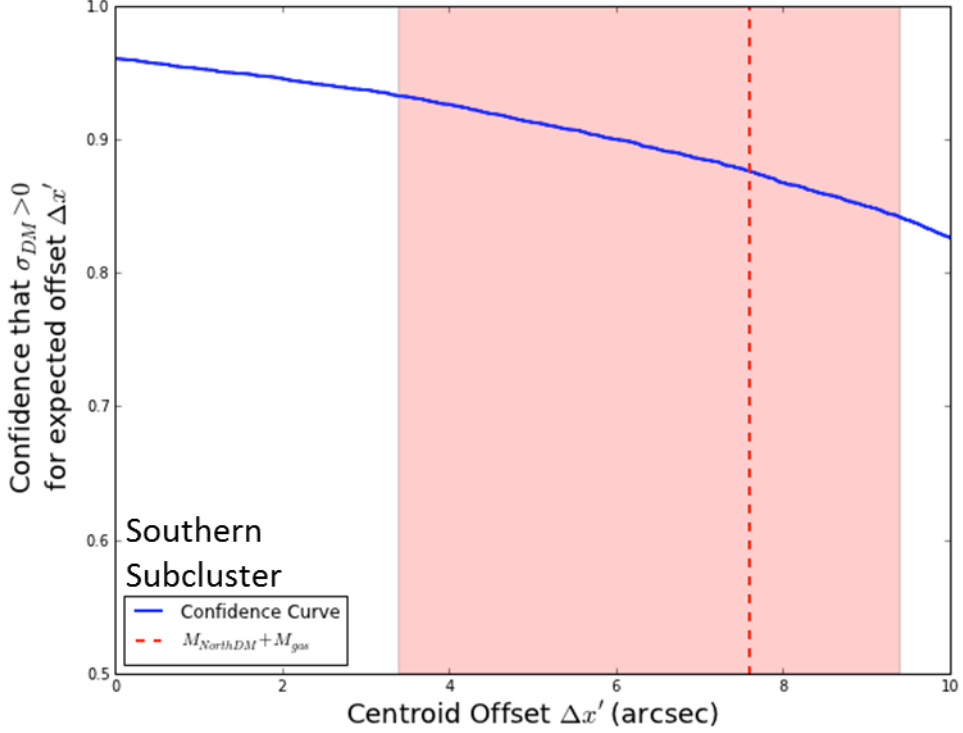


Figure 4.9: Musket Ball southern galaxy-WL centroid offset significance, in terms of confidence that $\sigma_{\text{DM}} > 0$. If there is no physical reason, other than SIDM, to expect an offset where the galaxies lead the WL ($+\Delta x'$) then confidence that $\sigma_{\text{DM}} > 0$ should where the blue curve crosses $\Delta x' = 0$ ($\sim 97\%$ confidence), which as discussed in the body of this section is an improper assumption to make. The red region shows the expected offset caused by the directional biases of the mass of the northern subcluster and the mass of the gas (see §4.4.2) with the most likely offset represented by the dashed red line. Since the non-SIDM effects are expected to cause an offset the confidence of $\sigma_{\text{DM}} > 0$ fall to $\sim 83\%$. The galaxy-WL centroid offset is measured along the merger axis direction (x') with positive offsets being when the galaxies lead the DM (as expected in the case of SIDM).

be positive when the galaxies are leading the WL in the respective outgoing merger axis direction (x') of each subcluster. Thus if the galaxies in the north trail the WL by $7''$ and the galaxies in the south lead the WL by $20''$ for a given realization then $\Delta x'_{\text{North}} + \Delta x'_{\text{South}}$ will equal $13''$ for that bootstrap realization. The result of this convention is shown as the blue curve in Figure 4.11. Comparing with the confidence curve for just the south subcluster shows that the confidence that $\sigma_{\text{DM}} > 0$ has dropped from $\sim 85\%$ to $\sim 55\%$. Furthermore the region of the expected centroid offset due to non-SIDM bias has been increased slightly to account for both the offset bias in the north and south (see §4.4.2). While this analysis is simple it does serve to place an approximate bookend on the confidence that $\sigma_{\text{DM}} > 0$, suggesting that the confidence should be between $\sim 55\text{--}85\%$.

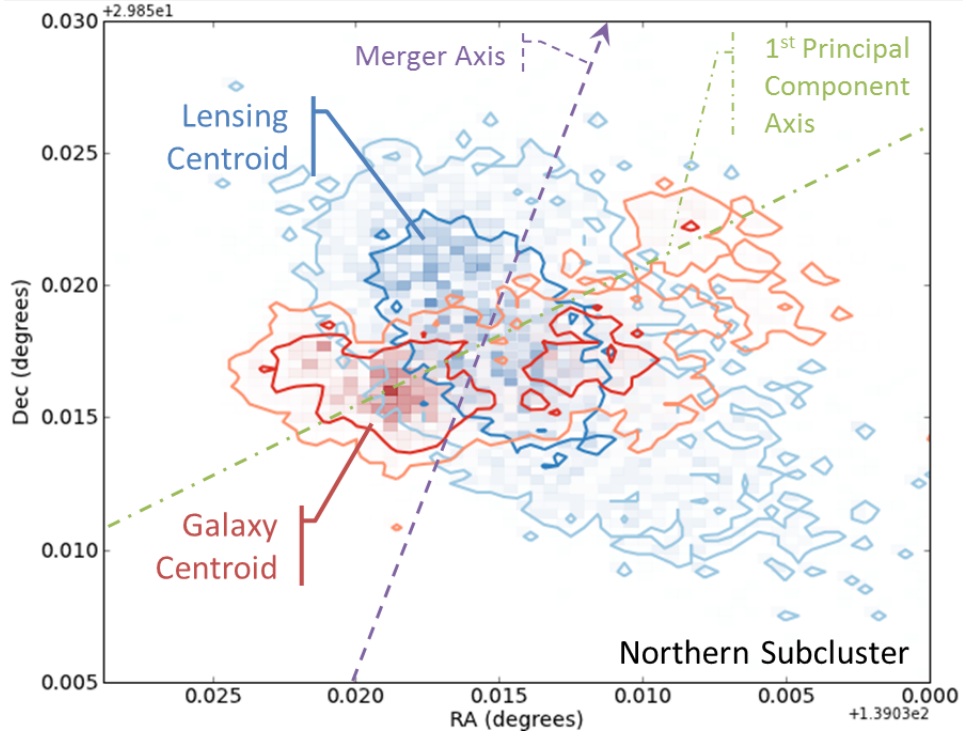


Figure 4.10: Musket Ball northern subcluster WL (blue) and galaxy number density (red) centroid probability density distribution functions constructed from 10,000 respective bootstrap realizations. The 68% (dark contours) and 95% (light contours) confidence intervals are shown for each. The region shown is 1.5' by 1.5', 567 kpc \times 567 kpc at $z=0.53$, the same scale as Figure 4.8. The merger axis of the cluster (as inferred from a line intersecting the two galaxy centroids) is plotted as a dashed purple line; its position angle is 153 degrees. The first principal component of the joint distributions has a position angle of 116 degrees (dot-dashed green line). The outgoing merger direction is denoted by the purple arrow. Unlike the southern subcluster (Figure 4.8) there does not appear to be as significant of an offset between the locations, however what offset there is, is contrary to the SIDM expectations or any physical expectations. Both centroids in the northern subcluster are less well defined than the centroids in the southern subcluster; most notably the galaxy density centroid which appears bimodal.

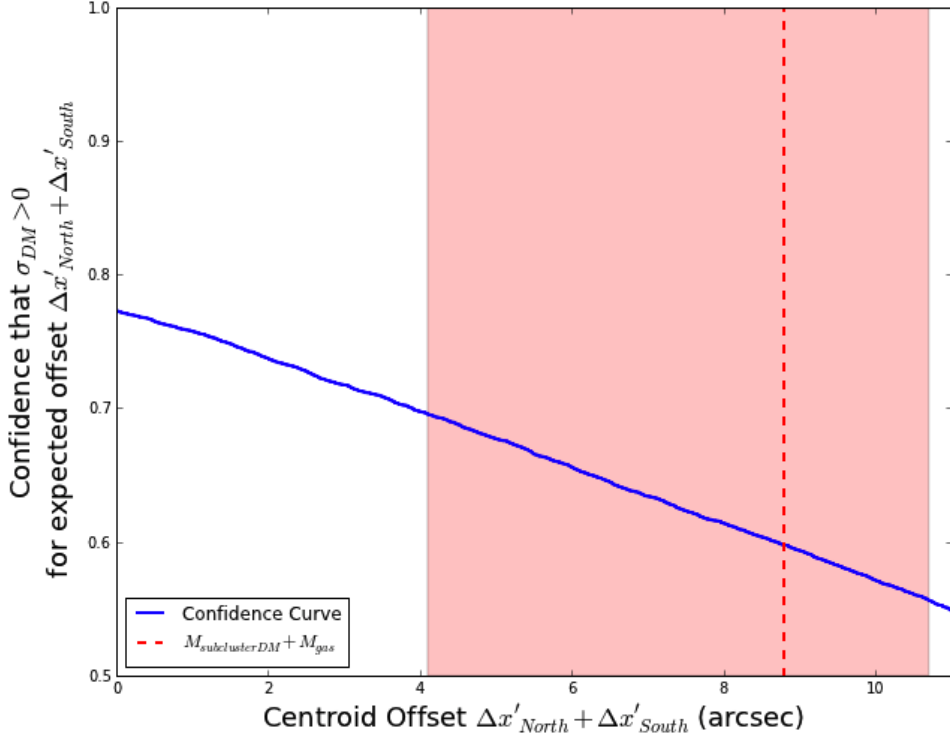


Figure 4.11: Musket Ball joint north and south galaxy-WL centroid offset significance, in terms of confidence that $\sigma_{DM} > 0$. If there is no physical reason, other than SIDM, to expect an offset where the galaxies lead the WL ($+\Delta x'$) then confidence that $\sigma_{DM} > 0$ should where the blue curve crosses $\Delta x' = 0$ ($\sim 78\%$ confidence), which as discussed in the body of this section is an improper assumption to make. The red region shows the expected offset caused by the directional biases of the mass of the other subcluster and the mass of the gas (see §4.4.2) with the most likely offset represented by the dashed red line. Since the non-SIDM effects are expected to cause an offset the confidence of $\sigma_{DM} > 0$ fall to $\sim 55\%$.

4.7 Summary

In this chapter we presented our measurements of the gas, galaxy, and WL centroids of the Musket Ball Cluster. We are able to constrain the central gas distribution's projected centroid to within $9''$ (57 kpc at $z=0.53$), see §4.3. Using both the extensive spectroscopic and photometric redshifts we are able to constrain the galaxy centroid of the northern subcluster to within $5.3''$ (33 kpc at $z=0.53$) and the galaxy centroid of the southern subcluster to within $3.3''$ (21 kpc at $z=0.53$), see §4.2. Using our tomographic WL method applied to the HST measured shapes we are able to constrain the projected WL centroid of the northern subcluster to within $13''$ (82 kpc at $z=0.53$) and the WL centroid of the southern subcluster to within $11''$ (69 kpc at $z=0.53$), see §4.4.

Given the accuracy of the gas and WL centroid measurements we are able to confidently

state that the $1.4'$ offset of the central gas concentration halfway between the north and south WL subclusters is clear evidence of the Musket Ball Cluster being a dissociative merger, see §4.5. Furthermore we use these measurements in conjunction with gas-WL offset method of Markevitch et al. [93] to place a constraint on $\sigma_{\text{DM}} m_{\text{DM}}^{-1} \lesssim 7 \text{ cm}^2 \text{ g}^{-1}$. Since this method has an inverse dependence on the surface mass density of DM it is not surprising that this constraint from the Musket Ball is looser than existing similar constraints from more massive clusters [19, 93, 100].

Upon investigating the galaxy-WL offset we find that galaxies in the southern subcluster appear to be leading the WL centroid by $\sim 20.5''$ (129 kpc at $z=0.53$), see §4.6. The 159 degree PA of this offset is inline with the 153 degree PA of the merger axis. Such an offset could be caused by SIDM. However, such an offset could also be caused by several directional biases inherent in the WL estimate of the DM location, see §4.4.2. Although we find that these directional biases could account for at most an offset of $9.4''$. Given this and the centroid uncertainties we find that such a large offset due to non-SIDM physics should occur less than 5–15% of the time, suggesting that $\sigma_{\text{DM}} > 0$ with $\sim 85\%$ confidence.

Interestingly though we find that galaxy-WL centroid offset in the north seems to contradict the SIDM scenario, see §4.6. For this subcluster we find that the galaxies are trailing the WL centroid along the merger axis by $\sim 7.4''$ (47 kpc at $z=0.53$). Other than noise there is no physical explanation for such an offset. We adjust the $\sigma_{\text{DM}} > 0$ confidence from the observed offset in the southern subcluster by directly combining the countering offsets in the north and south along the merger axis. This analysis suggests that the confidence of $\sigma_{\text{DM}} > 0$ should be lowered to $\sim 55\%$.

On a final note, Figure 2.5 shows that the southern mass peak in the Subaru WL map is actually leading the galaxies to some degree. However this is likely just a result of the the ground-based WL peak uncertainty being ~ 5 times larger than the uncertainty of the HST measured centroid. A good indication of this is that the HST centroid lies within the high-likelihood region of the Subaru data, but the Subaru centroid does not lie within the high-likelihood region of the HST data. While disregarding the Subaru data for the current analysis is reasonable, future analyses should incorporate this data for completeness.

4.8 Discussion

It is difficult to make any definitive conclusions about SIDM from the observed galaxy-WL offsets in the Musket Ball Cluster. While the SIDM scenario is slightly preferred over the CDM scenario, given the many assumptions noted in this chapter, it is not significantly so. There are a number of actions that can be taken to help clarify the situation.

(*i*) CDM and SIDM simulations of the Musket Ball Cluster merger, similar to the Randall et al. [127] simulations of the Bullet Cluster. Not only are these necessary to translate the observed offsets into quantitative constraints on σ_{DM} , but they should prove invaluable in helping to quantify the systematic errors that have been approximated in this analysis, as well as identify possible systematic errors that have to this point been disregarded.

(*ii*) A better observational measure of the expected SIDM effects. While the offset of the galaxy-WL centroids is a reasonable measure, it is not likely to be the best measure of the expected SIDM effect. The centroid measurement heavily bins the raw lensing and galaxy information, and data binning is always a lossy process. Thus it is conceivable to reduce the current uncertainties with methods that more directly compare the galaxy and WL surface mass distributions. Evidence for this can be seen in the recent SIDM simulations of Kahlhoefer et al. [79], where they find that peaks of the galaxy and SIDM distributions shift negligibly during mergers however there are notable shifts in the outer half of the two distributions. But as far as the centroid measurement is concerned it would be worth investigating the effects of weighting the galaxies by luminosity or stellar mass in addition to membership probability.

(*iii*) Study more dissociative mergers. Taking an ensemble approach to measuring the galaxy-WL offset will not only help reduce the random errors associated with the measurement but will potentially help with our understanding of the intrinsic scatter in such a measurement. Also Kahlhoefer et al. [79] find that the magnitude of SIDM effect is expected to vary among mergers depending on the properties of the merger. So there is not only the possibility of finding another merger where the offset is larger, but the varying magnitude of the observed offsets from merger to merger could potentially be used as a consistency check for a given SIDM model.

(*iv*) Better understand the intrinsic scatter of the galaxy-DM offset. In this work it has

been presumed that the galaxies trace the DM distribution. It is not known at what level this will break down, however it is possible to get some handle on this by studying the galaxy-DM offset in relaxed clusters, both observed and simulated. Any offset scatter observed in these relaxed systems can be assumed as the base noise level for merging systems.

(v) Account for the galaxy centroid directional offset bias (see §4.2). This bias should act in a positive manner to counter some of the directional offset bias of the WL measurement (which has been accounted for in the current analysis). About half of the expected WL offset bias comes from the mass of the gas and about half comes from the mass of the other subcluster. If the galaxies perfectly trace the DM then the galaxy centroid should also be biased towards the center of the merger by the same amount that the WL measurement is biased towards the center by the mass of the other subcluster. Thus the expected systematic galaxy-WL offset should only be $\sim 5''$ instead of $\sim 9''$. In this case the confidence that $\sigma_{\text{DM}} > 0$ should be adjusted to $\sim 0.7\text{--}0.9$.

(vi) More observations of the Musket Ball Cluster. While the current HST observations are sufficiently deep that further observations will not increase the number of source galaxies significantly, it is possible to improve the purity and completeness of the lensed source population, thereby improving the WL signal-to-noise. Additionally deeper X-ray observations would enable better modeling of the gas mass and associated directional galaxy-WL bias. However neither of these are expected to improve the confidence of the measurements to such a degree that the problem of σ_{DM} will be solved.

(vii) Better galaxy membership estimation. As previously noted there is potential for improving the galaxy membership estimation by attempting to adjust the cluster membership criteria in order to simultaneously minimize the joint uncertainty due to cluster membership noise and Poisson noise of the centroid estimate. This should improve the galaxy centroid measurement, and may become even more important as new galaxy location schemes based more strongly on the galaxy population as a whole are developed (see point *ii*).

Finally, one of the most important lessons learned from this analysis is that both sub-clusters of the merger should be used when estimating the significance of the offsets between galaxies, gas, and WL, especially in the case of near-equal mass mergers.

Chapter 5

Perspective: Summary & Discussion

In this chapter we summarize the work presented in this dissertation. We follow this summary with a discussion of the challenges that must be overcome if merging clusters are to reach their true potential as dark matter probes and discuss potential solutions to these challenges.

5.1 Dissertation Summary

Over the past century our understanding of the Universe has undergone dramatic revisions which have culminated in accurate (percent level) measurements of the composition of the universe. While the general scientific community agrees upon the composition of the universe, the properties of the bulk of this composition (dark matter and dark energy) remain a mystery. This dissertation has presented our recent efforts to better understand the properties of dark matter (DM).

In Chapter 1 we provided a brief review of the history of DM (§1.2.1), showing that while Fritz Zwicky provided the first evidence of DM in 1933 [172] it wasn't until the work of Vera Rubin and collaborators [131] in the 1970's that DM garnered much attention. Three general candidates for DM originally dominated the debate: it was simply massive compact objects made up of standard model particles, or it was that it was some new particle, or it was that general relativity needed to be modified. The MACHO experiment [2] eventually ruled out the possibility that massive compact objects made up the bulk of DM, and merging galaxy clusters ruled out modified gravity [29] thus providing strong evidence for DM being a new

particle. We reviewed the generally accepted cold dark matter (CDM) properties (§1.2.2) but provided motivation for considering that DM might actually interact with itself other than through gravity (SIDM model; §1.3). We also reviewed the possible probes of SIDM (§1.4), highlighting merging galaxy clusters (§1.5) and the four methods of constraining SIDM with observations of merging clusters.

In Chapter 2 we introduced the the merging galaxy cluster DLSCL J0916.2+2951 (also known as the Musket Ball Cluster) and presented our multi-wavelength studies of the system. Our photometric and spectroscopic observations show that the system consists of two subclusters separated by a projected distance of 1.0 ± 0.1 Mpc and a line-of-sight velocity difference of $v_{\text{los}} = 670^{+270}_{-330} \text{ km s}^{-1}$. Thus the two subclusters are close enough to be physically associated with one another. Our weak lensing analysis of the north and south subclusters show that they have comparable mass ($1.7^{+2.0}_{-0.72} \times 10^{14} M_{\odot}$ and $3.1^{+1.2}_{-0.79} \times 10^{14} M_{\odot}$, respectively), suggesting that the system is a major merger. Our Sunyaev-Zel'dovich effect and X-ray observations show that the cluster gas is located between the two subclusters proving that the Musket Ball Cluster is a post merger system where the collisional gas has become dissociated from the effectively collisionless galaxies and DM. Thus the Musket Ball Cluster is an excellent candidate to constrain the DM self-interaction cross-section (σ_{SIDM}).

In Chapter 3 we discussed the importance of understanding the dynamic history of mergers when attempting to use them to constrain the properties of DM. We developed a new Monte Carlo based method to discern the properties of dissociative mergers and propagate the uncertainty of the measured cluster parameters in an accurate and Bayesian manner. We verified it against an existing hydrodynamic N-body simulation, and applied it to two known dissociative mergers: 1ES 0657-558 (Bullet Cluster) and the Musket Ball Cluster. We find that the dynamic properties of the Musket Ball occupy a significantly different volume of merger phase space than the Bullet Cluster. The Musket Ball Cluster, being $3.4^{+3.8}_{-1.4}$ times further progressed than the Bullet Cluster, could potentially provide tighter constraints on σ_{DM} since the offset between galaxies and dark matter should initially increase with time post-merger for $\sigma_{\text{DM}} > 0$.

In Chapter 4 we compared the locations of the galaxies, gas, and DM in the Musket Ball Cluster to provide insight into the properties of DM. We constrain the central gas

distribution's projected centroid to within $9''$ (57 kpc at $z=0.53$), see §4.3. Using both the extensive spectroscopic and photometric redshifts we constrain the galaxy centroid of the northern subcluster to within $5.3''$ (33 kpc at $z=0.53$) and the galaxy centroid of the southern subcluster to within $3.3''$ (21 kpc at $z=0.53$), see §4.2. And using our tomographic WL method applied to the HST measured shapes we constrain the projected WL centroid of the northern subcluster to within $13''$ (82 kpc at $z=0.53$) and the WL centroid of the southern subcluster to within $11''$ (69 kpc at $z=0.53$), see §4.4. Our measurement of a significant offset of the gas between the DM in each subcluster enabled us to achieve the constraint $\sigma_{\text{DM}} m_{\text{DM}}^{-1} \lesssim 7 \text{ cm}^2 \text{ g}^{-1}$. Given the dependence on the surface mass density of this method it is not surprising that this constraint is less than that achieved with more massive mergers [19, 93, 100]. Finally in this chapter we investigated the galaxy-WL offset, since if DM self-interacts then the effectively collisionless galaxies might be expected to lead the DM post-merger. While we find that the galaxies appear to be leading the WL centroid in the southern subcluster by $\sim 20.5''$ (129 kpc at $z=0.53$), see §4.6, this only provides $\sim 85\%$ confidence that $\sigma_{\text{DM}} > 0$. Furthermore, when we account for the observation that the galaxy centroid appears to trail the WL centroid in the northern subcluster by $\sim 7.4''$ (47 kpc at $z=0.53$), the confidence that $\sigma_{\text{DM}} > 0$ falls to $\sim 55\%$. While the SIDM scenario is slightly preferred over the CDM scenario it is not significantly so. SIDM simulations of the Musket Ball Cluster are needed to turn these observations into quantitative constraints on σ_{DM} .

5.2 Discussion on the Path Forward

There are a number of outstanding uncertainties/challenges that must be overcome before merging clusters are proven capable of obtaining the necessary SIDM constraints to either measure σ_{DM} or constrain it to the point of being astrophysically uninteresting.

5.2.1 Uncertainty in the Location of Galaxies and DM/Lensing

Perhaps the most notable challenge is related the results from the recent theoretical studies of SIDM effects in merging clusters by Kahlhoefer et al. [79] (which were presented in the arXiv one week before the completion of this dissertation). There are a number of promising results from their study which support claims made previously in this dissertation (e.g., they confirm the expectation that the galaxy-DM offset increases following the merger, and also

confirm that for some models of DM, common mergers such of the Musket Ball Cluster can have more constraining power than extreme mergers such as the Bullet Cluster). However, one result from their study casts doubt on the possible effectiveness of merging galaxy clusters to constrain SIDM. In particular, they find that the typical galaxy-DM offset ranges between \sim 5–15 kpc for allowable ranges of σ_{DM} . This is much smaller than the galaxy and WL centroid uncertainties typically measured for galaxy clusters (\sim 20–100 kpc). And since most mergers don't occur directly in the plane of the sky, the observable projected offset will be \lesssim 5–15 kpc, assuming the Kahlhoefer et al. [79] results are correct. Even disregarding intrinsic scatter of the galaxy-DM location and systematic offset effects due to the dissociated gas and other subcluster mass, it will take a large number of dissociative mergers to reach the \sim 10 kpc offset level. Take for example the Musket Ball Cluster studied in this dissertation. We find that we are able to constrain the galaxy centroid in each subcluster to $\sim \pm 25$ kpc and the WL centroid in each subcluster to $\sim \pm 70$ kpc. This roughly translates to a centroid offset uncertainty of $\sigma_{\text{offset}} \sim 80$ kpc (again for argument's sake disregarding other systematic offset errors). Since the offset measurement is largely Poisson noise dominated (i.e. $\sigma_{\text{offset}} \propto N^{-1/2}$), it will take roughly 14–128 dissociative mergers¹ similar to the Musket Ball Cluster to achieve the necessary centroid accuracy of \lesssim 5–15 kpc. While this example is highly simplified, and it is not clear how general or accurate the Kahlhoefer et al. [79] results are, it does highlight the magnitude of this challenge and the importance of investigating it further.

Along these lines, the intrinsic scatter between the location of the galaxies and DM in galaxy clusters is still not accurately known. If the intrinsic scatter is of order the centroid measurement uncertainty then this will add significantly to the challenge of constraining SIDM with the galaxy-WL offset measurement in dissociative mergers. Two immediate means of constraining this intrinsic scatter is through studies of the scatter in existing simulations and observations of relaxed cluster systems, which should provide a lower limit on the expected scatter in merging systems. A number of high resolution simulations of relaxed clusters exist [e.g. 121, 130, which include both CDM and SIDM simulations]. By

¹Assuming that two centroid offset measurements can be made for each dissociative merger, since there are two subclusters per dissociative merger.

treating the subhalos in the cluster simulation as galaxies, one could estimate the intrinsic galaxy-DM offset. Alternatively a purely observational approach could study the galaxy-lensing offset in a sample of well measured relaxed clusters. For example the Cluster Lensing and Supernova Survey with Hubble (CLASH) galaxy cluster sample (20 relaxed clusters, $\sim 5\text{--}30 M_{\odot}$) provides excellent weak and strong lensing data to locate the DM as well as 16-band photometric redshifts to identify cluster members for the galaxy population location. Researchers of the Merging Cluster Collaboration are pursuing both avenues.

5.2.2 Find and study more dissociative mergers

Regardless of the magnitudes involved in the intrinsic scatter of the galaxy-WL/DM offset, it will be important to study as many dissociative mergers as possible in order to reduce this noise. Fortunately the number of confirmed dissociative mergers has been increasing at a rapid rate (see Figure 5.1). Prior to 2013 all of the dissociative mergers were serendipitously discovered, often requiring photometric, spectroscopic, lensing and X-ray observations for identification. The rapid rise in the number of confirmed mergers after 2013 is due to the radio relic selection method. Radio selection is an efficient way to identify dissociative mergers because the shock produced by a merger results in a “radio relic” (uniquely diffuse emission in an arc around part of the cluster, e.g. van Weeren et al. 2010). So rather than needing photometric, spectroscopic, lensing and X-ray observations it is possible to identify dissociative mergers with just radio observations. Thus wide-area radio surveys can provide many candidates. NVSS has already found a few dozen, and LOFAR is projected to find about 1000 [114]. The Merging Cluster Collaboration has begun an extensive follow-up of these radio relic mergers (see the red points in Figure 5.1 after 2013) with Keck spectroscopy, Subaru and HST imaging (archival and recently awarded: GO-13343, Co-PI Wittman, Co-PI Dawson), and Chandra and XMM X-ray imaging.

Another promising avenue of dissociative merger discovery is with the optical-Sunyaev Zel’dovich effect identification method that led to the discovery of the Musket Ball Cluster. Since the DES optical survey [145] will overlap much of the SPT [132] and ACT [72] Sunyaev-Zel’dovich effect (SZE) surveys it will be possible to search for significant offset of an SZE peak between a bimodal distribution of galaxies. Based on the simulated and

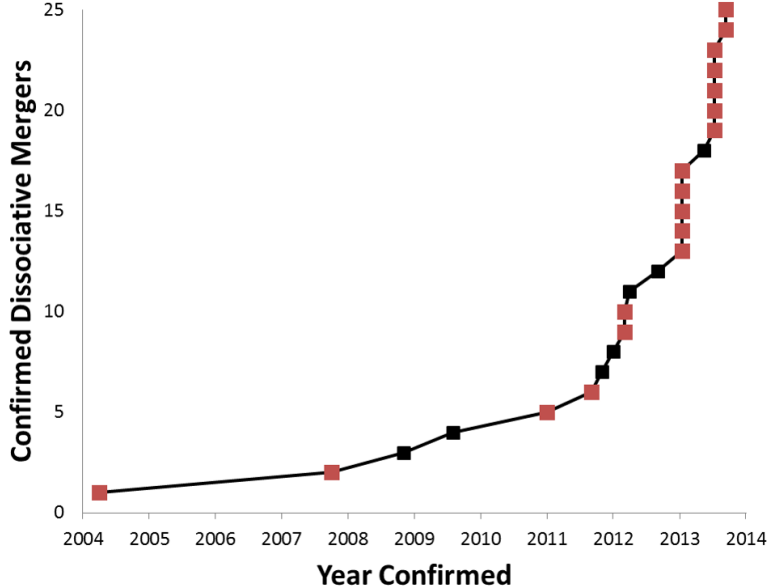


Figure 5.1: Number of confirmed dissociative mergers as a function of time. The red points identify mergers that the Merging Cluster Collaboration are studying to constrain the properties SIDM. Up until 2013 dissociative mergers were all serendipitously discoveries. The rapid rise in the number of confirmed mergers after 2013 is due to the radio relic selection method.

observed SZE cluster counts in the SPT survey [141, 155] and the fraction of all clusters that are dissociative mergers [54] we estimate that ~ 50 detectable dissociative mergers will be observed in the 4000 degree² SPT-DES survey. Selection bias will result in mergers with large mass (i.e., better signal-to-noise) and large projected separations (i.e., later stage mergers where the expected DM-galaxy offset is maximized). These will potentially be some of the best dissociative mergers with which to constrain σ_{DM} , although there is the potential disadvantage that these typically higher redshift clusters and their angular scales will be smaller.

Looking further into the future, the LSST optical survey [149] will cover a larger area than DES and go much deeper. When it is coupled with upcoming all-sky X-ray surveys (e.g., eROSITA), that will enable much better angular resolution of the gas compared to SPT and ACT, there is the possibility to discover thousands of dissociative mergers. Additionally, LSST will have multi-band photometric redshifts and excellent lensing quality data. Thus it is conceivable that the field of dissociative merger science will enter an era where the statistical errors no longer dominate the measurements.

5.2.3 Going from Observations to Dark Matter Constraints

Beyond the challenges associated with making the galaxy-DM offset measurement there remains the challenge of translating that measurement into a constraint on σ_{DM} . This challenge has both an observational element and a theoretical element.

Observationally it is possible to measure the projected galaxy-DM offset but this needs to be translated into a three-dimensional offset. As noted in Chapter 3, there are severe limitations in our ability to do this, largely due to the difficulty in constraining the angle of the merger axis with respect to the plane of the sky (α). With just the commonly available measurements of the subclusters (mass, relative velocities along the line of sight, and projected separation) the magnitude of the three-dimensional distance errors often exceeds the actual distances being measured (see e.g. d_{3D} of Tables 3.2 and 3.3). This is potentially a serious problem since there is only a factor of $\sim 2\text{--}4$ difference between the expected galaxy-DM offset of different σ_{DM} models [79, 93]. Fortunately though, moderate constraints on α can translate to significant constraints on d_{3D} . Take for example the Bullet Cluster with the added temporal prior (§3.3.2.2) where a factor of two improvement on the α uncertainty was accompanied by a factor of 9 improvement on the d_{3D} uncertainty. An added advantage of our radio relic sample is that radio polarization measurements of the radio relic can place an upper limit on α [47], for example in the case of CIZA J2242.8+5301 the polarization measurements translated to an upper limit on α of 30 degrees. Thus it is conceivable that this element of the challenge is not a daunting as it might seem.

The other major element of the challenge of translating the galaxy-DM measurement into a constraint on σ_{DM} is theoretically predicting the galaxy-DM offset for a given σ_{DM} . Randall et al. [127] showed that a promising technique is simulating a merger with collisionless “galaxy” particles and DM particles with varying σ_{DM} between runs. However there were a number of simplifying assumptions in their simulations that must be addressed if dissociative mergers are going to accurately constrain σ_{DM} :

- (i) They only modeled a single analog of the Bullet Cluster. By only choosing to model one analog of the Bullet Cluster, that albeit was representative of the most likely observed subcluster masses and projected separation, they failed to propagate the uncertainty in the observed merger parameters to the uncertainty in the expected offset for a given σ_{DM} ; thus

the lack of uncertainty estimates in there expected offset results.

(ii) The collision velocity in their simulation is extremely high. They based their choice of collision velocity on the Mach number of the gas shock feature, but as noted in Chapter 3 there are physical reasons this velocity is an overestimate of the true relative velocity. This resulted in an overestimate of the expected offset.

(iii) The galaxies were uniformly distributed in the DM halo and they used an unreasonably large number of galaxy particles. This unrealistic assumption fails to account for the intrinsic scatter related to the Poisson noise associated with the galaxies (see §4.2).

(iv) Galaxies were not embedded in their own DM subhalos. This could affect the expected offset between the galaxies and the cluster DM halo. The DM subhalos will experience a drag force due to σ_{DM} , and this will be translated to some degree into a gravitational drag force on the galaxies due to the gravitational dominance of the subhalos on small scales.

(v) The central densities of the subclusters were unphysically cuspy for the chosen σ_{DM} . As Rocha et al. [130] found the central density of SIDM halos becomes cored as σ_{DM} increases. Since the interaction rate scales roughly as the SIDM density squared, using King profiles for all the halos can result in overestimates of the expected offset.

At the heart of problems *i–iv* is the fact that the simulations failed to take into account the wealth of cosmological prior information. One possible solution to this and all of the associated problems is identifying likely merger analogs in large cosmological N-body simulations rather than setting up a simplified toy model of the merger. And then resimulating these analogs at higher resolution with varying σ_{DM} . Perhaps the best means of identifying analog mergers is through importance sampling. Where the known properties of merger in the cosmological simulation are cast in terms of the observable properties (subcluster masses, relative line-of-sight velocity, and projected separation), then given the PDF’s of the observed properties a likelihood of each simulated analog can be calculated. Because each simulated analog of the observed merger will have an associated likelihood, we could then create a posterior PDF of the expected galaxy-DM offset for a given σ_{DM} that marginalizes over all other uncertainties associated with a given merger. It will then be possible to combine the σ_{DM} constraints in a fair and well defined manner from an ensemble of dissociative mergers and reduce the noise associated with the galaxy-DM offset constraint

method.

5.3 Concluding Remarks

The work of this dissertation has highlighted the promise that merging galaxy clusters offer to either measure σ_{DM} or constrain it to the point of being astrophysically uninteresting. It has also highlighted the many challenges that must be overcome before this promise can be realized. This is an exciting time as the merging galaxies cluster science will face most these challenges within the next couple years. While we may not have any definitive results on SIDM in this time, we will have definitively assessed the value of merging galaxy clusters as probes of SIDM.

Appendix A

Dynamics of Merging Clusters Appendix

A.1 Potential Energy of Two Truncated NFW Halos

Generically the potential energy of a two-halo system with center to center separation r is

$$V(r) = \int \Phi_1(r') dm_2, \quad (\text{A.1})$$

where $\Phi_1(r')$ is the gravitational potential of halo 1 as a function of radial distance r' from the center of the halo 1 to the mass element of halo 2, dm_2 . I derive $\Phi_1(r)$ for the case of a truncated NFW halo in §A.1.1. The integral of equation A.1 can be approximated as a summation over $N \times N$ mass elements, $m_{2_{ij}}$, each with area $dr \times d\theta$, where i and j range from $0 \rightarrow N - 1$,

$$V(r) \approx \sum_{i=0}^{N-1} \sum_{j=0}^{N-1} \Phi_1(r'_{ij} + \epsilon) m_{2_{ij}},$$

where r'_{ij} is the distance from the center of halo 1 to the 2nd halo's mass element $m_{2_{ij}}$, as derived in §A.1.2, and ϵ is the softening length which reduces the effects of artificial singularities.

A.1.1 Truncated NFW Gravitational Potential

For an axially symmetric mass distribution the potential can be expressed as a series of Legendre Polynomials

$$\Phi_n(r) = -\frac{2\pi G}{(n+1/2)r^{n+1}} \int_0^r r'^{n+2} \rho_n(r') dr' - \frac{2\pi Gr^n}{n+1/2} \int_r^\infty r'^{1-n} \rho_n(r') dr' \quad (\text{A.2})$$

where

$$\rho_n(r) = (n+1/2) \int_0^\pi \rho(r, \theta) P_n(\cos \theta) \sin \theta d\theta. \quad (\text{A.3})$$

Assuming a spherical NFW halo

$$\rho_{\text{NFW}}(r) = \frac{\rho_s}{r/r_s(1+r/r_s)^2}$$

only the zeroth order term of Equation A.3 remains

$$\rho_{\text{NFW}}(r) = \rho_0(r)$$

and Equation A.2 reduces to

$$\begin{aligned} \Phi_{\text{NFW}}(r) &= -\frac{4\pi G}{r} \int_0^r r'^2 \rho_{\text{NFW}}(r') dr' - 4\pi G \int_r^\infty r' \rho_{\text{NFW}}(r') dr' \\ \Phi_{\text{NFW}}(r) &= -\frac{4\pi G \rho_s}{r} \left[\int_0^r \frac{r'^2}{r'/r_s(1+r'/r_s)^2} dr' + r \int_r^\infty \frac{r'}{r'/r_s(1+r'/r_s)^2} dr' \right]. \end{aligned}$$

Since I truncate the NFW halo at r_{200} the ∞ in the second integral becomes r_{200} and

$$\Phi_{\text{NFW}_T}(r) = \begin{cases} -\frac{4\pi G}{r} \rho_s r_s^3 \left[\ln(1+r/r_s) - \frac{r}{r_s+r_{200}} \right], & \text{if } r \leq r_{200}; \\ -\frac{GM_{200}}{r}, & \text{if } r > r_{200}. \end{cases} \quad (\text{A.4})$$

A.1.2 Mass Elements of a Truncated NFW Halo

Given the differential mass elements for a spherically symmetric halo

$$dm = 2\pi \rho(r, \theta) r^2 \sin(\theta) d\theta dr,$$

and discretizing the mass into elements with lengths $\delta r = r_{200}/N$ and $\delta\theta = \pi/N$ the halo 2 mass elements are given by

$$m_{ij} = 2\pi \int_{i\delta r}^{(i+1)\delta r} \int_{j\delta\theta}^{(j+1)\delta\theta} \rho(r') r'^2 \sin(\theta') d\theta' dr'.$$

For an NFW halo this becomes

$$m_{ij} = 2\pi \rho_s r_s^3 [\cos(j\delta\theta) - \cos((j+1)\delta\theta)] \left[\left(1 + \frac{(i+1)\delta r}{r_s}\right)^{-1} - \left(1 + \frac{i\delta r}{r_s}\right)^{-1} + \ln \left[\frac{(i+1)\delta r + r_s}{i\delta r + r_s} \right] \right].$$

A.2 Musket Ball Cluster Redshift Catalog

The Musket Ball Cluster redshift catalog (Table A.1) contains 738 spectroscopically confirmed galaxy redshifts. The galaxies are within an $\sim 18' \times 18'$ area centered on the Musket Ball Cluster (139.05 deg, +29.85 deg). The source of the redshifts are from three separate spectroscopic surveys: 1) *LRIS 2007* was carried out on 2007 January 15 using the Keck:I LRIS instrument, 2) *DEIMOS 2011A* was carried out on 2011 March 1 & 2 using the Keck:II DEIMOS instrument, and 3) *DEIMOS 2012B* was carried out on 2013 January 16 using the Keck:II DEIMOS instrument.

The *DEIMOS 2011A* observations consisted of 6 slit masks with 1"slits and using the 1200 line mm $^{-1}$ grating, tilted to a central wavelength of 6700 Å, resulting in a pixel scale of 0.33 Å pixel $^{-1}$, a resolution of ~ 1.1 Å (50 km s $^{-1}$), and typical wavelength coverage of 5400Å to 8000Å. The *DEIMOS 2013B* observations consisted of 1 slit mask with 1"slits and using the 1200 line mm $^{-1}$ grating, tilted to a central wavelength of 6200 Å, resulting in a pixel scale of 0.33 Å pixel $^{-1}$, a resolution of ~ 1 Å (50 km s $^{-1}$), and typical wavelength coverage of 4900Å to 7500Å. The exposures for each DEIMOS mask ($\sim 3 \times 20$ minutes) were combined using the DEEP2 version of the spec2d package [111]. This package combines the individual exposures of the slit mosaic and performs wavelength calibration, cosmic ray removal and sky subtraction on slit-by-slit basis, generating a processed two-dimensional spectrum for each slit. The spec2d pipeline also generates a processed one-dimensional spectrum for each slit. This extraction creates a one-dimensional spectrum of the target, containing the summed flux at each wavelength in an optimized window. Table A.1 only includes high quality ($Q \geq 3$, see Newman et al. [111] for an explanation on the quality codes) galaxy spectra. Details of the *LRIS 2007* observations and reduction are discussed in Sehgal et al. [138].

Table A.1. Musket Ball Cluster Redshift Catalog

RA (hh:mm:ss.sss)	Dec (dd:mm:ss.ss)	PosErr (arcsec)	z	σz	Source	R (mag)	σR (mag)
09:15:40.142	+29:55:06.71	0.5	0.234777	0.000020	DEIMOS 2011A	20.983	0.007
09:15:41.501	+29:47:07.64	0.5	0.530381	0.000024	DEIMOS 2011A	23.398	0.048
09:15:41.682	+29:55:13.05	0.5	0.704062	0.000033	DEIMOS 2011A	22.586	0.024
09:15:41.726	+29:56:12.79	0.5	0.498200	0.000015	DEIMOS 2011A	22.664	0.016
09:15:42.418	+29:46:55.71	0.5	0.899342	0.000101	DEIMOS 2011A	22.246	0.017

Note. — Table A.1 is published in its entirety in the electronic edition of the *Astrophysical Journal*. A portion is shown here for guidance regarding its form and content.

A.3 Bullet Cluster Result Plots

This section contains the parameter results array plots for the Bullet Cluster case including the added temporal prior of §3.3.2.2. For ease of display the parameters are grouped in three categories (*Input*, *Geometry*, and *Velocity & Time*) resulting in a six subplot results array, see Figure A.1. The *Input* parameters consist of: M_{200_1} , M_{200_2} , z_1 , z_2 , and d_{proj} , where halo 1 refers to the “main” subcluster and halo 2 refers to the “bullet” subcluster. The *Geometry* parameters consist of the randomly drawn α , and calculated d_{3D} , and d_{max} . The calculated *Velocity & Time* parameters consist of: TSC_0 , TSC_1 , and T .

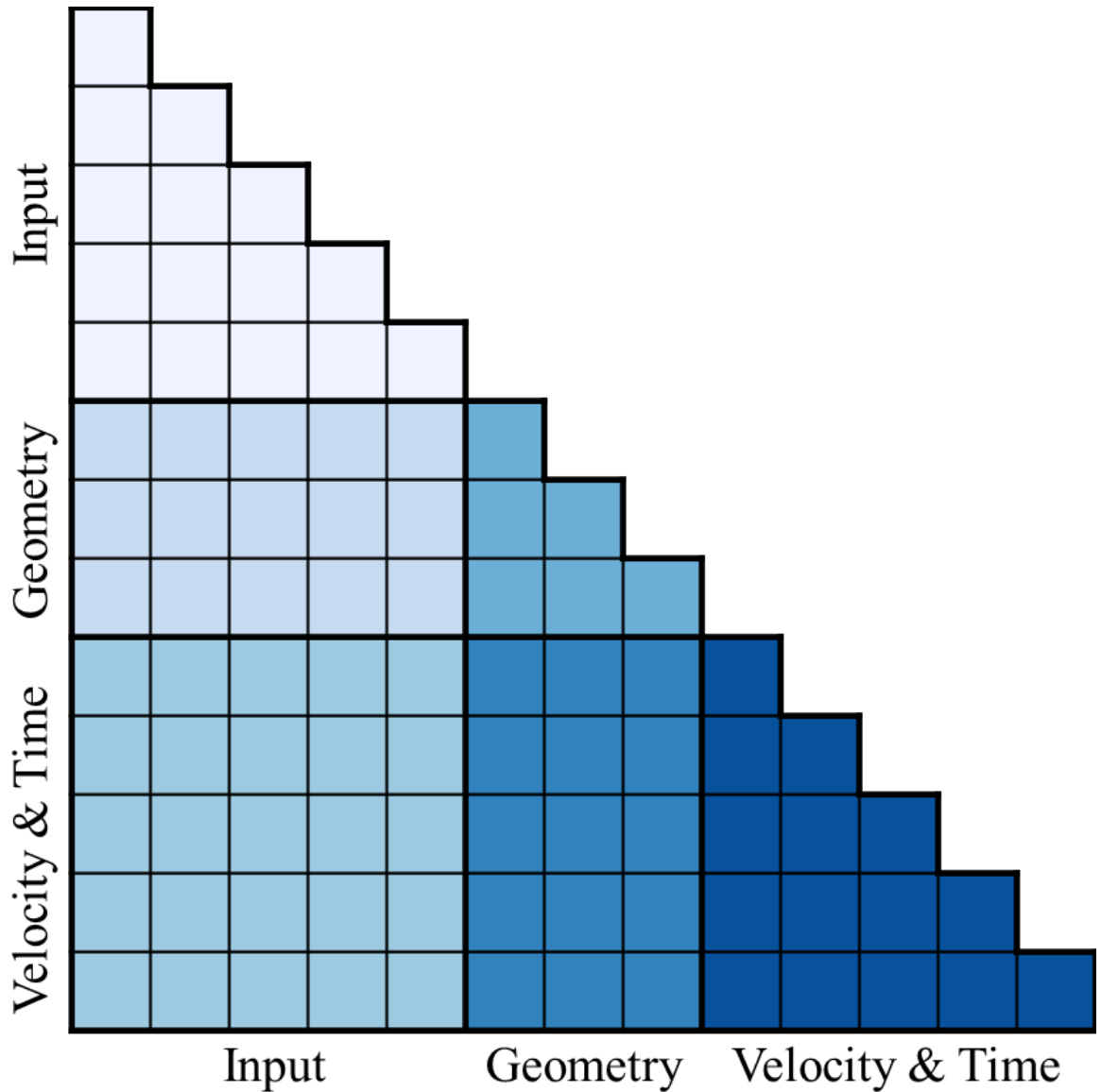


Figure A.1: For ease of display the results array is divided into six subplots, Figures A.2–A.6. The Input parameters consist of: M_{200_1} , M_{200_2} , z_1 , z_2 , and d_{proj} . The calculated Geometry parameters consist of: α , $d_{3\text{D}}$, and d_{max} . The calculated Velocity & Time parameters consist of: $v_{3\text{D}}(t_{\text{obs}})$, $v_{3\text{D}}(t_{\text{col}})$, TSC_0 , TSC_1 , and T .

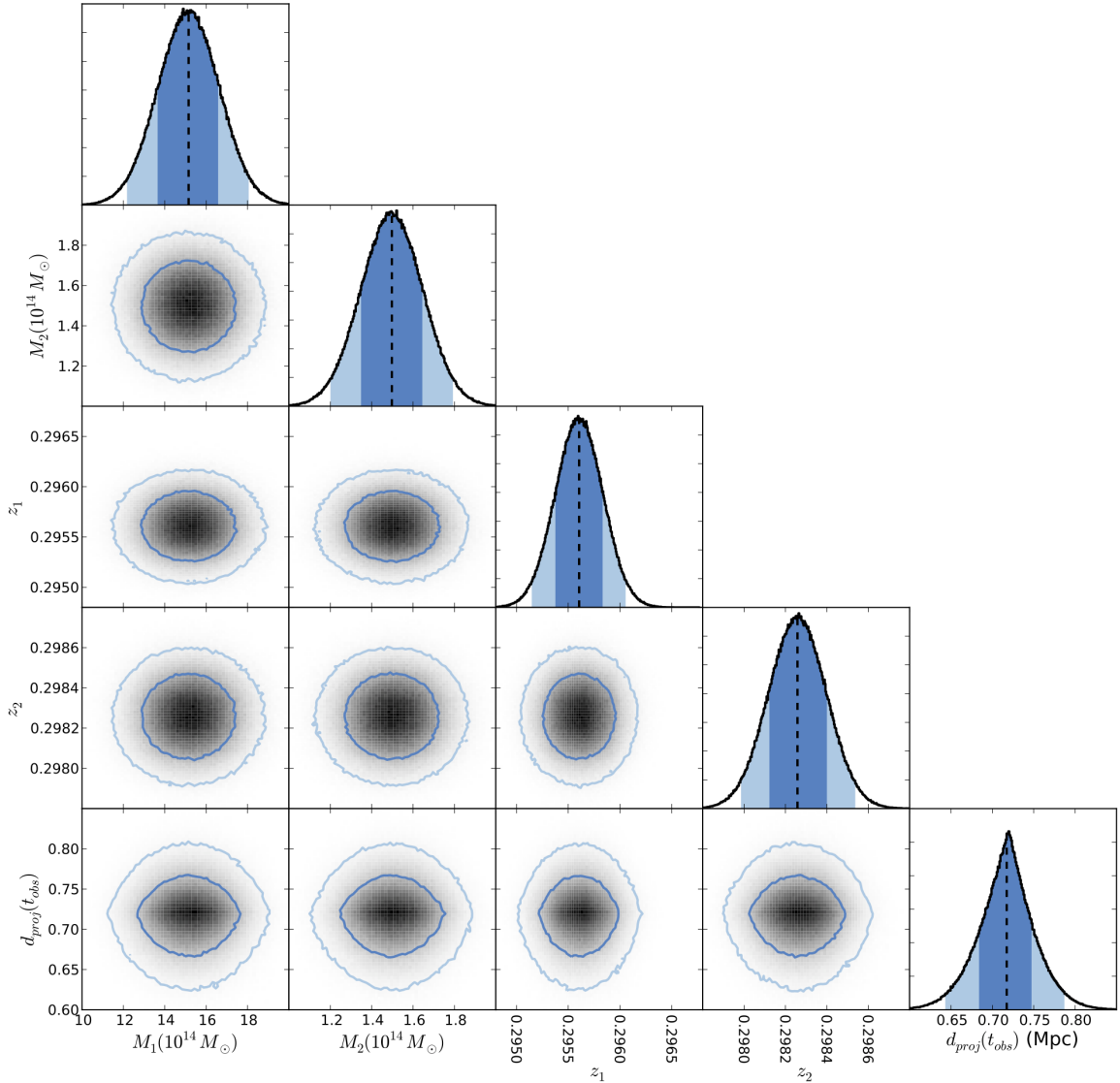


Figure A.2: Bullet Cluster marginalized *Input vs. Input* parameters result plots, for the case including the added temporal prior of §3.3.2.2. Dark and light blue colors correspond to 68% and 95% confidence intervals, respectively. The black dashed line is the biweight-statistic location [10].

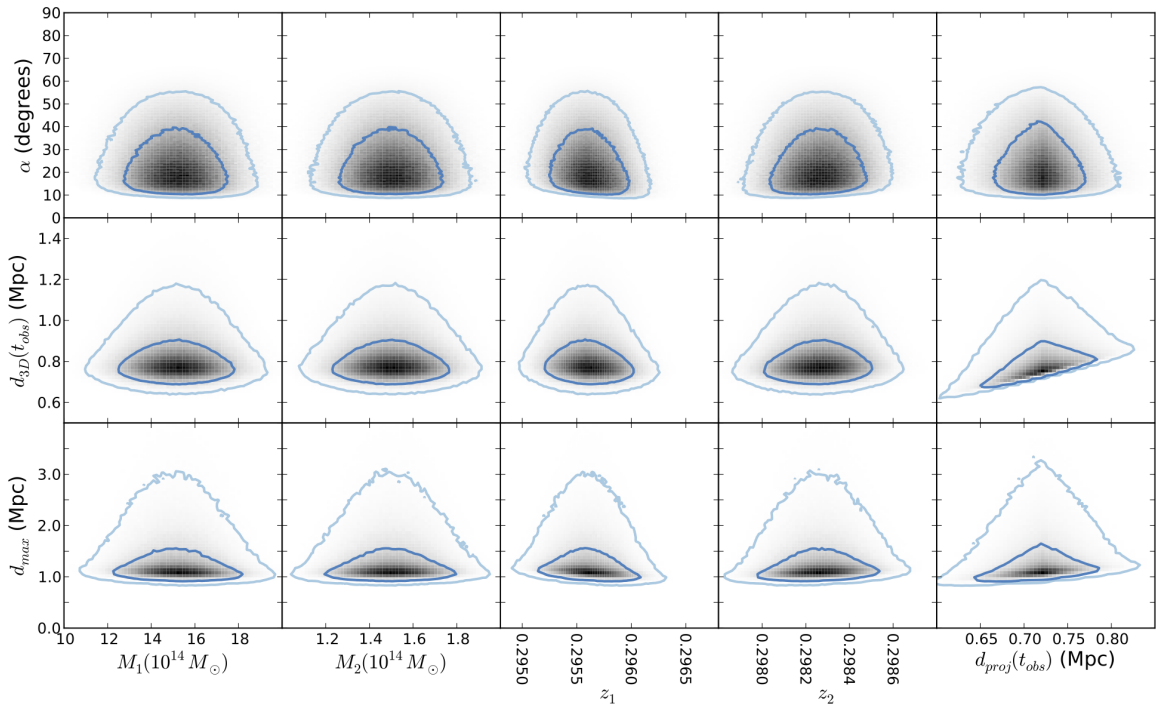


Figure A.3: Bullet Cluster marginalized *Input vs. Geometry* parameters result plots, for the case including the added temporal prior of §3.3.2.2. Dark and light blue colors correspond to 68% and 95% confidence intervals, respectively.

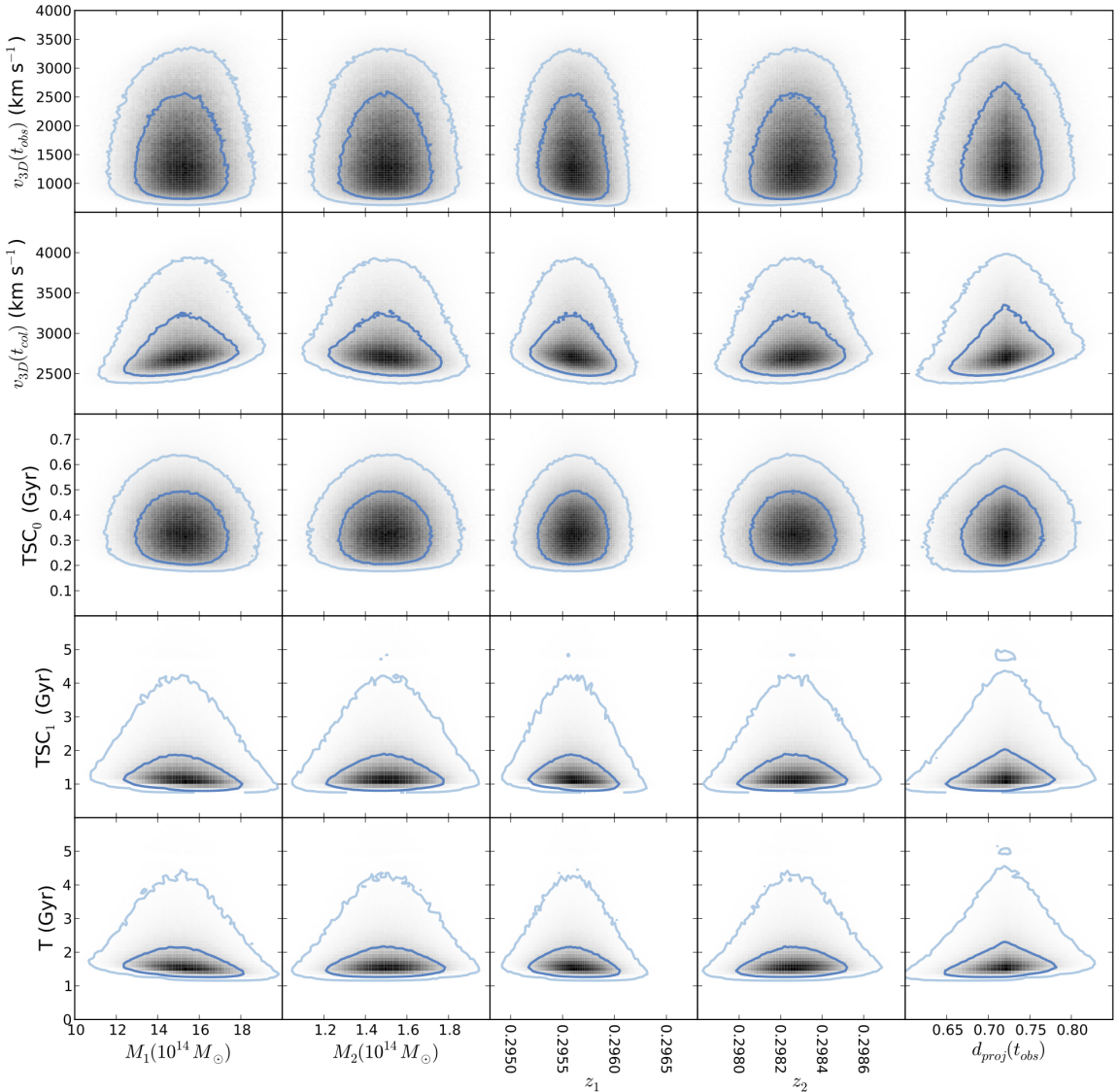


Figure A.4: Bullet Cluster marginalized *Input vs. Velocity & Time* parameters result plots, for the case including the added temporal prior of §3.3.2.2. Dark and light blue colors correspond to 68% and 95% confidence intervals, respectively.

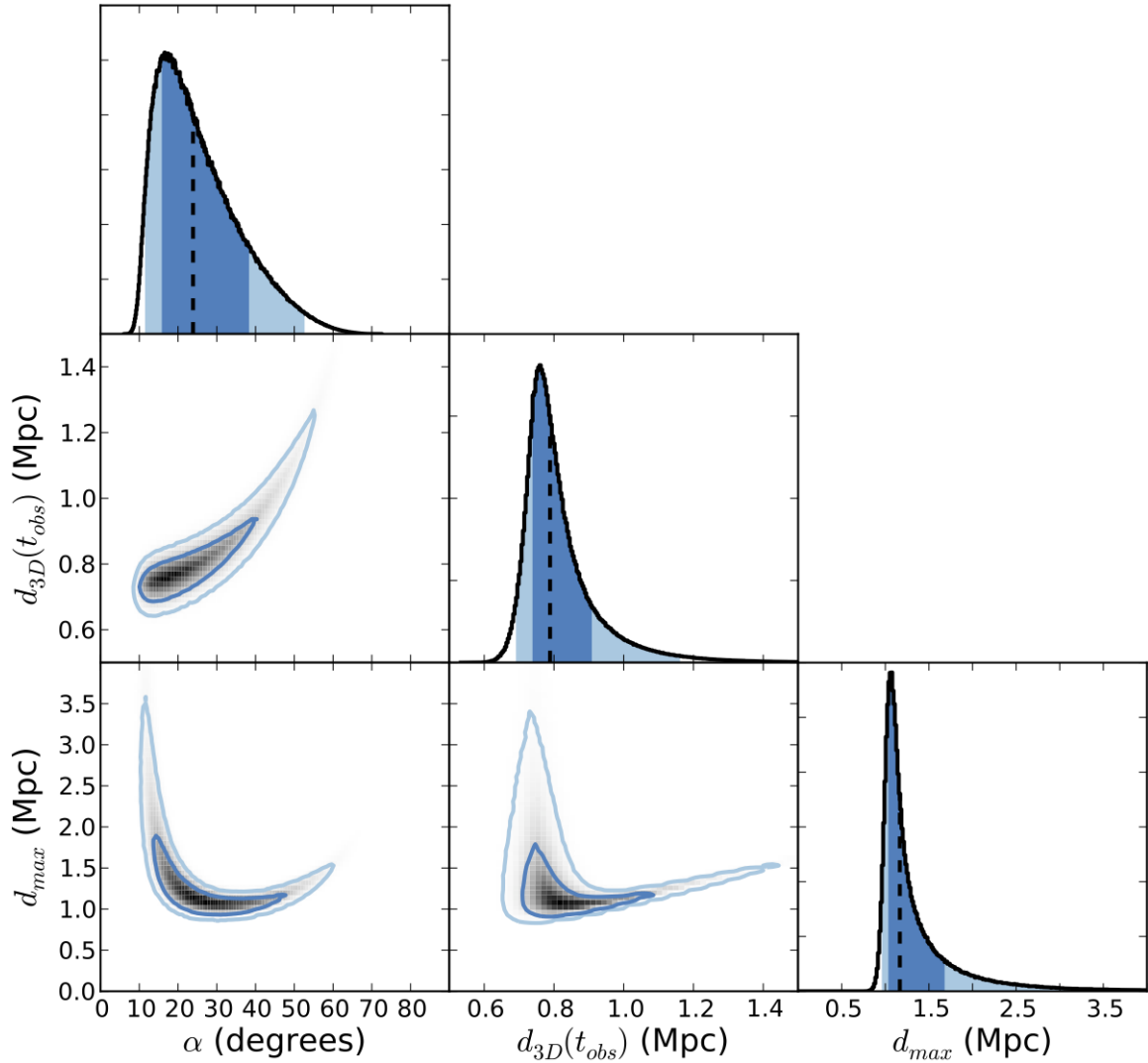


Figure A.5: Bullet Cluster marginalized *Geometry vs. Geometry* parameters result plots, for the case including the added temporal prior of §3.3.2.2. Dark and light blue colors correspond to 68% and 95% confidence intervals, respectively. The black dashed line is the biweight-statistic location [10].

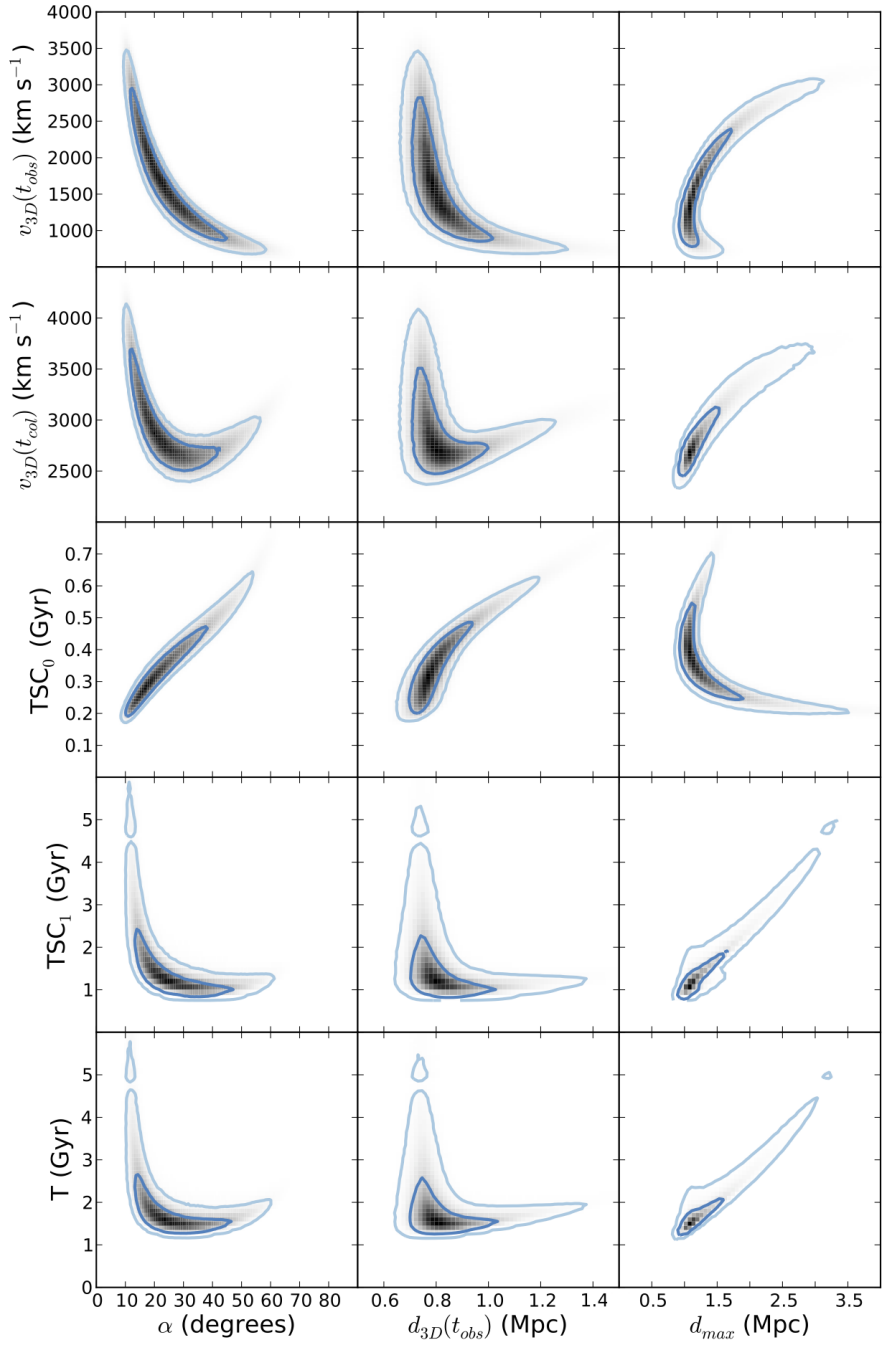


Figure A.6: Bullet Cluster marginalized *Geometry vs. Velocity & Time* parameters result plots, for the case including the added temporal prior of §3.3.2.2. Dark and light blue colors correspond to 68% and 95% confidence intervals, respectively.

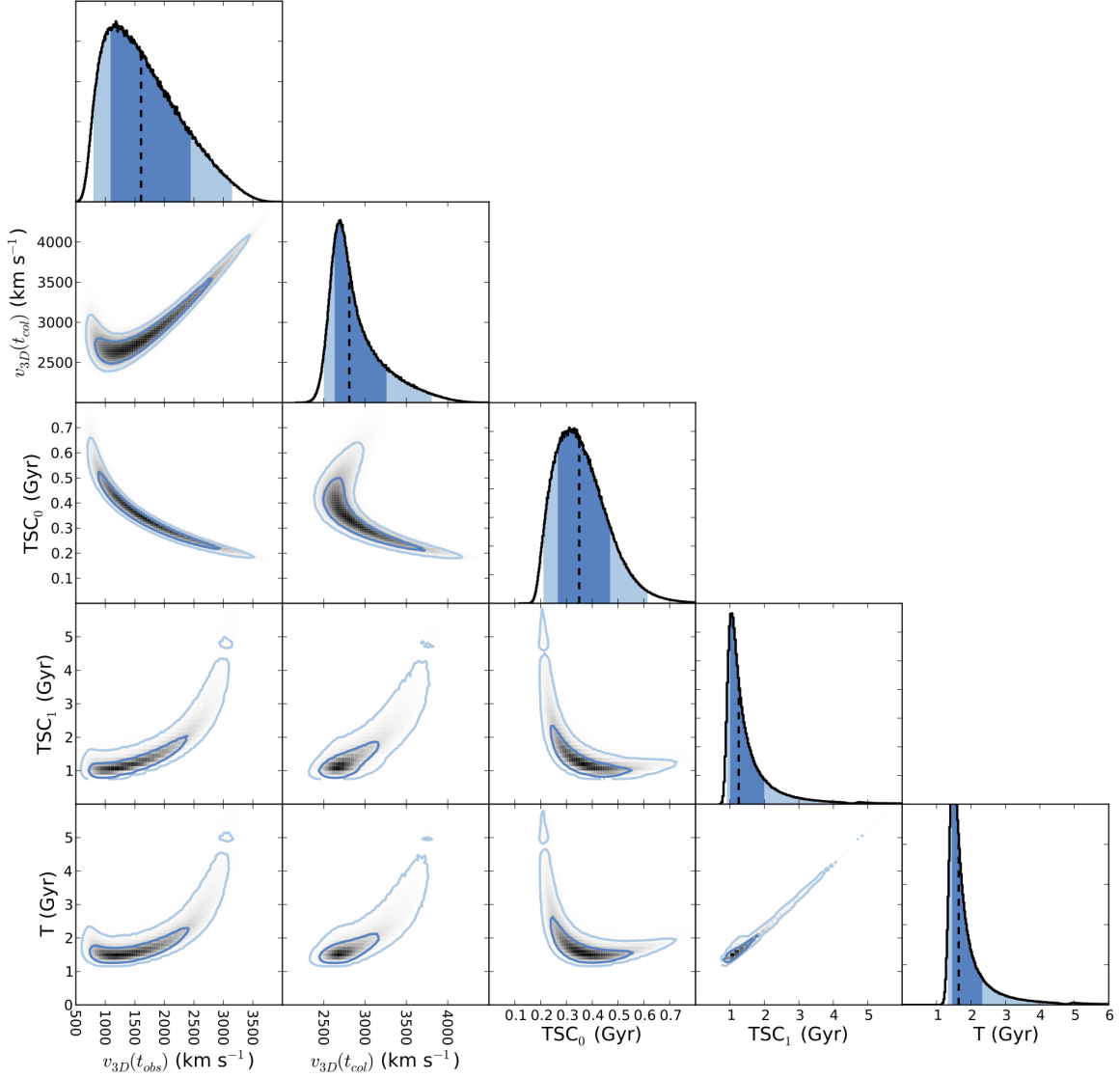


Figure A.7: Bullet Cluster marginalized *Velocity & Time vs. Velocity & Time* parameters result plots, for the case including the added temporal prior of §3.3.2.2. Dark and light blue colors correspond to 68% and 95% confidence intervals, respectively. The black dashed line is the biweight-statistic location [10].

A.4 Musket Ball Cluster Result Plots

This section contains the parameter results array plots for the Musket Ball Cluster. Similar to §A.3 the parameters are grouped in three categories (*Input*, *Geometry*, and *Velocity & Time*) resulting in a six subplot results array, see Figure A.1. The *Input* parameters consist of: M_{200_1} , M_{200_2} , z_1 , z_2 , and d_{proj} , where halo 1 refers to the “south” subcluster and halo 2 refers to the “north” subcluster. The calculated *Geometry* parameters consist of: α , d_{3D} , and d_{max} . The calculated Velocity & Time parameters consist of: $v_{3D}(t_{\text{obs}})$, $v_{3D}(t_{\text{col}})$, TSC_0 , TSC_1 , and T .

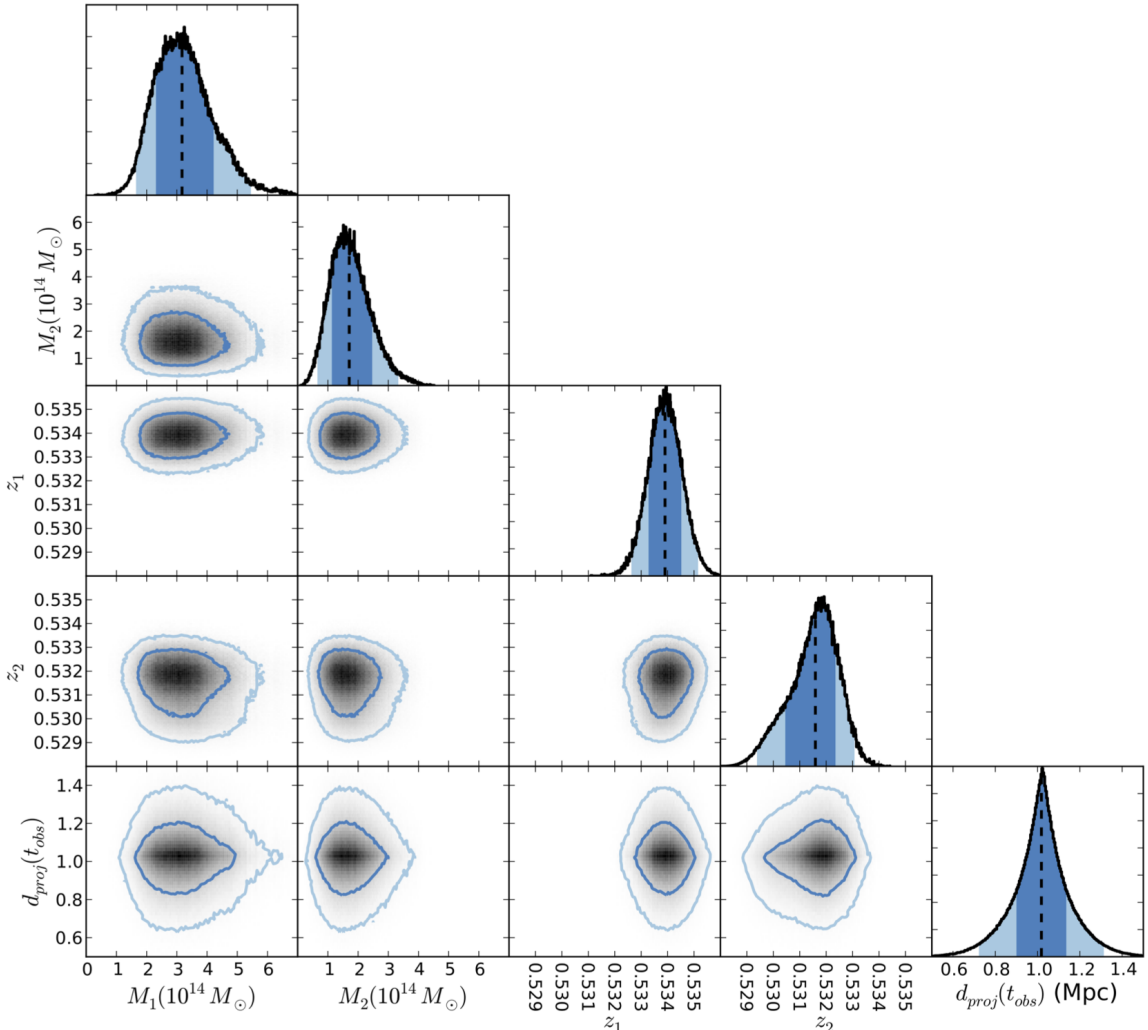


Figure A.8: Musket Ball Cluster marginalized *Input vs. Input* parameters result plots. Dark and light blue colors correspond to 68% and 95% confidence intervals, respectively. The black dashed line is the biweight-statistic location [10].

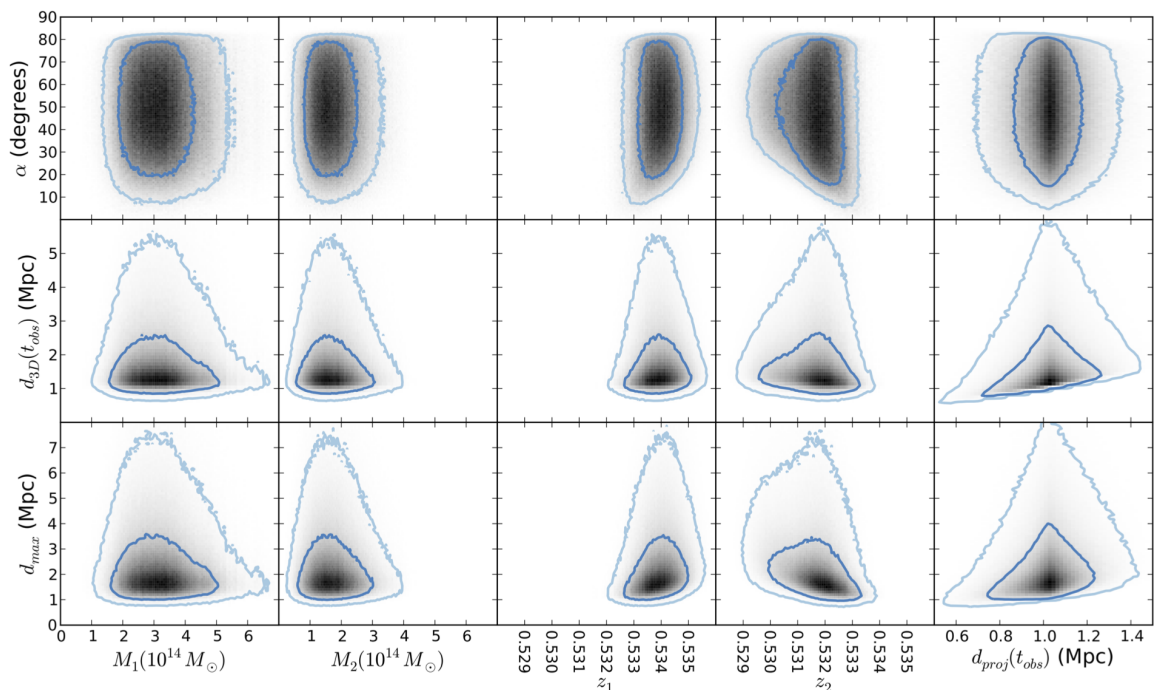


Figure A.9: Musket Ball Cluster marginalized *Input vs. Geometry* parameters result plots. Dark and light blue colors correspond to 68% and 95% confidence intervals, respectively.

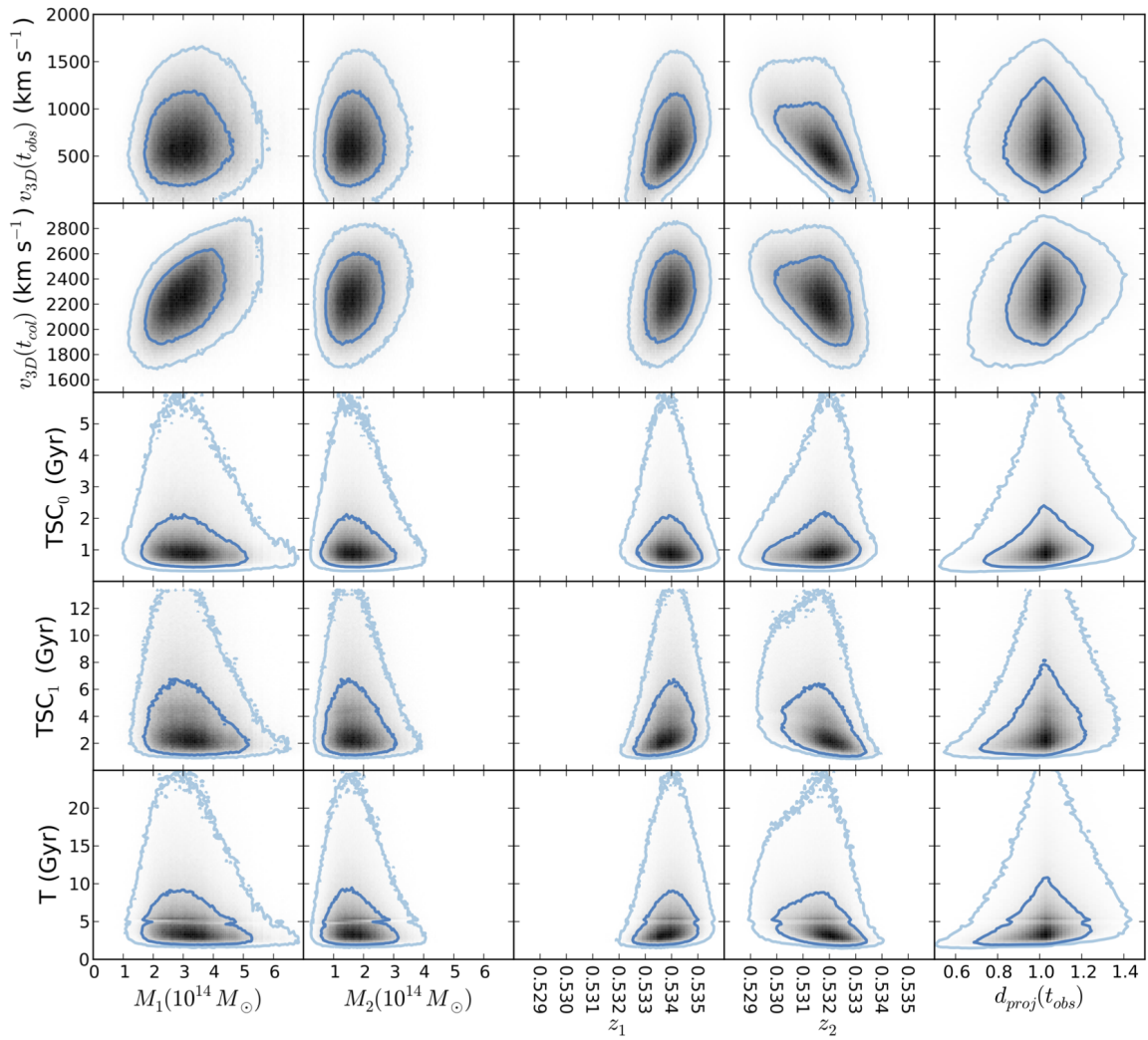


Figure A.10: Musket Ball Cluster marginalized *Input vs. Velocity & Time* parameters result plots. Dark and light blue colors correspond to 68% and 95% confidence intervals, respectively.

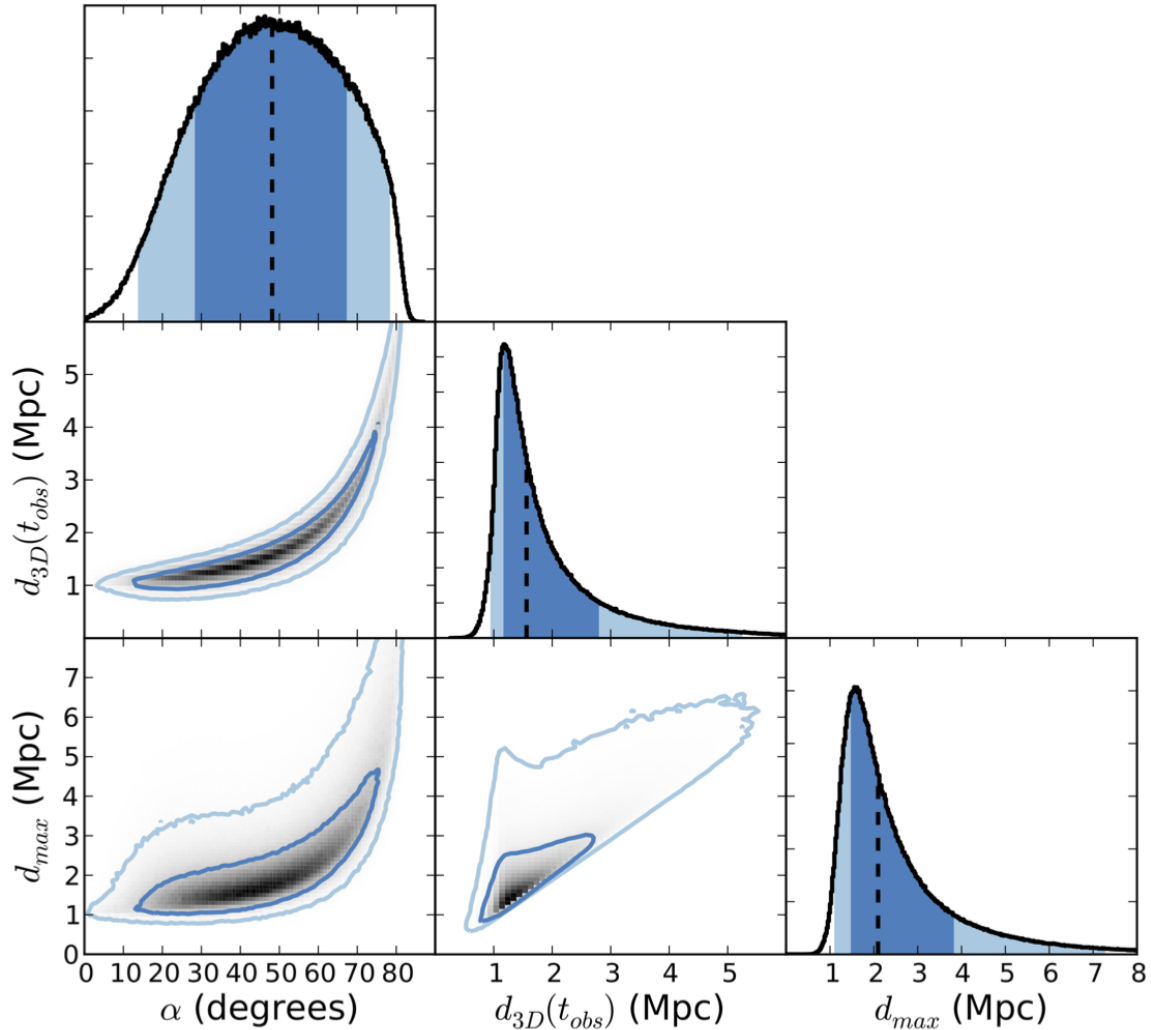


Figure A.11: Musket Ball Cluster marginalized *Geometry vs. Geometry* parameters result plots. Dark and light blue colors correspond to 68% and 95% confidence intervals, respectively. The black dashed line is the biweight-statistic location [10].

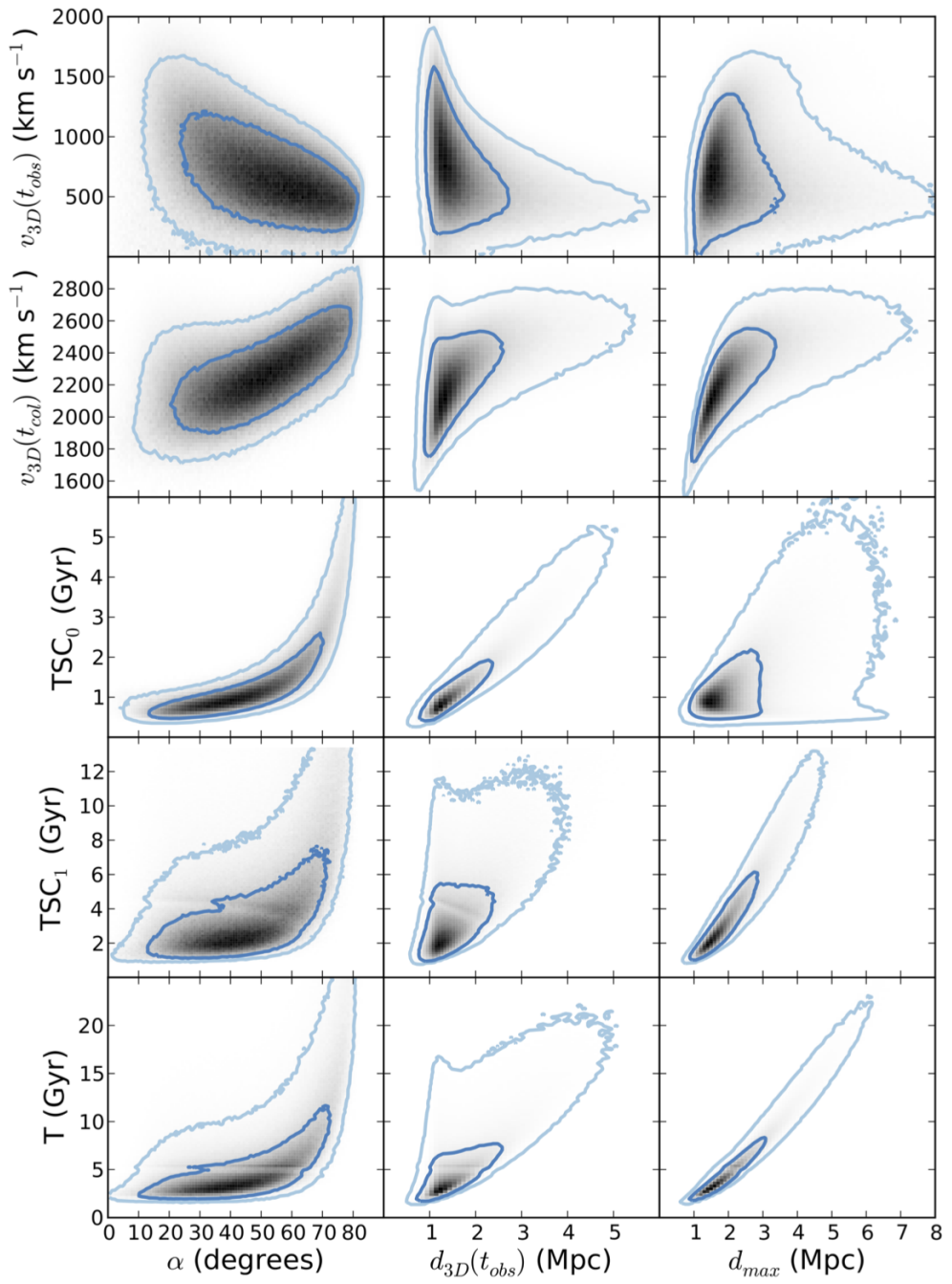


Figure A.12: Musket Ball Cluster marginalized *Geometry vs. Velocity & Time* parameters result plots. Dark and light blue colors correspond to 68% and 95% confidence intervals, respectively.

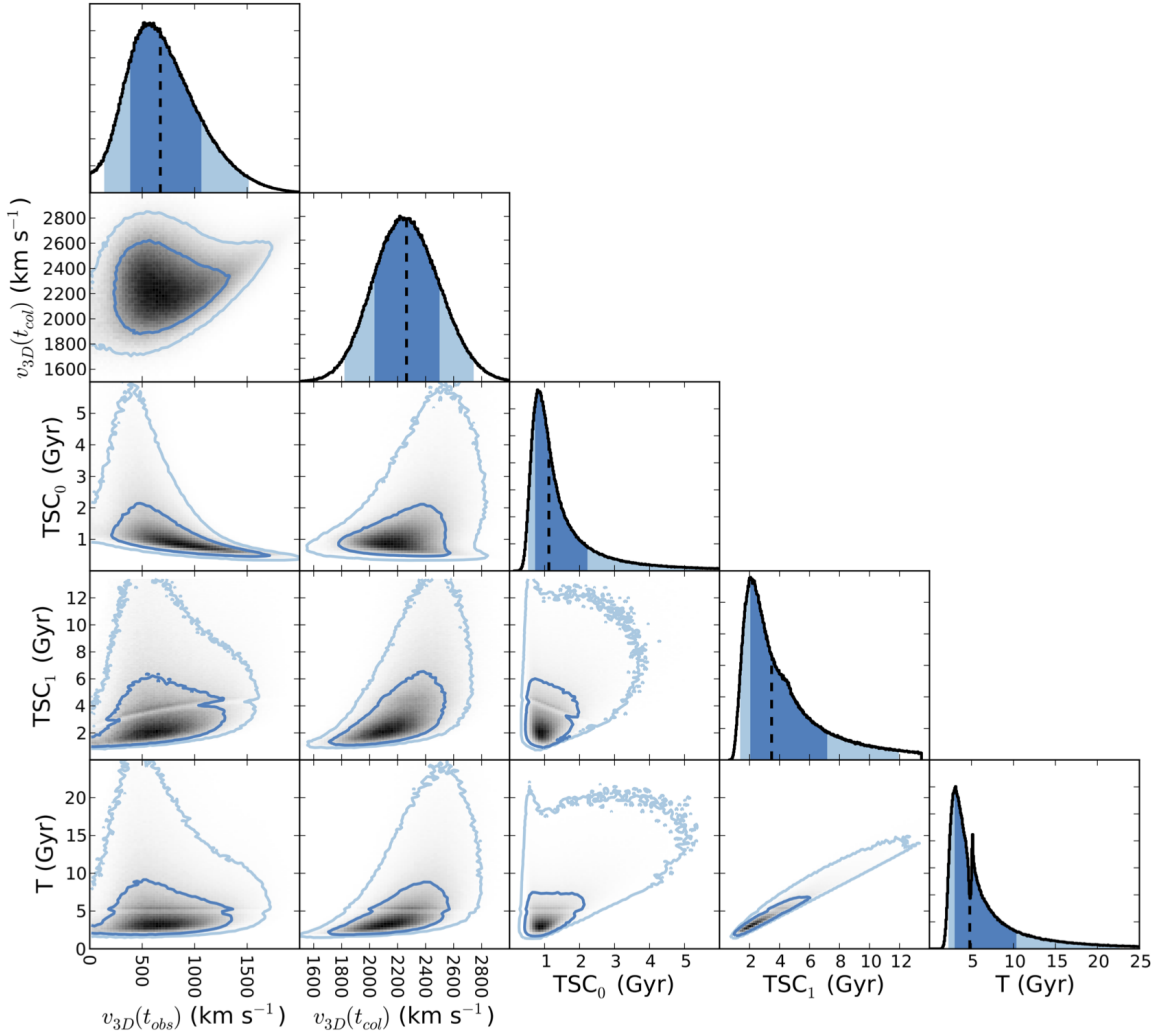


Figure A.13: Musket Ball Cluster marginalized *Velocity & Time vs. Velocity & Time* parameters result plots. Dark and light blue colors correspond to 68% and 95% confidence intervals, respectively. The black dashed line is the biweight-statistic location [10].

Appendix B

Fully Probabilistic Galaxy Cluster Membership Determination

B.1 Method

This membership determination method is rooted in the desire to treat both spectroscopic and photometric redshift samples in a consistent manner. This method slightly favors minimizing the Poisson noise while still trying to address the systematic contamination error. The basic approach is to assign a weight to each galaxy based on its probability of being a cluster member. This weight is defined as the inner product of the redshift probability density function (PDF) of a galaxy $p_i(z)$ and the redshift velocity dispersion (σ_{vdisp} assumed to be Gaussian) of the cluster at redshift z_{cluster} ,

$$w_i = \int_0^\infty p_i(z) \frac{1}{\sigma_{\text{vdisp}} \sqrt{2\pi}} e^{\frac{-(z-z_{\text{cluster}})^2}{2\sigma_{\text{vdisp}}^2}} dz. \quad (\text{B.1})$$

Since the redshift uncertainty of a spectroscopically observed galaxy with z_{spec_i} is $\ll \sigma_{\text{vdisp}}(1+z_{\text{cluster}})c^{-1}$, its redshift PDF can be treated as a delta-function and Equation B.1 reduces to

$$w_i = \frac{1}{\sigma_{\text{vdisp}} \sqrt{2\pi}} e^{\frac{-(z_{\text{spec}_i}-z_{\text{cluster}})^2}{2\sigma_{\text{vdisp}}^2}}. \quad (\text{B.2})$$

Under the assumption of Gaussian photometric redshift errors¹ ($\sigma_{z-\text{phot}_i} \approx \bar{\sigma}(1 + z_{\text{phot}_i})$; $\bar{\sigma}=0.07$ for the Musket Ball Cluster) Equation B.1 takes the form

$$w_i = \int_0^\infty \frac{1}{\sigma_{z-\text{phot}_i} \sqrt{2\pi}} e^{-\frac{(z-z_{\text{phot}_i})^2}{2\sigma_{z-\text{phot}_i}^2}} \frac{1}{\sigma_{\text{vdisp}} \sqrt{2\pi}} e^{-\frac{(z-z_{\text{cluster}})^2}{2\sigma_{\text{vdisp}}^2}} dz. \quad (\text{B.3})$$

When estimating the galaxy centroid these weights are simply used in conjunction with Equation 4.1. The bootstrap realizations used in the centroid uncertainty estimate are handled in a slightly different but equivalent manner. Using these weights we form a cumulative normalized weight distribution for all the galaxies with $R < 24$ and within a 9' by 9' region surrounding the Musket Ball Cluster (see Figure B.1). During the bootstrap sampling process a random number between 0 and 1 is drawn from a uniform distribution, where this random number intersects the weight distribution determines the randomly selected galaxy. Beyond this weighted draw with replacement the bootstrap uncertainty analysis is standard in all regards.

Comparing the galaxy redshift distribution of a random bootstrap realization with the redshift distribution of the parent population (Figure B.2) it is apparent that the fully probabilistic membership determination scheme still includes a large number of galaxies with photometric redshift estimates well outside the cluster redshift velocity dispersion ($z_{\text{cluster}} \pm \sigma_{\text{vdisp}}(1 + z_{\text{cluster}})c^{-1} \approx 0.53 \pm 0.004$). The reason for this is simply that the photometric redshift uncertainties are so large compared to all other pertinent redshift scales. Thus, galaxies that have the exact same photometric redshift as the cluster are not weighted dramatically more than galaxies with photometric redshift estimates well in front of or behind the cluster. Take for example two photometric redshift galaxies, one at the cluster redshift ($z = 0.53$) and one well behind the cluster at $z_{\text{phot}} = 0.79$. According to Equation B.3 the galaxy with $z_{\text{phot}} = 0.53$ will have a weight of 3.7 while the galaxy with $z_{\text{phot}} = 0.79$ will have a weight of 0.37. Since even in this small projected region around the Musket Ball Cluster the number of fore/background galaxies outnumber the cluster members, this probabilistic weighting scheme will always result in a significant amount of contamination. This is why George et al. [60] base their probability of cluster membership both on the

¹In reality there are a small fraction of galaxies, known as catastrophic outliers, that violate this assumption [see 137, for a detailed discussion]. For the case of DLS photometric redshifts the outlier fraction is $\lesssim 5\%$, thus they should not significantly violate the assumptions of this method.

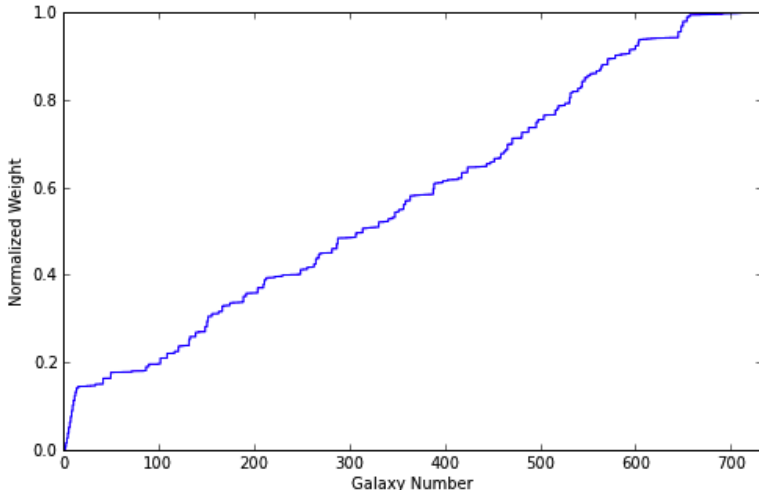


Figure B.1: The resulting cumulative weight distribution for all the galaxies with $R < 24$ and within a 9' by 9' region surrounding the Musket Ball Cluster. This distribution is used to perform a weighted random draw of cluster galaxies (e.g. the green distribution of Figure B.2) for the galaxy centroid bootstrap analysis. This distribution is determined by Equations B.1 and B.3. During the bootstrap sampling process a random number between 0 and 1 is drawn from a uniform distribution, where this random number intersects the weight distribution determines the randomly selected galaxy. Note that the catalog is sorted such that the spectroscopic members are first, thus the noticeably steeper slope for the early galaxy numbers.

expected distribution of the cluster members as well as the field. Such a method is worth considering for future work but is currently beyond the scope of this dissertation. Instead we use an empirically based method to determine our weighting scheme for cluster membership (see §4.2.4.2).

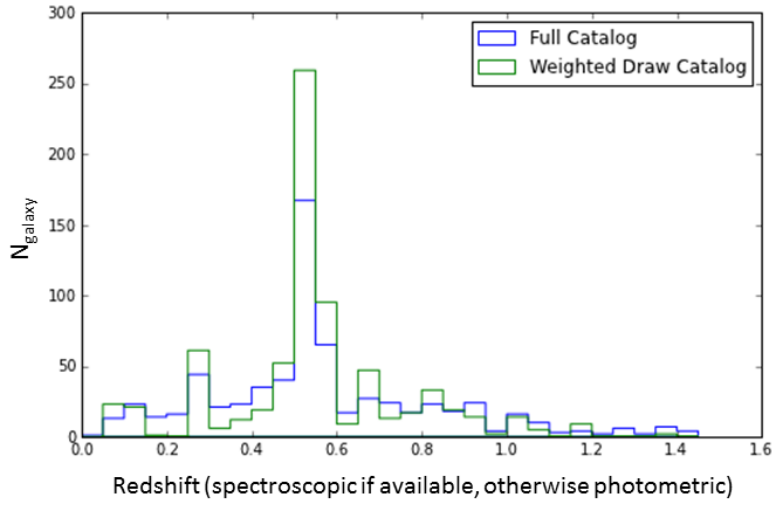


Figure B.2: The redshift (spectroscopic if available, otherwise photometric) distribution of all the galaxies in a $9' \times 9'$ area surrounding the Musket Ball Cluster with $R < 24$ (blue); and a single bootstrap sample (green) drawn from the fully probabilistic weighted distribution (Figure B.1). While the probabilistic scheme does work to increase the number of galaxies selected at the cluster redshift ($z = 0.53$) it still selects a disproportionate number of galaxies with photometric redshifts outside of the cluster redshift; see that in Figure 4.2 only 1 galaxy of our spectroscopic survey sample with $z_{\text{phot}} > 0.7$ is actually at the cluster redshift and only 1 galaxy with $z_{\text{phot}} < 0.43$ is at the cluster redshift.

REFERENCES

- [1] Ackerman, L., Buckley, M. R., Carroll, S. M., & Kamionkowski, M. 2009, Phys. Rev. D, 79, 023519, 0810.5126
- [2] Alcock, C. et al. 2000, ApJ, 542, 281, arXiv:astro-ph/0001272
- [3] Angus, G. W., & McGaugh, S. S. 2008, MNRAS, 383, 417, 0704.0381
- [4] Aragón-Calvo, M. A., van de Weygaert, R., & Jones, B. J. T. 2010, MNRAS, 408, 2163, 1007.0742
- [5] Arkani-Hamed, N., Finkbeiner, D. P., Slatyer, T. R., & Weiner, N. 2009, Phys. Rev. D, 79, 015014, 0810.0713
- [6] Arnaud, K. A. 1996, in Astronomical Society of the Pacific Conference Series, Vol. 101, Astronomical Data Analysis Software and Systems V, ed. G. H. Jacoby & J. Barnes, 17
- [7] Barrena, R., Biviano, A., Ramella, M., Falco, E. E., & Seitz, S. 2002, A&A, 386, 816, arXiv:astro-ph/0202323
- [8] Barrena, R., Girardi, M., Boschin, W., & Dasí, M. 2009, A&A, 503, 357, 0905.3011
- [9] Beers, T. C., Flynn, K., & Gebhardt, K. 1990, AJ, 100, 32
- [10] Beers, T. C., Geller, M. J., & Huchra, J. P. 1982, ApJ, 257, 23
- [11] Benítez, N. 2000, ApJ, 536, 571, arXiv:astro-ph/9811189
- [12] Berlind, A. A. et al. 2006, ApJS, 167, 1, arXiv:astro-ph/0601346
- [13] Bertin, E. 2006, in Astronomical Society of the Pacific Conference Series, Vol. 351, Astronomical Data Analysis Software and Systems XV, ed. C. Gabriel, C. Arviset, D. Ponz, & S. Enrique, 112
- [14] Bertin, E., Mellier, Y., Radovich, M., Missonnier, G., Didelon, P., & Morin, B. 2002, in Astronomical Society of the Pacific Conference Series, Vol. 281, Astronomical Data Analysis Software and Systems XI, ed. D. A. Bohlander, D. Durand, & T. H. Handley, 228
- [15] Bonafede, A. et al. 2012, MNRAS, 426, 40, 1206.6102
- [16] Boschin, W., Girardi, M., Barrena, R., & Nonino, M. 2012, A&A, 540, A43, 1203.1473
- [17] Bourdin, H. et al. 2011, A&A, 527, A21, 1011.3154
- [18] Boylan-Kolchin, M., Bullock, J. S., & Kaplinghat, M. 2012, MNRAS, 422, 1203, 1111.2048

- [19] Bradač, M., Allen, S. W., Treu, T., Ebeling, H., Massey, R., Morris, R. G., von der Linden, A., & Applegate, D. 2008, ApJ, 687, 959, 0806.2320
- [20] Bradač, M. et al. 2006, ApJ, 652, 937, arXiv:astro-ph/0608408
- [21] Bullock, J. S. 2010, ArXiv e-prints, 1009.4505
- [22] Bullock, J. S., Dekel, A., Kolatt, T. S., Kravtsov, A. V., Klypin, A. A., Porciani, C., & Primack, J. R. 2001, ApJ, 555, 240, arXiv:astro-ph/0011001
- [23] Carlberg, R. G., Yee, H. K. C., Morris, S. L., Lin, H., Hall, P. B., Patton, D. R., Sawicki, M., & Shepherd, C. W. 2001, ApJ, 552, 427, arXiv:astro-ph/0008201
- [24] Carlson, E. D., Machacek, M. E., & Hall, L. J. 1992, ApJ, 398, 43
- [25] Choi, A. 2011, PhD thesis, University of California, Davis
- [26] Choi, A., Tyson, J. A., Morrison, C. B., Jee, M. J., Schmidt, S. J., Margoniner, V. E., & Wittman, D. M. 2012, ApJ, 759, 101, 1208.3904
- [27] Chung, S. M., Gonzalez, A. H., Clowe, D., Markevitch, M., & Zaritsky, D. 2010, ApJ, 725, 1536, 1005.3847
- [28] Chung, S. M., Gonzalez, A. H., Clowe, D., Zaritsky, D., Markevitch, M., & Jones, C. 2009, ApJ, 691, 963, 0810.1052
- [29] Clowe, D., Bradač, M., Gonzalez, A. H., Markevitch, M., Randall, S. W., Jones, C., & Zaritsky, D. 2006, ApJ, 648, L109, arXiv:astro-ph/0608407
- [30] Clowe, D., Gonzalez, A., & Markevitch, M. 2004, ApJ, 604, 596, arXiv:astro-ph/0312273
- [31] Coe, D., Benítez, N., Sánchez, S. F., Jee, M., Bouwens, R., & Ford, H. 2006, AJ, 132, 926, arXiv:astro-ph/0605262
- [32] Coil, A. L. et al. 2011, ApJ, 741, 8, 1011.4307
- [33] Colín, P., Avila-Reese, V., Valenzuela, O., & Firmani, C. 2002, ApJ, 581, 777, arXiv:astro-ph/0205322
- [34] Cook, R. I., & Dell'Antonio, I. P. 2012, ApJ, 750, 153
- [35] Courbin, F., & Minniti, D., eds. 2002, Lecture Notes in Physics, Berlin Springer Verlag, Vol. 608, Gravitational Lensing: An Astrophysical Tool
- [36] Dahle, H. 2000, in The NOT in the 2000's, ed. N. Bergvall, L. O. Takalo, & V. Piironen, 45, arXiv:astro-ph/0009393
- [37] Dalcanton, J. J., & Hogan, C. J. 2001, ApJ, 561, 35, arXiv:astro-ph/0004381

- [38] Davé, R., Spergel, D. N., Steinhardt, P. J., & Wandelt, B. D. 2001, ApJ, 547, 574, arXiv:astro-ph/0006218
- [39] Davis, M. et al. 2003, in Society of Photo-Optical Instrumentation Engineers (SPIE) Conference Series, Vol. 4834, Society of Photo-Optical Instrumentation Engineers (SPIE) Conference Series, ed. P. Guhathakurta, 161–172, arXiv:astro-ph/0209419
- [40] Dawson, W. A. 2013, ApJ, 772, 131, 1210.0014
- [41] Dawson, W. A. et al. 2012, ApJ, 747, L42, 1110.4391
- [42] de Laix, A. A., Scherrer, R. J., & Schaefer, R. K. 1995, ApJ, 452, 495, arXiv:astro-ph/9502087
- [43] Diaferio, A., Schindler, S., & Dolag, K. 2008, Space Sci. Rev., 134, 7, 0801.0968
- [44] Dietrich, J. P., Böhnert, A., Lombardi, M., Hilbert, S., & Hartlap, J. 2012, MNRAS, 419, 3547, 1103.4607
- [45] Dietrich, J. P., Werner, N., Clowe, D., Finoguenov, A., Kitching, T., Miller, L., & Simionescu, A. 2012, Nature, 487, 202, 1207.0809
- [46] Duffy, A. R., Schaye, J., Kay, S. T., & Dalla Vecchia, C. 2008, MNRAS, 390, L64, 0804.2486
- [47] Ensslin, T. A., Biermann, P. L., Klein, U., & Kohle, S. 1998, A&A, 332, 395, arXiv:astro-ph/9712293
- [48] Evrard, A. E. et al. 2008, ApJ, 672, 122, arXiv:astro-ph/0702241
- [49] Fahlman, G., Kaiser, N., Squires, G., & Woods, D. 1994, ApJ, 437, 56, arXiv:astro-ph/9402017
- [50] Farrar, G. R., & Rosen, R. A. 2007, Physical Review Letters, 98, 171302, arXiv:astro-ph/0610298
- [51] Feng, J. L., Kaplinghat, M., & Yu, H.-B. 2010, Physical Review Letters, 104, 151301, 0911.0422
- [52] Ferrari, C., Benoist, C., Maurogordato, S., Cappi, A., & Slezak, E. 2005, A&A, 430, 19, arXiv:astro-ph/0409072
- [53] Fischer, P., & Tyson, J. A. 1997, AJ, 114, 14, arXiv:astro-ph/9703189
- [54] Forero-Romero, J. E., Gottlöber, S., & Yepes, G. 2010, ApJ, 725, 598, 1007.3902
- [55] Gal, R. R., Lemaux, B. C., Lubin, L. M., Kocevski, D., & Squires, G. K. 2008, ApJ, 684, 933, 0803.3842
- [56] Gavazzi, G., Garilli, B., & Boselli, A. 1990, A&AS, 83, 399

- [57] Geller, M. J., Dell'Antonio, I. P., Kurtz, M. J., Ramella, M., Fabricant, D. G., Caldwell, N., Tyson, J. A., & Wittman, D. 2005, ApJ, 635, L125, arXiv:astro-ph/0510351
- [58] Gelman, A., & Rubin, D. B. 1992, Statistical Science, 7, 457
- [59] George, M. R. et al. 2012, ApJ, 757, 2, 1205.4262
- [60] ——. 2011, ApJ, 742, 125, 1109.6040
- [61] Giavalisco, M. et al. 2004, ApJ, 600, L93, arXiv:astro-ph/0309105
- [62] Girardi, M., Barrena, R., Boschin, W., & Ellingson, E. 2008, A&A, 491, 379, 0809.3139
- [63] Gladders, M. D., & Yee, H. K. C. 2000, AJ, 120, 2148, arXiv:astro-ph/0004092
- [64] Gnedin, O. Y., & Ostriker, J. P. 2001, ApJ, 561, 61, arXiv:astro-ph/0010436
- [65] Gómez, P. L., Hughes, J. P., & Birkinshaw, M. 2000, ApJ, 540, 726, arXiv:astro-ph/0004263
- [66] Gómez, P. L. et al. 2012, AJ, 144, 79
- [67] Gonzalez, A. H., Zaritsky, D., Simard, L., Clowe, D., & White, S. D. M. 2002, ApJ, 579, 577, arXiv:astro-ph/0207243
- [68] Halverson, N. W. et al. 2009, ApJ, 701, 42, 0807.4208
- [69] Hao, J. et al. 2010, ApJS, 191, 254, 1010.5503
- [70] Hennawi, J. F., & Ostriker, J. P. 2002, ApJ, 572, 41, arXiv:astro-ph/0108203
- [71] Hennawi, J. F., & Spergel, D. N. 2005, ApJ, 624, 59, arXiv:astro-ph/0404349
- [72] Hincks, A. D. et al. 2010, ApJS, 191, 423, 0907.0461
- [73] Hogan, C. J., & Dalcanton, J. J. 2000, Phys. Rev. D, 62, 063511, arXiv:astro-ph/0002330
- [74] Hwang, H. S., & Lee, M. G. 2009, MNRAS, 397, 2111, 0905.2991
- [75] Ilbert, O. et al. 2006, A&A, 457, 841, arXiv:astro-ph/0603217
- [76] Jee, M. J., Blakeslee, J. P., Sirianni, M., Martel, A. R., White, R. L., & Ford, H. C. 2007, PASP, 119, 1403, 0710.5560
- [77] Jee, M. J. et al. 2011, ApJ, 737, 59, 1105.3186
- [78] Jee, M. J., & Tyson, J. A. 2009, ApJ, 691, 1337, 0810.0709
- [79] Kahlhoefer, F., Schmidt-Hoberg, K., Frandsen, M. T., & Sarkar, S. 2013, ArXiv e-prints, 1308.3419

- [80] Kahn, F. D., & Woltjer, L. 1959, ApJ, 130, 705
- [81] Kalberla, P. M. W., Burton, W. B., Hartmann, D., Arnal, E. M., Bajaja, E., Morras, R., & Pöppel, W. G. L. 2005, A&A, 440, 775, arXiv:astro-ph/0504140
- [82] Klypin, A., Kravtsov, A. V., Valenzuela, O., & Prada, F. 1999, ApJ, 522, 82, arXiv:astro-ph/9901240
- [83] Kochanek, C. S., & White, M. 2000, ApJ, 543, 514, arXiv:astro-ph/0003483
- [84] Koester, B. P. et al. 2007, ApJ, 660, 239, arXiv:astro-ph/0701265
- [85] Kuzio de Naray, R., McGaugh, S. S., & de Blok, W. J. G. 2008, ApJ, 676, 920, 0712.0860
- [86] Lee, J., & Komatsu, E. 2010, ApJ, 718, 60, 1003.0939
- [87] Lemaux, B. C. et al. 2009, ApJ, 700, 20, 0905.2233
- [88] Lynds, R., & Petrosian, V. 1989, ApJ, 336, 1
- [89] Macciò, A. V., Paduroiu, S., Anderhalden, D., Schneider, A., & Moore, B. 2012, MNRAS, 424, 1105, 1202.1282
- [90] Machacek, M. E. 1994, ApJ, 431, 41
- [91] Mahdavi, A., Hoekstra, H., Babul, A., Balam, D. D., & Capak, P. L. 2007, ApJ, 668, 806, 0706.3048
- [92] Markevitch, M. 2006, in ESA Special Publication, Vol. 604, The X-ray Universe 2005, ed. A. Wilson, 723, arXiv:astro-ph/0511345
- [93] Markevitch, M., Gonzalez, A. H., Clowe, D., Vikhlinin, A., Forman, W., Jones, C., Murray, S., & Tucker, W. 2004, ApJ, 606, 819, arXiv:astro-ph/0309303
- [94] Markevitch, M., Gonzalez, A. H., David, L., Vikhlinin, A., Murray, S., Forman, W., Jones, C., & Tucker, W. 2002, ApJ, 567, L27, arXiv:astro-ph/0110468
- [95] Mastropietro, C., & Burkert, A. 2008, MNRAS, 389, 967, 0711.0967
- [96] Mellier, Y. 1999, ARA&A, 37, 127, arXiv:astro-ph/9812172
- [97] Menanteau, F. et al. 2012, ApJ, 748, 7, 1109.0953
- [98] Meneghetti, M., Yoshida, N., Bartelmann, M., Moscardini, L., Springel, V., Tormen, G., & White, S. D. M. 2001, MNRAS, 325, 435, arXiv:astro-ph/0011405
- [99] Merritt, D., & Tremblay, B. 1994, AJ, 108, 514
- [100] Merten, J. et al. 2011, MNRAS, 417, 333, 1103.2772

- [101] Meylan, G., Jetzer, P., North, P., Schneider, P., Kochanek, C. S., & Wambsganss, J., eds. 2006, Gravitational Lensing: Strong, Weak and Micro, arXiv:astro-ph/0407232
- [102] Miller, N. A., & Owen, F. N. 2003, AJ, 125, 2427, arXiv:astro-ph/0302061
- [103] Milosavljević, M., Koda, J., Nagai, D., Nakar, E., & Shapiro, P. R. 2007, ApJ, 661, L131, arXiv:astro-ph/0703199
- [104] Miralda-Escudé, J. 2002, ApJ, 564, 60
- [105] Moore, B., Ghigna, S., Governato, F., Lake, G., Quinn, T., Stadel, J., & Tozzi, P. 1999, ApJ, 524, L19, arXiv:astro-ph/9907411
- [106] Mroczkowski, T. et al. 2012, ArXiv e-prints, 1205.0052
- [107] Muchovej, S. et al. 2011, ApJ, 732, 28, 1012.1610
- [108] Navarro, J. F., Frenk, C. S., & White, S. D. M. 1996, ApJ, 462, 563, arXiv:astro-ph/9508025
- [109] Newman, A. B., Treu, T., Ellis, R. S., & Sand, D. J. 2013, ApJ, 765, 25, 1209.1392
- [110] Newman, A. B., Treu, T., Ellis, R. S., Sand, D. J., Nipoti, C., Richard, J., & Jullo, E. 2013, ApJ, 765, 24, 1209.1391
- [111] Newman, J. A. et al. 2012, ArXiv e-prints, 1203.3192
- [112] Noh, Y., & Cohn, J. D. 2011, MNRAS, 413, 301, 1011.1000
- [113] Nusser, A. 2008, MNRAS, 384, 343, 0709.3572
- [114] Nuza, S. E., Hoeft, M., van Weeren, R. J., Gottlöber, S., & Yepes, G. 2012, MNRAS, 420, 2006, 1111.1721
- [115] Oh, S.-H., Brook, C., Governato, F., Brinks, E., Mayer, L., de Blok, W. J. G., Brooks, A., & Walter, F. 2011, AJ, 142, 24, 1011.2777
- [116] Okabe, N., Bourdin, H., Mazzotta, P., & Maurogordato, S. 2011, ApJ, 741, 116, 1107.0004
- [117] Ouchi, M. et al. 2004, ApJ, 611, 660, arXiv:astro-ph/0309655
- [118] Owen, F. N., Ledlow, M. J., Keel, W. C., Wang, Q. D., & Morrison, G. E. 2005, AJ, 129, 31, arXiv:astro-ph/0410340
- [119] Peebles, P. J. E. 1993, Principles of Physical Cosmology (Princeton University Press)
- [120] Peter, A. H. G. 2012, ArXiv e-prints, 1201.3942
- [121] Peter, A. H. G., Rocha, M., Bullock, J. S., & Kaplinghat, M. 2013, MNRAS, 430, 105, 1208.3026

- [122] Planck Collaboration et al. 2013, ArXiv e-prints, 1303.5076
- [123] Poggianti, B. M., Bridges, T. J., Komiyama, Y., Yagi, M., Carter, D., Mobasher, B., Okamura, S., & Kashikawa, N. 2004, ApJ, 601, 197, arXiv:astro-ph/0309449
- [124] Poole, G. B., Fardal, M. A., Babul, A., McCarthy, I. G., Quinn, T., & Wadsley, J. 2006, MNRAS, 373, 881, arXiv:astro-ph/0608560
- [125] Pospelov, M., Ritz, A., & Voloshin, M. 2008, Physics Letters B, 662, 53, 0711.4866
- [126] Ragozzine, B., Clowe, D., Markevitch, M., Gonzalez, A. H., & Bradač, M. 2012, ApJ, 744, 94, 1111.4983
- [127] Randall, S. W., Markevitch, M., Clowe, D., Gonzalez, A. H., & Bradač, M. 2008, ApJ, 679, 1173, 0704.0261
- [128] Randall, S. W., Sarazin, C. L., & Ricker, P. M. 2002, ApJ, 577, 579, arXiv:astro-ph/0206161
- [129] Ricker, P. M., & Sarazin, C. L. 2001, ApJ, 561, 621, arXiv:astro-ph/0107210
- [130] Rocha, M., Peter, A. H. G., Bullock, J. S., Kaplinghat, M., Garrison-Kimmel, S., Oñorbe, J., & Moustakas, L. A. 2013, MNRAS, 430, 81, 1208.3025
- [131] Rubin, V. C., & Ford, Jr., W. K. 1970, ApJ, 159, 379
- [132] Ruhl, J. et al. 2004, in Society of Photo-Optical Instrumentation Engineers (SPIE) Conference Series, Vol. 5498, Society of Photo-Optical Instrumentation Engineers (SPIE) Conference Series, ed. C. M. Bradford, P. A. R. Ade, J. E. Aguirre, J. J. Bock, M. Dragovan, L. Duband, L. Earle, J. Glenn, H. Matsuhara, B. J. Naylor, H. T. Nguyen, M. Yun, & J. Zmuidzinas, 11–29, arXiv:astro-ph/0411122
- [133] Russell, H. R. et al. 2011, MNRAS, 417, L1, 1105.0435
- [134] Sanders, R. H., & McGaugh, S. S. 2002, ARA&A, 40, 263, arXiv:astro-ph/0204521
- [135] Sanderson, A. J. R., Edge, A. C., & Smith, G. P. 2009, MNRAS, 398, 1698, 0906.1808
- [136] Schindler, S., & Mueller, E. 1993, A&A, 272, 137
- [137] Schmidt, S. J., & Thorman, P. 2013, MNRAS, 431, 2766, 1211.3245
- [138] Sehgal, N., Hughes, J. P., Wittman, D., Margoniner, V., Tyson, J. A., Gee, P., & dell'Antonio, I. 2008, ApJ, 673, 163, 0706.2351
- [139] Sheldon, E. S. et al. 2001, ApJ, 554, 881, arXiv:astro-ph/0103029
- [140] Simon, J. D., Bolatto, A. D., Leroy, A., Blitz, L., & Gates, E. L. 2005, ApJ, 621, 757, arXiv:astro-ph/0412035
- [141] Song, J. et al. 2012, ApJ, 761, 22, 1207.4369

- [142] Spergel, D. N., & Steinhardt, P. J. 2000, Physical Review Letters, 84, 3760, arXiv:astro-ph/9909386
- [143] Springel, V., & Farrar, G. R. 2007, MNRAS, 380, 911, arXiv:astro-ph/0703232
- [144] Steigman, G. 2008, JCAP, 10, 1, 0808.1122
- [145] The Dark Energy Survey Collaboration. 2005, ArXiv Astrophysics e-prints, arXiv:astro-ph/0510346
- [146] Tremaine, S., & Gunn, J. E. 1979, Physical Review Letters, 42, 407
- [147] Tulin, S., Yu, H.-B., & Zurek, K. M. 2012, JCAP, 5, 13, 1202.0283
- [148] ——. 2013, Physical Review Letters, 110, 111301, 1210.0900
- [149] Tyson, J. A. 2002, in Society of Photo-Optical Instrumentation Engineers (SPIE) Conference Series, Vol. 4836, Society of Photo-Optical Instrumentation Engineers (SPIE) Conference Series, ed. J. A. Tyson & S. Wolff, 10–20, arXiv:astro-ph/0302102
- [150] Tyson, J. A., Wenk, R. A., & Valdes, F. 1990, ApJ, 349, L1
- [151] van den Bergh, S. 1999, PASP, 111, 657, arXiv:astro-ph/9904251
- [152] van Weeren, R. J., Brüggen, M., Röttgering, H. J. A., & Hoeft, M. 2011, MNRAS, 418, 230, 1108.1398
- [153] van Weeren, R. J., Hoeft, M., Röttgering, H. J. A., Brüggen, M., Intema, H. T., & van Velzen, S. 2011, A&A, 528, A38, 1102.2235
- [154] van Weeren, R. J., Röttgering, H. J. A., Brüggen, M., & Hoeft, M. 2010, Science, 330, 347, 1010.4306
- [155] Vanderlinde, K. et al. 2010, ApJ, 722, 1180, 1003.0003
- [156] Vikhlinin, A. et al. 2009, ApJ, 692, 1033, 0805.2207
- [157] Vikhlinin, A., & Markevitch, M. 2003, in Astronomical Society of the Pacific Conference Series, Vol. 301, Matter and Energy in Clusters of Galaxies, ed. S. Bowyer & C.-Y. Hwang, 63
- [158] Villaescusa-Navarro, F., & Dalal, N. 2011, JCAP, 3, 24, 1010.3008
- [159] Vogelsberger, M., & Zavala, J. 2013, MNRAS, 430, 1722, 1211.1377
- [160] Vogelsberger, M., Zavala, J., & Loeb, A. 2012, MNRAS, 423, 3740, 1201.5892
- [161] von der Linden, A. et al. 2012, ArXiv e-prints, 1208.0597
- [162] Walker, M. 2013, Dark Matter in the Galactic Dwarf Spheroidal Satellites, ed. T. D. Oswalt & G. Gilmore, 1039

- [163] Walker, M. G., & Peñarrubia, J. 2011, ApJ, 742, 20, 1108.2404
- [164] Wechsler, R. H., Bullock, J. S., Primack, J. R., Kravtsov, A. V., & Dekel, A. 2002, ApJ, 568, 52, arXiv:astro-ph/0108151
- [165] Willman, B. 2010, Advances in Astronomy, 2010, 0907.4758
- [166] Wittman, D. M. et al. 2002, in Society of Photo-Optical Instrumentation Engineers (SPIE) Conference Series, Vol. 4836, Society of Photo-Optical Instrumentation Engineers (SPIE) Conference Series, ed. J. A. Tyson & S. Wolff, 73–82, arXiv:astro-ph/0210118
- [167] Yagi, M., Kashikawa, N., Sekiguchi, M., Doi, M., Yasuda, N., Shimasaku, K., & Okamura, S. 2002, AJ, 123, 66
- [168] Yang, X., Mo, H. J., van den Bosch, F. C., Zhang, Y., & Han, J. 2012, ApJ, 752, 41, 1110.1420
- [169] Yoshida, N., Springel, V., White, S. D. M., & Tormen, G. 2000, ApJ, 535, L103, arXiv:astro-ph/0002362
- [170] ——. 2000, ApJ, 544, L87, arXiv:astro-ph/0006134
- [171] Zavala, J., Vogelsberger, M., & Walker, M. G. 2013, MNRAS, 431, L20, 1211.6426
- [172] Zwicky, F. 1933, Helvetica Physica Acta, 6, 110
- [173] ——. 1937, ApJ, 86, 217